Title
Ionization injection plasma wakefield acceleration

Permalink
https://escholarship.org/uc/item/5gh0k91r

Author
Xi, Yunfeng

Publication Date
2016

Peer reviewed|Thesis/dissertation

Universidad of California

Los Angeles

Ionization injection plasma wakefield acceleration

A dissertation submitted in partial satisfaction
of the requirements for the degree
Doctor of Philosophy in Physics

by

Yunfeng Xi

2016

ABSTRACT OF THE DISSERTATION

Ionization injection plasma wakefield acceleration

by

Yunfeng Xi

Doctor of Philosophy in Physics

University of California, Los Angeles, 2016

Professor James Rosenzweig, Chair

Plasma-based acceleration, either driven by laser (LWFA) or driven by electron beam (PWFA) has the potential of accelerating electrons to GeV in a few centimeters. This allows construction of table-top accelerator which can be applied to build light source such as free electron laser (FEL) or high energy particle collider. The driver bunch loses energy to plasma when driving a wake. The following witness bunch injected at correct phase will be accelerated. Here we report a novel injection scheme, laser-ionization injection where the witness bunch is formed by laser-ionizing higher-threshold gas such as He. Simulation and numerical calculation is presented to evaluate the beam quality, the beam emittance is estimated to be 10^{-8} mrad. Experimental key issues such as timing synchronization of laser pulse and electron bunch and eliminate "dark current" are taken care of before the plasma acceleration experiment is carried out. Two beams are synchronized to 100-fs level via plasma radiation observation and Electro-Optic Sampling (EOS). "Dark current" is reduced to trivial level by tuning plasma density and driver bunch configuration. We observed 1 GeV gain of witness bunch with 5% energy spread.

The dissertation of Yunfeng Xi is approved.

Louis Bouchard

Warren Mori

Pietro Musumeci

James Rosenzweig, Committee Chair

University of California, Los Angeles

2016

To my parents . . .

who—among so many other things—

have been supporting me unconditionally.

Table of Contents

List of Figures

LIST OF TABLES

ACKNOWLEDGMENTS

Last six years in UCLA is the best in my life. I would like to acknowledge gratefully that my advisor James Rosenzweig who has supported me both academically and financially. Also, I thank my colleagues both in UCLA and in SLAC National Laboratory. Together, we spent so many sleepless nights in tunnel and main control room and drank countless cups of coffee. Now, it is time for me to turn a new page of my life. I am going to miss the beautiful UCLA campus. I am going to miss the beach and sunset of Los Angeles. "You can check-out any time you like, but you can never leave!"

2010–2012   M.S. (Physics), UCLA, Los Angeles, California.

2010–2012   Teaching Assistant, Department of Physics and Astronomy, UCLA, Los Angeles, California.

2012–2016   Facility User, SLAC National Accelerator Laboratory, Menlo Park, California.

2012–2016   Research Assistant, Particle Beam Physics Lab, UCLA, Los Angeles, California.

PUBLICATIONS

- Georg Wittig, Oliver S. Karger, Alexander Knetsch, Yunfeng Xi, Aihua Deng, James B. Rosenzweig, David L. Bruhwiler, Jonathan Smith, Zheng-Ming Sheng, Dino A. Jaroszynski, Grace G. Manahan and Bernhard Hidding, Nuclear Instruments and Methods in Physics Research Section A 829, 83-87 (2016)

- G. G. Manahan, A. Deng, O. Karger, Y. Xi, A. Knetsch, M. Litos, G. Wittig, T. Heinemann, J. Smith, Z. M. Sheng et al Phys. Rev. Accel. Beams 19, 011303 (2016)

- G. Wittig, O. Karger, A. Knetsch, Y. Xi, A. Deng, J. B. Rosenzweig, D. L. Bruhwiler, J. Smith, G. G. Manahan, Z.-M. Sheng, D. A. Jaroszynski, and B. Hidding, Phys. Rev. Accel. Beams 18, 081304 (2015)

- B. Hidding, G. G. Manahan, O. Karger, A. Knetsch, G. Wittig, D. A. Jaroszynski, Z.-M. Sheng, Y. Xi, A. Deng, J. B. Rosenzweig et al., J. Phys. B 47, 234010 (2014)

- Y. Xi, B. Hidding, D. Bruhwiler, G. Pretzler, and J. B. Rosenzweig, Phys. Rev. Accel. Beams 16, 031303 (2013)

- B. Hidding, J. B. Rosenzweig, Y. Xi, B. OShea, G. Andonian, D. Schiller, S. Barber, O. Williams, G. Pretzler, T. Knigstein et al., AIP Conf. Proc. 1507, 570 (2012)

CHAPTER 1

Introduction

We have made remarkable achievements in particle physics area thanks to accelerator technology development. Over the last decades, particle acceleration has been improved by many orders of magnitude. Figure 1.1 plotted the trend of energy of particle beam produced in laboratories. The plot, named "Livingston plot", was originally made by M. Stanley Livingston in 1954. Since then, the plot has been updated based on accelerator development. From the plot, the energy of accelerators has been growing exponentially in time. Starting from the 1930s, the energy has increased by a factor of 10 every 7 years. However, on each branch, the trend starts to bend and goes to a plateau eventually. This is because for each technology, there is a limit for particle acceleration. People have been developing new accelerator technologies to start new branches on the plot to boost up the accelerating energy exponentially instead of simply scaling up given machine linearly.

While already standing on the frontier of 10 TeV, we are still pushing the high energy boundary for two reasons: according to quantum mechanics, the higher energy the particle possesses, the shorter the associated wavelength, thus to investigate finer structure, we need to accelerate probe particle further. On the other hand, most of interesting particles nowadays do not exist in nature and live only in extremely short span during particle colliding process. Higher energy collision is required to create new heavier particles. Besides the colliders, accelerator also serves as beam source to generate radiation source such as Free-Electron Laser (FEL) [BPN84]. Linac Coherent Light Source (LCLS) at SLAC National Laboratory has been a huge success and has wide application in biology and chemistry imaging.

These motivations drive accelerator scientists to accelerate particles to higher and higher energy. Echoing the radio-frequency (RF) structure developed decades ago, people have to construct larger size accelerators. For example, the International Linear Collider
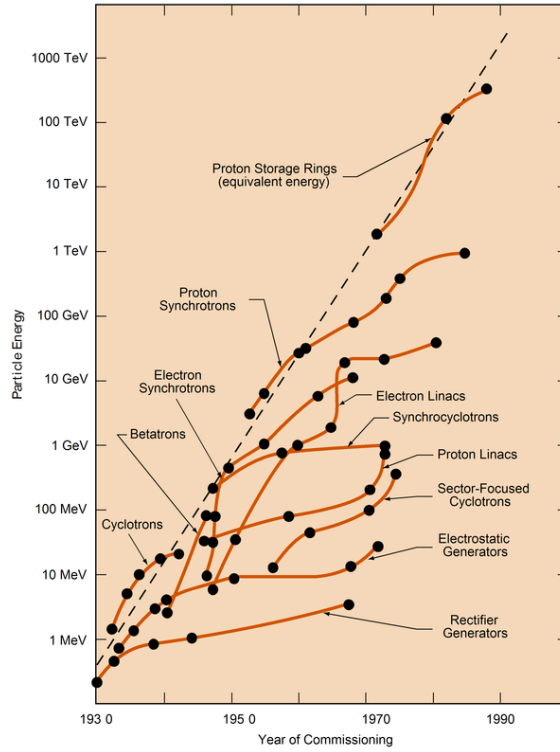
Figure 1.1: A Livingston plot showing accelerator energy versus time, updated to include machines that came on line during the 1980s. The filled circles indicate new or upgraded accelerators of each type.

(ILC) has been proposed as next generation linac. The design energy is 500 GeV initially and followed by a upgrade to 1 TeV later with the accelerator length of 30-50 km. The financial cost which is estimated as US$25 billion has been the major concern. The physical size and financial budget limits the construction of accelerator that delivers higher-energy particles.

To break the limit of financial cost and accelerator dimension, novel accelerator has to be invented to exceed the current 100 MV/m gradient based on RF. A new branch on "Livingston plot" has been established since 1970s known as wakefield accelerator. This type of accelerator usually involves two bunches: driver bunch and witness bunch. The driver bunch could be electron bunch. The energy of the driver bunch varies from 100 MeV to 10 GeV. It can also be a laser pulse with pulse duration of tens of femtoseconds, spot size of a few microns, normalized vector potential a_0 of 3 or 4. The driver beam travels through accelerating structure. Depending on whether the structure is gas or dielectric material, it is called plasma wakefield or dielectric wakefield respectively.

2

Because of boundary condition, driver bunch deposits energy into the structure in the form of wakefield and the following witness bunch absorbs energy from it. The gradient of wakefield accelerator is usually GeV/m or even 10s of GeV/m which is orders of magnitude higher than traditional RF-based accelerator.

In this dissertation, we focus on plasma wakefield with electron bunch as the driver and discuss the progress we have made both in simulation and experiment during last a few years. In Chapter 1, the concept of wakefield-based accelerator has been introduced with a brief review of accelerator history. In Chapter 2, theories and definitions will be discussed for describing and measuring the characteristics of beam as beam evolves in different situations. PIC simulation which is the most popular method in beam and particle fields will be mentioned at the end. In Chapter 3, we will list different schemes of plasma wakefield acceleration (PWFA) that have been proposed and tested so far. With all these ways paved, we will introduce our ionization injection scheme PWFA in Chapter 4. The emittance of the witness beam will be estimated. While in Chapter 5, we will report the experiment conducted in SLAC. A few experimental key steps such as timing and beam diagnostics will be pointed out and spent more attention.

CHAPTER 2

Beam dynamics

The goal of our experiment is to produce ultra-low emittance and high brightness electron beam from plasma wakefield acceleration. Therefore, it is necessary to explain the definition of emittance and brightness. In this chapter, we will introduce phase space representation of beam first and then derive motion equations of beam including effects of both external electromagnetic field and self-field. Following up that, we will introduce beam emittance and brightness. At the end, we introduce the most popular simulation scheme Particle-In-Cell (PIC) and discuss how equations of motion and Maxwell equations are discretized.

2.1 Phase space

In 3D world, each particle has its own position ($\vec{\mathbf{x}}$) and momentum ($\vec{\mathbf{p}}$) in three directions at each moment. $\vec{\mathbf{x}}$ and $\vec{\mathbf{p}}$ which have six degrees of freedom in total compose *phase space*. Consider N particles in an ensemble, the distribution of particles in phase space can be written as

$$F(\vec{\mathbf{x}}, \vec{\mathbf{p}}) = \sum_{i=1}^{N} \delta^3(\vec{\mathbf{x}} - \vec{\mathbf{x}}_i)\delta^3(\vec{\mathbf{p}} - \vec{\mathbf{p}}_i) \tag{2.1}$$

where delta function $\delta^3(\vec{\mathbf{x}} - \vec{\mathbf{x}}_i)\delta^3(\vec{\mathbf{p}} - \vec{\mathbf{p}}_i)$ denotes the position of momentum of ith particle in phase space. With the density function above, the total number of particles in integral form is

$$N = \int f(\vec{\mathbf{x}}, \vec{\mathbf{p}})d^3x d^3p \tag{2.2}$$

In a system where particle number is conservative, the continuity equation is

$$\frac{\partial F}{\partial t} + \nabla_{\vec{\mathbf{x}}} \cdot (\dot{\vec{\mathbf{x}}}F) + \nabla_{\vec{\mathbf{p}}} \cdot (\dot{\vec{\mathbf{p}}}F) = 0 \tag{2.3}$$

where $\nabla_{\vec{\mathbf{x}}}$ and $\nabla_{\vec{\mathbf{p}}}$ are divergence operator with respect to $\vec{\mathbf{x}}$ and $\vec{\mathbf{p}}$. If we insert Hamilton's equations $\frac{\partial H}{\partial p} = \frac{dx}{dt}$ and $\frac{\partial H}{\partial x} = -\frac{dp}{dt}$ into continuity equation and realize that $\mathbf{x}$ and $\mathbf{p}$ are independent variables, we obtain

$$\frac{\partial F}{\partial t} + \dot{\vec{\mathbf{x}}} \cdot \nabla_{\vec{\mathbf{x}}}F + \dot{\vec{\mathbf{p}}} \cdot \nabla_{\vec{\mathbf{p}}}F + (\dot{\vec{\mathbf{x}}} \cdot \nabla_{\vec{\mathbf{x}}} + \dot{\vec{\mathbf{p}}} \cdot \nabla_{\vec{\mathbf{p}}})F = 0 \tag{2.4}$$

$$\frac{\partial F}{\partial t} + \dot{\vec{\mathbf{x}}} \cdot \nabla_{\vec{\mathbf{x}}}F + \dot{\vec{\mathbf{p}}} \cdot \nabla_{\vec{\mathbf{p}}}F + \sum_{j=1}^{3} \left(\frac{\partial^2 H}{\partial x_j \partial p_j} - \frac{\partial^2 H}{\partial p_j \partial x_j} \right)F = 0 \tag{2.5}$$

$$\frac{dF}{dt} = \frac{\partial F}{\partial t} + \dot{\vec{\mathbf{x}}} \cdot \nabla_{\vec{\mathbf{x}}}F + \dot{\vec{\mathbf{p}}} \cdot \nabla_{\vec{\mathbf{p}}}F = 0 \tag{2.6}$$

Equation 2.6 is called *Klimontovich equation*[Nic83]. This equation describes a beam exactly. However, what we are interested in is the average properties of beam. Thus we define the ensemble average of $F(\mathbf{x}, \mathbf{p}, \text{t})$ as $f(\mathbf{x}, \mathbf{p}, \text{t})$ and the residual is defined as δF whose ensemble average $\langle \delta F \rangle$ is 0. Usually N is very large so that effects associated with δF such as short range collisions between beam particles can be neglected. Hence we obtain

$$\frac{\partial f}{\partial t} + \dot{\vec{\mathbf{x}}} \cdot \nabla_{\vec{\mathbf{x}}}f + \dot{\vec{\mathbf{p}}} \cdot \nabla_{\vec{\mathbf{p}}}f = 0 \tag{2.7}$$

which is called the *Vlasov equation*. It is often erroneously referred to *Liouville's theorem*. Though the finite volume in 6-dimensional phase space is independent of time, the surface corresponding to the volume may change, we will see an example in a moment. Also, the volume in a subspace of 6-dimensional phase space is not necessarily constant. In some cases when each subspace is independent of other degrees of freedom and can be decoupled from them, the subspace volumes can be constant.

One of the most common distributions is Gaussian distribution, the 2-dimensional form (x, p_x) can be written as

$$f_x(x, p_x) = \frac{1}{2\pi\sigma_x\sigma_{p_x}} exp(-\frac{x^2}{2\sigma_x^2}) exp(-\frac{p_x^2}{2\sigma_{p_x}^2}) \tag{2.8}$$

Note that here we assume the restoring force is linear with x and independent of p_x, thus x and p_x can be decoupled in the distribution above. σ_x is related to restoring force, while σ_{p_x} represents the average kinetic energy of ensemble which is also called temperature.
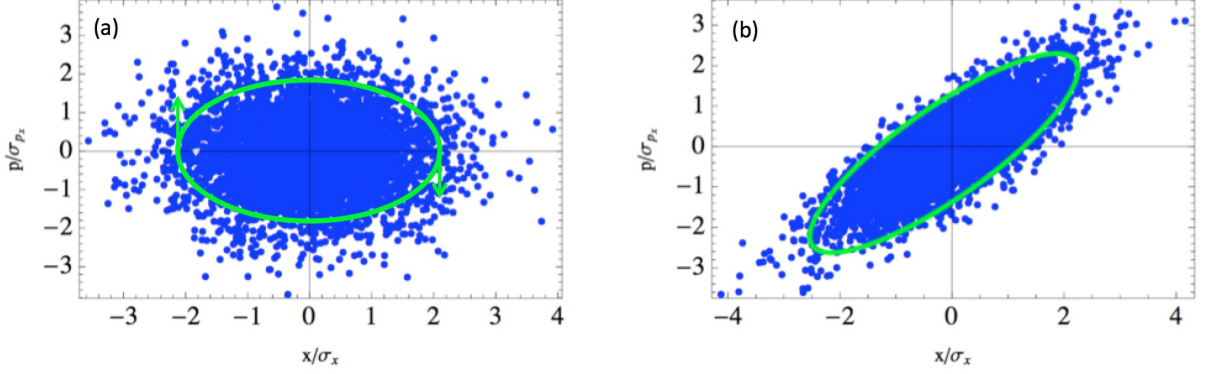
Figure 2.1: Plot (a) is bi-Gaussian distribution of (x, p_x) in phase space. Plot (b) is drifted bi-Gaussian distribution after restoring force is removed.

The bi-Gaussian distribution is shown in Figure 2.1 (a). As the beam oscillates, the elliptical profile rotates clockwise. After the restoring force is removed, p_x becomes constant while $x = x_0 + p_x t / m$. Now the elliptical profile is tilted and stretched which indicates there is correlation between x and p_x. *Liouville's theorem* tells us the areas of the two ellipses are the same. This property that the area of an ellipse in phase space that contains a given portion of the distribution remains constant if the restoring force is linear is very important in beam physics. The area of the ellipse is related to *emittance*, so equivalently, linear force does not change beam emittance. We will also prove this mathematically in next section. This is also an important characteristic of plasma wakefield since the transverse wakefield is almost linear which would not increase beam emittance. On the other hand, if the beam is not linear, the ellipse will be filamented. Though the curve encloses the same area as before, the quality of distribution is spoiled.

2.2 Beam emittance

The last section is discussed in Hamiltonian form using canonical momentum and coordinates. It is a rigorous analysis of classic motion of particles. However, in practice, we

are not interested in the complete description of beam development. Instead, we want to know transverse size and momentum spread as function of position along the accelerating structure, not time. For convenience of this analysis, people invented a new coordinate system which keeps track of position and momentum deviations from the design trajectory named *Curvilinear Coordinate System*. Here "design trajectory" means the perfect path of particle traveling through accelerator without any focusing or beam manipulating components. In beam physics, particles have much smaller transverse momentum than longitudinal momentum which means paraxial approximation is valid ($p_x, p_y \ll p_z \approx p$, $p^2 = p_x^2 + p_y^2 + p_z^2$). With this approximation, we can replace p_x with $x' \equiv dx/dz$, because

$$\frac{dx}{dz} = \frac{dx/dt}{dz/dt} = \frac{v_x}{v_z} \approx \frac{p_x}{p} \tag{2.9}$$

Now the phase space distribution $f_x(x, p_x)$ becomes $f_x(x, x')$. Note that we only discussed x, but same transformation can be applied to y direction by default.

Another issue is about the definition of beam spread. As you might have noticed in the bi-Gaussian distribution example above, the distribution has a theoretically infinite edge which makes it difficult to define the beam size. Conventionally, beam emittance ε_x is defined as the area of ellipse that contains 95% of particle as the green ellipsis shown in Figure 2.1. 95% is somewhat arbitrary. One could equally use 90%.

Another method to characterize beam spread is using root-mean-square (RMS) derived from second moment of distributions. This method was introduced by Lapostolle and Sacherer [Lap71, Sac71]. They proposed the concept of *equivalent beams*. It states it states that if the current (a measure of the space-charge force) and kinetic energy of two distributions are the same, and the second moments of the distributions are the same, then they will remain the same when subjected to the same external forces.

The second moments of distribution $f_x(x, x')$ are listed below:

$$\begin{aligned}
\langle x^2 \rangle &= \iint x^2 f_x(x, x') dx dx' \\
\langle x'^2 \rangle &= \iint x'^2 f_x(x, x') dx dx' \\
\langle xx' \rangle &= \iint xx' f_x(x, x') dx dx'
\end{aligned} \tag{2.10}$$

$\sqrt{\langle x^2 \rangle}$ is defined as spatial RMS σ_x. Similarly, $\sigma_{x'} \equiv \sqrt{\langle x'^2 \rangle}$ and $\sigma_{xx'} \equiv \langle xx' \rangle$. The RMS emittance is defined analytically in terms of the second moments as

$$\varepsilon_x \equiv \sqrt{\langle x^2 \rangle \langle x'^2 \rangle - \langle xx' \rangle^2} \tag{2.11}$$

Emittance is a quantitative measure of the beam quality. It represents the effective trace space area of the beam. As the beam gains energy along propagation, x' decreases due to the factor of γ on denominator. As a result, the RMS emittance will decreases while transverse remains the same. It is called *adiabatic damping.* To address this, we define *normalized emittance* as

$$\varepsilon_{x,n} = \beta\gamma\varepsilon_x \tag{2.12}$$

where $\beta = v/c$, $\gamma = 1/(1 - \beta^2)^{1/2}$ is Lorentz factor, m is electron rest mass and c is the speed of light.

Figure 2.2 shows the relation between area of RMS ellipse and RMS emittance in trace space and geometric meaning of σ_x and $\sigma_{x'}$. This ellipse can also be expressed as *RMS ellipse equation*

$$\sigma_{x'}^2 x^2 - 2\sigma_{xx'}xx' + \sigma_x^2 x'^2 = \varepsilon_x^2 \tag{2.13}$$

or

$$\hat{\gamma}x^2 + 2\hat{\alpha}xx' + \hat{\beta}x'^2 = \varepsilon_x^2 \tag{2.14}$$

where $\hat{\alpha} = -xx'$, $\hat{\beta} = x^2$, $\hat{\gamma} = \frac{1+\hat{\alpha}^2}{\hat{\beta}}$ are Courant-Snyder parameters.

2.3   Beam envelope equation

There is a formalism developed called *envelope equation* to allow us to perform a more general analysis of behavior of beam slices. It can include linear effect such as space charge effect, external focusing and accelerating forces and emittance in a straightforward way.
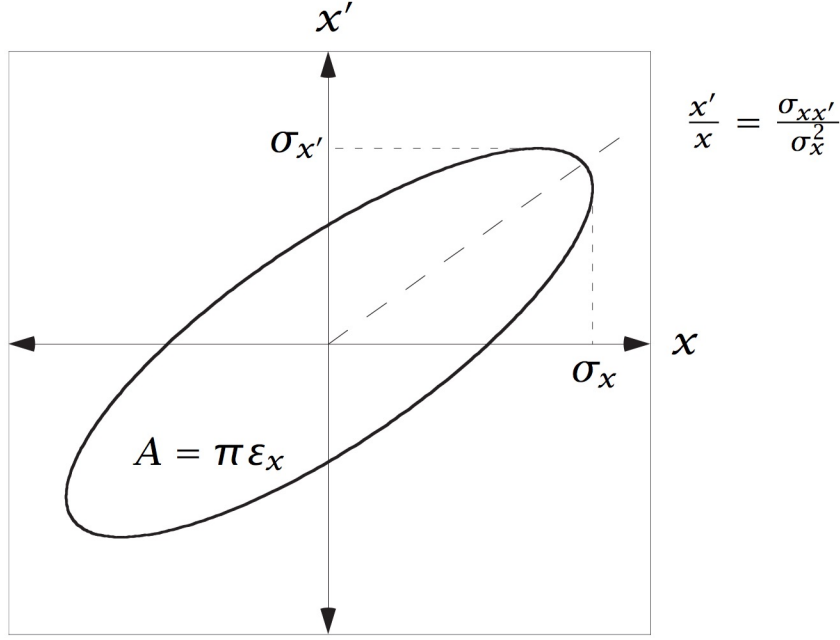
Figure 2.2: Properties of beam RMS ellipse

As a starting point, we derive the envelope equation in general. The differentiate of beam RMS size can be written as

$$\sigma'_x = \frac{d}{dz}(\sqrt{\langle x^2 \rangle}) = \frac{\langle xx' \rangle}{\sigma_x} \tag{2.15}$$

$$\sigma''_x = \frac{1}{\sigma_x^2}[\sigma_x \frac{d\langle xx' \rangle}{dz} - \frac{\langle xx' \rangle^2}{\sigma_x}] \tag{2.16}$$

In equation above, $d\langle xx' \rangle/dz$ can be written as $\langle x'^2 \rangle + \langle xx'' \rangle - \frac{\gamma'}{\gamma}\langle xx' \rangle$. Thus

$$\sigma''_x = \frac{1}{\sigma_x^2}[\sigma_x(\langle x'^2 \rangle + \langle xx'' \rangle - \frac{\gamma'}{\gamma}\langle xx' \rangle) - \frac{\langle xx' \rangle^2}{\sigma_x}] \tag{2.17}$$

$$\sigma''_x + \frac{\gamma'}{\gamma}\sigma'_x = \frac{\varepsilon_x^2}{\sigma_x^3} + \frac{\langle xx'' \rangle}{\sigma_x} \tag{2.18}$$

Note that Equation 2.17 is derived based on the assumption that $(\beta\gamma)' \approx \gamma'$. Also, ε_x is geometric emmitance. The $\langle xx'' \rangle$ on RHS of Equation is the force term which includes all of transverse force effects as mentioned above: space charge, linear focusing force etc.

If the force is linear external focusing force, it can be written as $x'' = -\kappa_\beta^2(z)x$. For example, in quadrupole focusing case, $\kappa_\beta^2 = eB'/p$, so the force term for quadrupole focusing is

$$\frac{\langle xx'' \rangle}{\sigma_x} = -\frac{\kappa_\beta^2 \langle x^2 \rangle}{\sigma_x} = -\kappa_\beta^2 \sigma_x \tag{2.19}$$

It is more natural to write the equation in cylindrical coordinates if the beam profile and external force have axial symmetry. Now x in equations above is replaced by r. The definition of radial emittance as $\varepsilon_r^2 = \langle r^2 \rangle \langle r'^2 \rangle - \langle rr' \rangle^2$ where $r' = p_r/p$.

For example, the focusing force in RF accelerating structures is axisymmetric. The average form is

$$\langle F_r \rangle = -\frac{\eta}{8} \frac{(eE_0)^2}{\gamma mc^2} r \tag{2.20}$$

where E_0 is the peak accelerating field and η is a factor related to spatial harmonics of the RF fields. We know with paraxial approximation $p_z \ll p_r$

$$\frac{dp_r}{dt} = \frac{d(\gamma mv_r)}{dt} = \gamma m \frac{d^2 r}{dt^2} = \gamma m v_z^2 \frac{d^2 r}{dz^2} \approx \gamma m \beta^2 c^2 \gamma'' \tag{2.21}$$

After we substitute Equation into Equation , we obtain

$$r'' = -\frac{\eta}{8} \left(\frac{eE_0}{\gamma mc^2} \right)^2 r = -\frac{\eta}{8} \left(\frac{\gamma'}{\gamma} \right)^2 r \tag{2.22}$$

where $\gamma'' = eE_0/mc^2$ is named normalized energy gain. Therefore,

$$\frac{\langle rr'' \rangle}{\sigma_r} = -\frac{\eta}{8} \left(\frac{\gamma'}{\gamma} \right)^2 \sigma_r \tag{2.23}$$

Finally the radial envelope equation including focusing and acceleration terms can be written as

$$\sigma_r'' + \frac{\gamma'}{\gamma} \sigma_r' + \frac{\eta}{8} \left(\frac{\gamma'}{\gamma} \right)^2 \sigma_r = \frac{\varepsilon_r^2}{\sigma_r^3} + \frac{\langle rr'' \rangle_{sc}}{\sigma_r} \tag{2.24}$$

In this envelope equation, the second and third term on LHS are accelerating term and focusing term respectively while on RHS, the first term is due to emittance and the subscript "sc" in second term represents "space charge".

2.4 Beam brightness

Beam brightness was first defined by von Borries and Rhushka in 1939 [BR39] as $B = I/(A\Omega)$ where I is beam current, A is beam transverse area and Ω is the divergence of the beam. Since then, it has become a useful figure of merit to evaluate beam quality because it summarizes many properties of an electron beam. There are different definitions of beam brightness in accelerator and beam physics. For example, the 5D brightness is defined as Equation 2.25. This is the relativistic analog of the microscope brightness.

$$B_{5D} = \frac{2I}{\varepsilon_{nx}\varepsilon_{ny}} \sim \frac{2I}{(\beta\gamma)^2 \varepsilon_x \varepsilon_y} \tag{2.25}$$

where ε_x and ε_y are emittance in x and y direction respectively and subscript "n" denotes "normalized". Another definition is 6D brightness which is the true figure of merit, but it is hard to measure in practice.

$$B_{6D} = \frac{N}{\varepsilon_{nx}\varepsilon_{ny}\sigma_z\sigma_\gamma} \tag{2.26}$$

where σ_z is the RMS bunch length and σ_γ is the RMS energy spread. This brightness converses when the forces are linear.
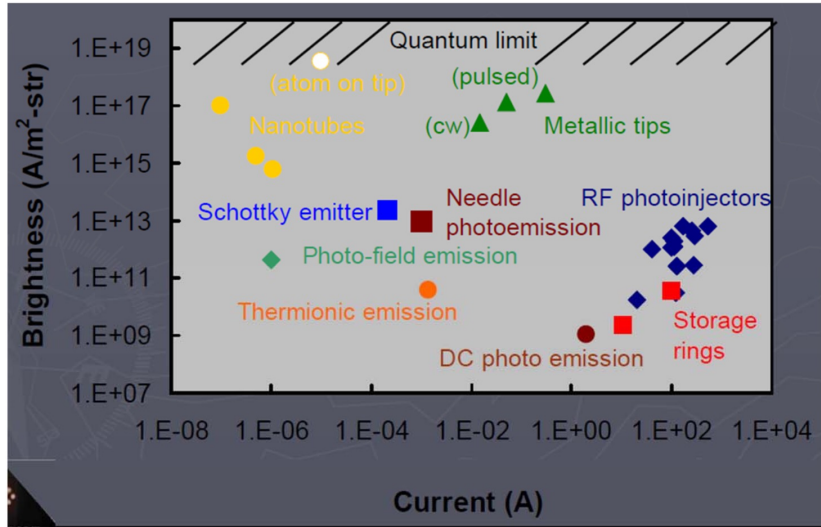
Figure 2.3: Distribution of various electron sources in brightness and current

Figure 2.3 from C. Brau shows brightness and current of different electron sources which spans many orders of magnitude. The RF photoinjectors of our interest are located

around $10 - 100A$ and $10^{11} - 10^{13} A/m^2$ region.

An interesting side note is that there is quantum limit for beam brightness for the reason that Pauli exclusion principle and Heisenberg uncertainty principle. According to [M.B.Callaham,IEEEJ.quantumelectronics,24:1958,1988], the quantum limit for the maximum beam brightness is

$$B_{quantum} = \frac{2e}{h^3}(m_0 c)^3 = \frac{2e}{(\lambda_c)^3} \tag{2.27}$$

where h is Planck constant and λ_c is de Broglie wavelength. The order of magnitude of $B_{quantum}$ is $10^{25} A/m^2$. In reality, the state-of-the-art electron sources is only $10^{-4} B_{quantum}$ or less which is not even close to this limit.

2.5 Motion of Charged Particles in Fields

The interaction of particles and fields is complicated because fields affect particles' motion and particles' collective behavior updates fields distribution in return. For simplicity, we start with single particle motion and limit the discussion to the external field. Even so, calculating the motion of a charged particle can be quite hard.

$$\frac{d\boldsymbol{p}}{dt} = \frac{d(\gamma m \boldsymbol{v})}{dt} = q(\boldsymbol{E} + \boldsymbol{v} \times \boldsymbol{B}) \tag{2.28}$$

$$\frac{dE}{dt} = \frac{d(\gamma m c^2)}{dt} = \boldsymbol{v} \cdot \boldsymbol{F} \tag{2.29}$$

where m and q are particle's mass and charge. Here the "particle" is electron. $\boldsymbol{v}$ is the velocity of particle. $\boldsymbol{E}$ and $\boldsymbol{B}$ are external electric and magnetic fields. γ is Lorentz factor. $\boldsymbol{F}$ is external force due to fields. The physical interpretation of Equation and Equation are rate of change of momentum and energy respectively.

A simple case is constant $\boldsymbol{B}$ and $\boldsymbol{E} = 0$. We suppose the initial velocity of a particle is $\boldsymbol{v} = (0, 0, v_0)$ and $\boldsymbol{B} = (0, B_0, 0)$. From Equation , we immediately know there is not energy gain for particle and it will stay in circular motion in xz-plane. The force on particle $\boldsymbol{F}$ is

$$F_x = \gamma m \frac{dv_x}{dt} = \frac{ev_z B_0}{c} \tag{2.30}$$

$$F_y = 0 \tag{2.31}$$

$$F_z = \gamma m \frac{dv_z}{dt} = \frac{ev_x B_0}{c} \tag{2.32}$$

Taking the time derivative of equations above and substitute Equations 2.30 into RHS of new derivative equations, we obtain

$$\frac{d^2 v_x}{dt^2} = -(\frac{eB_0}{\gamma mc})^2 v_x \tag{2.33}$$

$$\frac{d^2 v_z}{dt^2} = -(\frac{eB_0}{\gamma mc})^2 v_z \tag{2.34}$$

The solution of this type of second-order derivative equation has sinusoidal form. With the initial conditions we assumed, the solution of particle's position is

$$x(t) = -\frac{v_0}{\Omega_0} cos(\Omega_0 t) + \frac{v_0}{\Omega_0} \tag{2.35}$$

$$z(t) = \frac{v_0}{\Omega_0} sin(\Omega_0 t) \tag{2.36}$$

where $\Omega_0 \equiv \frac{eB_0}{\gamma mc}$ is defined as *cyclotron frequency*.

To solve more general particle motion problem, let us review the example above in curvilinear coordinate system that we introduced in early section. We choose the direction of motion of particle to be the s direction. y direction is perpendicular to motion plane. In new coordinate system, the infinitesimal step ds_i can be written as

$$d\boldsymbol{r} = ds_x \hat{x} + ds_y \hat{y} + ds_\theta \hat{s} \tag{2.37}$$

$$= dx\hat{x} + dy\hat{y} + (x + R)d\theta\hat{s}$$

$$= dx\hat{x} + dy\hat{y} + (1 + \frac{x}{R})ds\hat{s}$$

where $R = v_0/\Omega_0$ is radius of curvature. As time evolves the accelerator coordinate system will rotate as $ds/dt = v_0$. The time derivative of unit vectors are

13

$$\dot{\hat{s}} = \frac{d\hat{s}}{dt} = \frac{d\hat{s}}{d\theta}\frac{d\theta}{dt} = -\hat{x}(\frac{d}{dt}\frac{s}{R}) = -\frac{v_0\hat{x}}{R} \tag{2.38}$$

$$\dot{\hat{x}} = \frac{v_0\hat{s}}{R} \tag{2.39}$$

The position of one particular particle can be expressed as the difference between its absolute position $\boldsymbol{r}$ and reference frame $\boldsymbol{r_0}$. With two equations above, we can now derive the beam frame velocity

$$
\begin{aligned}
\dot{\boldsymbol{r}} &= \dot{\boldsymbol{r}}_0 + \dot{x}\hat{x} + x\dot{\hat{x}} + \dot{y}\hat{y} + y\dot{\hat{y}} + \dot{z}\hat{s} + z\dot{\hat{s}} \\
&= \dot{\boldsymbol{r}}_0 + \dot{x}\hat{x} + x\frac{v_0}{R}\hat{s} + \dot{y}\hat{y} + \dot{z}\hat{s} - z\frac{v_0}{R}\hat{x} \\
&= (\dot{x} - z\frac{v_0}{R})\hat{x} + \dot{y}\hat{y} + (1 + \frac{x}{R} + \frac{\dot{z}}{v_0})v_0\hat{s}
\end{aligned}
\tag{2.40}
$$

The chain rule can be applied to derive the relation between time derivative and position derivative. Note the distinction between $\dot{()}$ and $()'$.

$$\dot{x} = \frac{dx}{dt} = \frac{dx}{ds}\frac{ds}{dt} = v_0 x' \tag{2.41}$$

The last step of Equation 2.40 can be rewritten as

$$\dot{r} = (x' - \frac{z}{R})v_0\hat{x} + y'v_0\hat{y} + (1 + \frac{x}{R} + z')v_0\hat{s} \tag{2.42}$$

If we take the time derivative of velocity equation, we can get acceleration equations as follows:

$$
\begin{aligned}
\frac{\dot{v}_x}{v_0^2} &= x'' - \frac{2z'}{R} - z(\frac{1}{R})' - \frac{x}{R^2} - \frac{1}{R} \\
\frac{\dot{v}_y}{v_0^2} &= y'' \\
\frac{\dot{v}_z}{v_0^2} &= z'' - \frac{2x'}{R} - x(\frac{1}{R})' - \frac{z}{R^2}
\end{aligned}
\tag{2.43}
$$

We rewrite Equation 2.5 in three components:

$$\dot{v}_x = \frac{q}{\gamma mc}(v_y B_z - v_z B_y)$$

$$\dot{v}_y = \frac{q}{\gamma mc}(v_x B_z - v_z B_x) \tag{2.44}$$

$$\dot{v}_z = \frac{q}{\gamma mc}(v_x B_y - v_y B_x)$$

After we insert Equation 2.43 into Equation 2.44, acceleration equation can be written after arrangements as follows

$$x'' - \frac{2z'}{R} - z(\frac{1}{R})' - \frac{x}{R^2} - \frac{1}{R} = \frac{q}{\gamma mcv_0}(y'B_z - (1 + \frac{x}{R} + z')B_y)$$

$$y'' = -\frac{q}{\gamma mcv_0}((x' - \frac{z}{R})B_z - (1 + \frac{x}{R} + z')B_x) \tag{2.45}$$

$$z'' + \frac{2x'}{R} + x(\frac{1}{R})' - \frac{z}{R^2} = \frac{q}{\gamma mcv_0}((x' - \frac{z}{R})B_y - y'B_x)$$

The equations above describe particle's motion completely. However, they are not practically useful when magnetic field is not uniform. Approximation should be made to simplify these equations. Details of γ and $\boldsymbol{B}$ expansion are neglected here. After we drop nonlinear terms, we obtain the linear equations of motion as follow

$$x'' + (\frac{1}{R(s)^2} + K_n(s))x = 0 \tag{2.46}$$

$$y'' - K_n(s)y = 0 \tag{2.47}$$

where R(s) is dipole bending radius with dependence on s and $K_n = \frac{q}{p}\frac{dB_y}{dx}$ is quadrupole focusing strength. These equations are known as *Mathieu-Hill equation.* To write these two equations in the same form, we also define $K_x(s) \equiv 1/R(s)^2 + K_n(s)$ and $K_y(s) \equiv -K_n(s)$. The general form of equation tells us particle motion around the reference trajectory is caused by dipole bending and quadrupole focusing. Their strength varies with s in general. If $K_n(s)$ and $R(s)$ are constant or vary very slowly over s, the transverse motion can be regarded as "quasi-harmonic oscillation". To simplify the discussion further, we select a small piece of accelerator where $K(s)$ can be approximated as constant. We know that equation $u'' + Ku = 0$ with initial conditions: $u(0) = u_0$ and $u'(0) = u_0$ has solution like Equation 2.48

15

$$u(s) = \begin{cases} u_0 cos(\sqrt{K}s) + u_0'\frac{1}{\sqrt{K}}sin(\sqrt{K}s), K > 0 \\ u_0 cosh(\sqrt{|K|}s) + u_0'\frac{1}{\sqrt{|K|}}sinh(\sqrt{|K|}s), K < 0 \end{cases} \tag{2.48}$$

The solution above can also be written in matrix transformation from vector $(u_0, u_0')^T$ to $(u, u')^T$.

$$\begin{pmatrix} u \\ u' \end{pmatrix} = \begin{pmatrix} C(s) & S(s) \\ C'(s) & S'(s) \end{pmatrix} \begin{pmatrix} u_0 \\ u_0' \end{pmatrix} \tag{2.49}$$

where

$$C(s) = \begin{cases} cos(\sqrt{K}s), K > 0 \\ cosh(\sqrt{|K|}s), K < 0 \end{cases} \tag{2.50}$$

$$S(s) = \begin{cases} sin(\sqrt{K}s), K > 0 \\ sinh(\sqrt{|K|}s), K < 0 \end{cases} \tag{2.51}$$

C'(s) and S'(s) are their derivatives respectively.

In a drift space, the momentum of particle is constant. We take the limit of $K \rightarrow 0$ and assume the drifting distance is l, then the transform matrix becomes

$$M_{drift} = \begin{pmatrix} 1 & l \\ 0 & 1 \end{pmatrix} \tag{2.52}$$

Another case is transporting through a quadrupole without bending which indicates $\lim_{R\rightarrow\infty}(K_n + \frac{1}{R^2}) = K_n$. Therefore, the focusing and defocusing matrix are

$$M_{QF} = \begin{pmatrix} cos(\sqrt{K_n}l) & \frac{1}{\sqrt{K_n}}sin(\sqrt{K_n}l) \\ -\sqrt{K_n}sin(\sqrt{K_n}l) & cos(\sqrt{K_n}l) \end{pmatrix} \tag{2.53}$$

$$M_{QD} = \begin{pmatrix} cosh(\sqrt{|K_n|}l) & \frac{1}{\sqrt{|K_n|}}sinh(\sqrt{|K_n|}l) \\ \sqrt{|K_n|}sinh(\sqrt{|K_n|}l) & cosh(\sqrt{|K_n|}l) \end{pmatrix} \tag{2.54}$$

2.6   Particle-In-Cell simulation

In last sections, we have solved the motion equations for scenario where single particle moves in simple electric and/or magnetic fields. However, this is often not the case in real research. There are millions of particles in the system. And the fields are usually not uniformly distributed. Besides, there are interactions between particles in one cluster which increases the computing complexity to $O(N^2)$. It takes a huge amount of computing efforts, most of time it is impossible, to find the exact solution to each particle trajectory. On the other hand, people have little interest in one particular particle's position and momentum information. Instead, they would like to study collective behavior and dynamics of particles which leads to the possibility of reducing the computing complexity significantly with appropriate approximation treatment.

Particle-in-cell (PIC) is one of the most powerful methods to simulate particles dynamics. The history of PIC can date back to late 1905s when Buneman [Bun59] and Dawson [Daw62] published particle trajectory calculations. Note that in these papers, the basic physics models were based on the assumption that space charge was neglected. Charged particle trajectories were computed in specified fields in unbounded systems. In spite of that, these works laid the foundation of plasma physics computation. After that, the computational community realized particle-particle method was hard to scale up as the number of particle N and devised particle-mesh methods that the space (only 1D in early time) is discretized as a mesh and Poisson Equation is solved numerically on the mesh. At that time, this method was referred to as could-in-cell or particle-in-cell depending on weighting schemes. Though it was 1D simulation, it included space charge effect and achieved great success in solving plasma problems. The PIC scheme was realized in code and published by Birdsall and Langdon [BL85] and Hockney and Eastwood [HE81]. A lot of PIC theories were established in their works and have been adopted till now such as finite time, space discretization and electromagnetic schemes for propagating waves. Nowadays, PIC scheme has been implemented in both commercial software like Vorpal vended by Tech-X and open-source tool such as OSIRIS developed by Mori's group in UCLA and WARP by Lawrence Berkeley National Laboratory (LBNL).

In this framework, individual particles are traced in continuous phase space while

moments of particle distribution are computed on mesh grids. It can represent general distribution functions in phase space statistically. The equations that governs motion of particles and interaction between particles and electromagnetic fields usually retains the full nonlinear effects. Space charge and other collective effects can be included, thus the self-consistency of coupling of charged particles and fields is preserved. As shown in Figure 2.4, particles are defined in continuum space in both position and momentum (or velocity). fields $\boldsymbol{E}$ and $\boldsymbol{B}$ are defined on grids in space. Time, representing the evolution of motion of particles, is also treated as discrete quantity. Particles and fields information is updated per time step Δt initialized with initial conditions. Particles' position and momentum are advanced with current fields distribution in terms of motion equations. Then the boundary conditions are applied to determine wether particles should be absorbed or emitted. After that, with new particle distribution $(\boldsymbol{x}, \boldsymbol{p})$, we can obtain new source terms $(\rho, \boldsymbol{J})$. Then by solving Maxwell equations, we advance fields $\boldsymbol{E}$ and $\boldsymbol{B}$. This is one flow cycle of PIC scheme.
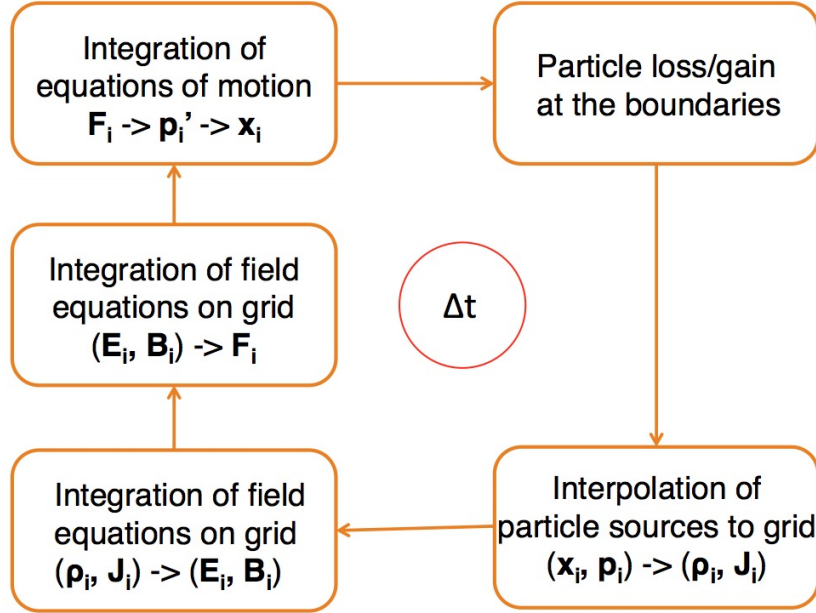
Figure 2.4: Schematic plot of working iteration of PIC scheme.

We already know the Newton-Lorentz equations of motion Equation 2.5 and $d\boldsymbol{x}/dt = \boldsymbol{v}$. In PIC scheme, it is discretized using the second order accurate center difference scheme, also known as the "leapfrog" scheme.

$$\frac{\boldsymbol{u}^{t+\Delta t/2} - \boldsymbol{u}^{t-\Delta t/2}}{\Delta t} = \frac{q}{m}(\boldsymbol{E}^t + \frac{\boldsymbol{u}^{t+\Delta t/2} + \boldsymbol{u}^{t-\Delta t/2}}{2\gamma^t} \times \boldsymbol{B}^t) \quad (2.55)$$

$$\frac{\boldsymbol{x}^{t+\Delta t} - \boldsymbol{x}^t}{\Delta t} = \frac{\boldsymbol{u}^{t+\Delta t/2}}{\gamma^{t+\Delta t/2}} \quad (2.56)$$

where $\boldsymbol{u} = \gamma \boldsymbol{v}$ and $\gamma^t = (\gamma^{t-\Delta t/2} + \gamma^{t+\Delta t/2})/2$. To write the equations above into a more explicit format, one common option is to use Boris pusher [Bor70].

$$\boldsymbol{u}^- = \boldsymbol{u}^{t-\Delta t/2} + \frac{q\Delta t \boldsymbol{E}^t}{2m} \quad (2.57)$$

$$\boldsymbol{u}' = \boldsymbol{u}^- + \boldsymbol{u}^- \times \boldsymbol{t}^t \quad (2.58)$$

$$\boldsymbol{u}^+ = \boldsymbol{u}^- + \boldsymbol{u}' \times \frac{2\boldsymbol{t}^t}{1 + \boldsymbol{t}^t \cdot \boldsymbol{t}^t} \quad (2.59)$$

$$\boldsymbol{u}^{t+\Delta t/2} = \boldsymbol{u}^+ + \frac{q\Delta t \boldsymbol{E}^t}{2m} \quad (2.60)$$

where $\boldsymbol{t}^t$ is defined as $\hat{B}tan(\frac{q\Delta t}{2m\gamma^t}B^t)$.

Boris pusher has excellent long term accuracy. The reason is that it conserves phase space volume. Since theory of relativity can be applied in any frame of reference, people have been thinking simulating plasma physics problem in the frame which minimizes the range of space and time scales [Vay07, MFL10]. However, because the equations are all discretized as discussed above, they may not preserve some fundamental properties and cause finite grid instability and numerical Cherenkov instability. The numerical noise could result in unpredictable errors in simulation. In 2007, Jean-Luc Vay proposed a novel Boris pusher to address this issue [Vay08].

For the field solver, it basically means solve finite-difference time-domain (FDTD) discretization on a Yee mesh 2.5. The electric field components form the edges of the cube and they are at integral multiples of the timestep, and the magnetic field components form the normals to the faces of the cube and they are at $t = (n + 1/2)\Delta t$, where n is an integer. The initial conditions must satisfy $\nabla \cdot \boldsymbol{B} = 0$ and $\nabla \cdot \boldsymbol{D} = \rho$ and then the electric and magnetic fields are advanced in time using finite-differenced forms of Faraday's law and Ampere's law.
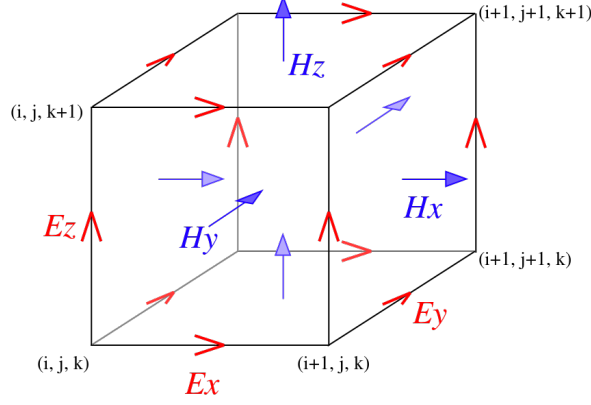
Figure 2.5: A Cartesian Yee cube used for FDTD to show how electric and magnetic field vector components are distributed.

$$\frac{\partial \boldsymbol{D}}{\partial t} = \nabla \times \boldsymbol{H} - \boldsymbol{J} \tag{2.61}$$

$$\frac{\partial \boldsymbol{B}}{\partial t} = -\nabla \times \boldsymbol{E} \tag{2.62}$$

The original Ampere' law and Faraday's law can be written in finite difference form as following:

$$\delta_t D_i = \delta_j H_k - \delta_k H_j \tag{2.63}$$

$$\delta_t B_i = -\delta_j E_k + \delta_k E_j \tag{2.64}$$

where i, j and k denote the indices of an orthogonal right-handed set of coordinates and δ_t denotes the finite-difference operator with respect to the variable t. The explicit format are written in Equations 2.66. As mentioned on Yee cube above, D, E and J are defined at the midpoint of the segments connecting mesh nodes, while B and H are defined on a mesh displaced by one half cell in each dimension.

$$\frac{D_i^t - D_i^{t-\Delta t}}{\Delta t} = \frac{H_{k,x_j+\Delta x_j/2}^{t-\Delta t/2} - H_{k,x_j-\Delta x_j/2}^{t-\Delta t/2}}{\Delta x_j} - \frac{H_{j,x_k+\Delta x_k/2}^{t-\Delta t/2} - H_{j,x_k-\Delta x_k/2}^{t-\Delta t/2}}{\Delta x_k} - J_i^{t-\Delta t/2} \tag{2.65}$$

$$\frac{B_i^{t+\Delta t/2} - B_i^{t-\Delta t/2}}{\Delta t} = -\frac{E_{k,x_j+\Delta x_j/2}^t - E_{k,x_j-\Delta x_j/2}^t}{\Delta x_j} + \frac{E_{j,x_k+\Delta x_k/2}^t - E_{j,x_k-\Delta x_k/2}^t}{\Delta x_k} \tag{2.66}$$

Although PIC has excellent performance and dominates in plasma simulation community, it is worth to point out that there are a few limitations in PIC scheme. A major one is that the particle per cell count rates follow Poisson statistics. For N_e particles per cell, the relative fluctuations are $1/\sqrt{N_e}$. If N_e is limited by computing power, large fluctuations can result in particle-wave collisions. Also, the dispersive relation can change artificially. Since this is beyond the topics we cover, we will skip the detail.

CHAPTER 3

Plasma-based wakefield acceleration overview

We start this section with introducing plasma wakefield acceleration (PWFA) along with its sister scheme laser wakefield acceleration (LWFA). Basic theories and simulations are presented. Especially, we demonstrate the derivation of the important theorem, *Panofsky-Wenzel theorem* which draws connection between transverse wakefield and longitudinal wakefield. Next, we overview the history of wakefield simulations and experiments briefly. In the last section, we discuss the current injection schemes that have been proposed and tested.

3.1   Plasma/laser wakefield acceleration

The basic concepts of plasma acceleration was originally conceived by Toshiki Tajima and John M. Dawson of UCLA in 1979 [TD79]. Initially plasma is prepared in equilibrium. If a strong electric or electromagnetic field is applied into plasma. As shown in Figure 3.1, the plasma electrons will be repelled away from center while background ions will be stationary in the time scale of excitation consider the huge mass difference (at least a factor of 1836). The temporary separation of electrons and ions creates a charge imbalance in the perturbed region. The plasma electrons experience strong attractive force back to center of the wake by positive plasma ion columns. This forms extremely high longitudinal (accelerating) and transverse (focusing) electric field. The accelerating gradient in the region between tail and middle of plasma column can be potentially used for electron acceleration. Note that originally laser pulse was suggested in Tajima and Dawson's paper. But the idea of using electron bunch as driver was proposed shortly after that [CDH85]. Beam-driven plasma wakefield acceleration is called PWFA while laser-driven scheme is called LWFA. In next discussions, beam-driven and laser-driven scheme will be mentioned both from time to time since they share a lot of commons though this

dissertation is dedicated to the work on beam-driven scenario.
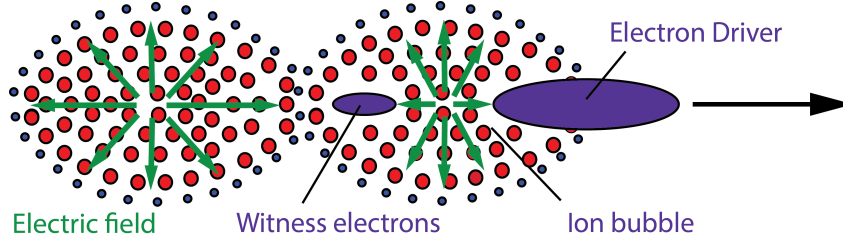
Figure 3.1: A schematic plot of plasma wakefield acceleration with driver bunch leading in front (right) and witness bunch following behind in the bubble. Both longitudinal and transversal wakefields are drawn in green. The figure source is here.

To compare the advantage of plasma acceleration to RF acceleration, we estimate accelerating gradient of plasma wakefield by calculating the cold nonrelativistic plasma wave breaking field $E_0 = cm_e\omega_p/e$ where $\omega_p = (4\pi n_0 e^2/m_e)^{1/2}$ is plasma frequency and n_0 is the ambient electron number density [Daw59]. c, m_e and e are speed of light in vacuum, electron's rest mass and charge respectively. More practically, the expression of E_0 is written as $E_0(V/m) \approx 96\sqrt{n_0(cm^{-3})}$. As we will discuss later, the plasma density of our interest is $n_0 = 10^{17} cm^{-3}$. In this case, wave-breaking field is estimated as 30 GV/m which is about two orders of magnitude higher than the state-of-the-art RF gun. Another advantage of plasma acceleration is that the plasma column length is approximately same as plasma wavelength which can be evaluated as $\lambda_p = 2\pi c/\omega_p = 2\pi/k_p$ and practically $\lambda_p(\mu m) \approx 3.3 \times 10^{10}/\sqrt{n_0(cm^{-3})}$, thus we can tune the length by changing plasma density.

Plasma-based acceleration was discussed mostly in linear regime in early days. In linear regime, both electrons and positrons can be accelerated in same structure as long as they are injected into correct focusing and accelerating phase. The validity and usefulness of linear-fluid theory has been discussed in [LHZ05] thoroughly. The optimum wake was also found as $k_p\sigma_z = 2^{1/2}$ for $k_p\sigma_r \leq 1$ given fixed beam parameters where k_p is plasma wave number, σ_z and σ_r is longitudinal and transverse size of the beam respectively. In beam-driven case, the ratio of driver beam density and plasma density n_b/n_p determines if the regime is linear or blowout; Equivalently, the normalized vector potential of laser $a_0 = eA/(mc^2)$ is for laser-driven. When $n_b/n_p > 1$ or $a_0 > 1$, plasma wave goes to blowout regime where $\delta n/n_0 \approx 1$ which indicates almost all electrons inside the regime are blown out by the driver bunch. However, this condition is not absolutely necessary,

linear regime or quasi-linear regime can transit into blowout-regime due to self-focusing.

We have known the wave breaking limit from simple estimation above. It would be useful to explore properties of wakefields such as the relationship between transverse components and longitudinal component and the dependencies of each of them. *Panofsky-Wenzel Theorem* which was used to in scenario where a beam travels through a structure and generate a wave excitation when there are longitudinal and transverse momentum kicks. This theorem can be generalized to many structures such as RF deflectors. This structure can also be plasma. Here, we start to derive the theorem for single particle and then take a look at it in plasma acceleration example.

First, we write fields $\boldsymbol{E}$ and $\boldsymbol{B}$ in terms of the scalar and vector potential.

$$\boldsymbol{E} = -\nabla\phi - \frac{\partial \boldsymbol{A}}{\partial t} \tag{3.1}$$

$$\boldsymbol{B} = \nabla \times \boldsymbol{A} \tag{3.2}$$

Assume the particle's velocity direction is in $\hat{z}$, then

$$\boldsymbol{v} \times \boldsymbol{B} = v_0\hat{z} \times (\nabla \times \boldsymbol{A}) \tag{3.3}$$

For vector $\boldsymbol{a}$ and $\boldsymbol{b}$, we have

$$\nabla(\boldsymbol{a} \cdot \boldsymbol{b}) = \boldsymbol{a} \times (\nabla \times \boldsymbol{b}) + \boldsymbol{b} \times (\nabla \times \boldsymbol{a}) + (\boldsymbol{a} \cdot \nabla)\boldsymbol{b} + (\boldsymbol{b} \cdot \nabla)\boldsymbol{a} \tag{3.4}$$

Therefore, Equation 3.3 can be written as

$$v_0\hat{z} \times (\nabla \times \boldsymbol{A}) = \nabla(\boldsymbol{A} \cdot v_0\hat{z}) - \boldsymbol{A} \times (\nabla \times v_0\hat{z}) - (\boldsymbol{A} \cdot \nabla)v_0\hat{z} - (v_0\hat{z} \cdot \nabla)\boldsymbol{A} \tag{3.5}$$

The second and third term on the right hand side equal to zero. We arrive at

$$v_0\hat{z} \times (\nabla \times \boldsymbol{A}) = v_0\nabla A_z - v_0\frac{\partial \boldsymbol{A}}{\partial z} \tag{3.6}$$

While the full derivative of $\boldsymbol{A}$ is

$$\frac{d\boldsymbol{A}}{dt} = \frac{\partial \boldsymbol{A}}{\partial t} + (\boldsymbol{v} \cdot \nabla)\boldsymbol{A} = \frac{\partial \boldsymbol{A}}{\partial t} + v_0\frac{\partial \boldsymbol{A}}{\partial z} \tag{3.7}$$

Since $\boldsymbol{A}$ has no explicit dependency on time t,

$$v_0 \frac{d\boldsymbol{A}}{dz} = \frac{d\boldsymbol{A}}{dt} \tag{3.8}$$

Thus the Lorentz force can be written as

$$\boldsymbol{F} = q(-\nabla\phi + v_0\nabla A_z - v_0\frac{d\boldsymbol{A}}{dz}) \tag{3.9}$$

The total change of momentum $\boldsymbol{p}$ through structure can be expressed as

$$\Delta\boldsymbol{p} = q\int(-\frac{d\boldsymbol{A}}{dz} + \nabla(A_z - \frac{\phi}{v_0}))dz \tag{3.10}$$

For an isolated structure, $\boldsymbol{A} = 0$ because $\boldsymbol{E}$ and $\boldsymbol{B}$ vanish on the boundary.

$$\Delta\boldsymbol{p} = \nabla(q\int(A_z - \frac{\phi}{v_0})dz) \equiv \nabla\Omega \tag{3.11}$$

Thus, we have $\nabla\times(\Delta\boldsymbol{p}) = 0$, or equivalently

$$\nabla_\perp(\Delta p_z) = \frac{\partial(\Delta\boldsymbol{p}_\perp)}{\partial z} \tag{3.12}$$

[LHZ06] derived the theorem for plasma wake excitation case. In the paper, the pseudo potential is defined as $\bar{\Psi} = \bar{\Phi} - \bar{A}_z$ where $\bar{\Phi}$ is the electrostatic potential and $\bar{A}_z$ is the component of the vector potential in the direction of propagation. The coordinate system is chosen as $(\xi = z - v_\phi t, x, y, s = z)$ where v_ϕ is the phase velocity of the wake. The conclusion was $F_z \approx -\partial_\xi\bar{\Psi}$ and $F_\perp \approx -\nabla_\perp\bar{\Psi}$. Thus the Panofsky-Wenzel theorem can be written as

$$\nabla_\perp F_z = \partial_\xi F_\perp \tag{3.13}$$

It means the transverse variation of longitudinal component of wakefield equals to the longitudinal variation of transverse components of wakefield.

3.2 A brief history of PWFA

In this section, we will follow the timeline of the PWFA topic. The milestones of both theory and experiment but not exhaustively will be pointed out. As we mentioned above,

the idea of beam-driven scheme was proposed by P. Chen *et al.* In this paper, 1D linear regime simulations was shown to prove this could be promising candidate to achieve GeV/m-level acceleration gradient. After a couple of years, 2D simulation results were presented in [Kat86, SS87]. Issues such as dephasing of trapped particles and beam loading were addressed. Then J. Rosenzweig *et al* explored nonlinear regime and reported their theoretical studies of 1D plasma wave [Ros87, RBK91] . The nonlinear regime where electrons were all repelled to side, only ions were left as background later was known as "blowout regime". The beam loading issue for the "blowout regime" was developed in [TLT08] and shown that with appropriate beam shape, high energy transformer ratio and low energy spread can be achieved. Thanks to huge improvement of computing power, nowadays 2D cylindrically symmetric code and 3D boosted frame code such as OSIRIS and WARP are available so that we can model plasma problems more accurately.

Plasma wakefield acceleration were observed for the first time in experiment [RCC88]. The experiment was conducted in Argonne National Laboratory with 2 3 nC charge, 21 MeV, σ_r 2.4mm, σ_z 2.4mm electron driver bunch. The witness bunch following behind was 15 MeV and the gradient reported was about 1 MeV/m. Later on, the followup experiment was carried out to investigate accelerating and focusing properties of PWFA. Gradient of 5 MeV/m was measured and transverse focusing effect was observed [RSC89]. As proof of concept, these experiments demonstrated PWFA on MeV-level. In 1990s, experiment with 1 GeV energy gain was proposed [ACD98] and approved as E-157 experiment [HAD00, OSD02] at Final Focus Test Beam facility (FFTB) in SLAC National Accelerator Laboratory. The most famous one in FFTB was the tail of 42 GeV driver bunch was accelerated over 80 GeV with accelerating gradient of 54 GeV/m and plasma length of 80 cm [BCD07]. The energy was doubled in less than 1m long plasma which was astonishing. Besides this success, there were other interesting topic tested on FFTB. For example, the transverse properties of the blowout regime [CBD02], the X-ray radiation from beam betatron motion of electrons [WCB02] and positrons [JAB06], oscillation of witness beam due to initial offset injection known as "hosing instability" [DBC06].

3.3 Different injections

We already know there are PWFA and LWFA from last sections. There is another dimension to categorize plasma-based acceleration which is injection. Injection of background plasma electrons into the plasma wave, trapping them in the wave, and forming an electron bunch with compact six-dimensional phase space volume is a complex process presenting difficult challenges. Schemes that yield control over such characteristics, such as self-injection [MMN04, GTT04, FGP04, KBY11, KYB11, BPR12], density step injection [BNP98, SBR01, GNP08, SBS10, GNL11], multiple laser pulse injection [UKD96, EHL97, FRN06, DLR09], ionization-induced injection [CSM06, MTS10, CRA10, PCR11, LXW11], and combinations of these have been proposed and developed to varying degrees in recent years. For applications such as driving an x-ray free electron laser (XFEL), ultralow emittance and high current, with reproducibility and precise controllability over energy, are required. It has been shown recently that under certain circumstances the output from laser-plasma-accelerators may be already sufficient to yield the minimum conditions needed for FEL radiation production [MMR12]. However, a substantial increase in electron bunch quality is highly desirable for plasma-based accelerators, in order to increase the brightness of electron drivers for XFEL applications; this increase in brightness enables a dramatic decrease of the FEL footprint by shortening the FEL gain length, thus helping make a truly compact XFEL system [RAA08]. Further, use of lower emittance beams allows shorter wavelengths to be accessed [OMR10]. In next chapter, we will introduce a novel injection scheme: ionization injection.

CHAPTER 4

Ionization injection scheme PWFA
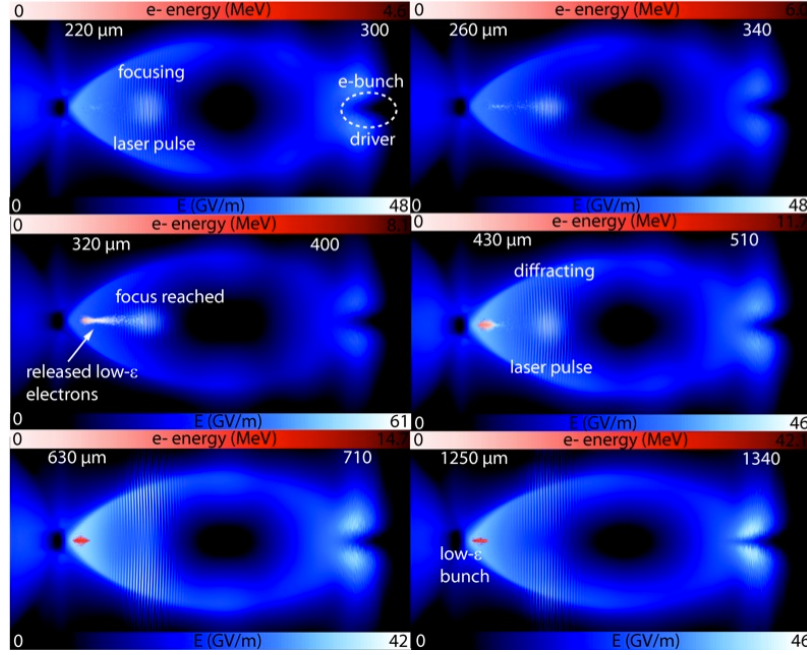
Figure 4.1: PIC simulation snapshots of photoionization release, trapping, and acceleration of electrons inside a bunch-driven, self-ionized plasma blowout. The copropagating laser pulse starts to release electrons as it approaches its focus. These low-emittance electrons are trapped at the back of the blowout and gain energy (red color bar). The blue and white colors show the sum of the electric field, which is necessary to indicate the bubble structure as well as the linearly polarized laser pulse electric field.

Recently, hybrid plasma accelerators [HKO10] have been described that promise to enable dramatically increased electron bunch quality by employing an underdense photocathode plasma wakefield mechanism [HRX]the equivalent of a solid photocathode in RF photoinjector guns [HBP94]. In particular, this hybrid injector scheme plasma accelerator (also known as Trojan horse injection [HPR12]) may produce bunches with normalized transverse emittance down to the $\epsilon \approx 10^{-2}$ mm mrad level or less. The essen-

tial ingredients of this novel concept are an intense, short pulse electron beam driver; a synchronized, relatively low-energy laser pulse; and a gas/plasma combination consisting of at least one low-ionization threshold (LIT) and another higher-ionization-threshold (HIT) atomic component. The electron beam driver is required to drive the plasma wakefield interaction into the blowout regime in the LIT medium. The synchronized laser pulse then follows the driving electron beam and is focused into the blowout cavity where it releases ultracold electrons via localized (within the laser Rayleigh length) ionization of the HIT gas. In contrast to todays laser wakefield acceleration schemes, where the terawatts-power-scale laser pulse sets up the plasma wave, here, the modest intensity laser pulse is required only to release electrons into the electron beam-driven plasma wakefield acceleration, in underdense photoionization action. The separation of function between driving of very large-amplitude plasma waves and the ionization injection between the electron beam and laser beam, respectively, gives a high degree of tenability in this approach.

Figure 4.1 illustrates this underdense photocathode plasma wakefield acceleration process based on particle-in-cell (PIC) simulations with VORPAL [NC04]. The electron bunch driver sets up the LIT plasma wave, and the laser pulse sets free electrons around its focus on an axis with ultralow emittance. These electrons are then caught and form a tiny, ultrahigh quality bunch that is copropagating with the plasma wave at the end of the blowout, thus profiting from maximized energy gain.

The dynamics of laser ionization-based electron injection in the recently introduced plasma photocathode concept is analyzed analytically and with particle-in-cell simulations. The influence of the initial few-cycle laser pulse that liberates electrons through background gas ionization in a plasma wakefield accelerator on the final electron phase space is described through the use of Ammosov-Deloine-Krainov theory as well as nonadiabatic Yudin-Ivanov (YI) ionization theory and subsequent downstream dynamics in the combined laser and plasma wave fields. The photoelectrons are tracked by solving their relativistic equations of motion. They experience the analytically described transient laser field and the simulation-derived plasma wakefields. It is shown that the minimum normalized emittance of fs-scale electron bunches released in mulit-GV/m-scale plasma wakefields is of the order of 10^{-2} mm mrad. Such unprecedented values, combined with

the dramatically increased controllability of electron bunch production, pave the way for highly compact yet ultrahigh quality plasma-based electron accelerators and light source applications.

In first section, we will discuss the mechanism of intense laser ionization and introduce a new model that calculates the ionization rate and simulate initial distribution of ionization electrons. Then we move on to study witness bunch behaviors with equations of motion derived from Chapter 2 and initial conditions we obtained from first section. Finally, we calculate emittance and brightness with solution of equations of motion after cm-scale acceleration.

4.1 High-intensity laser ionization
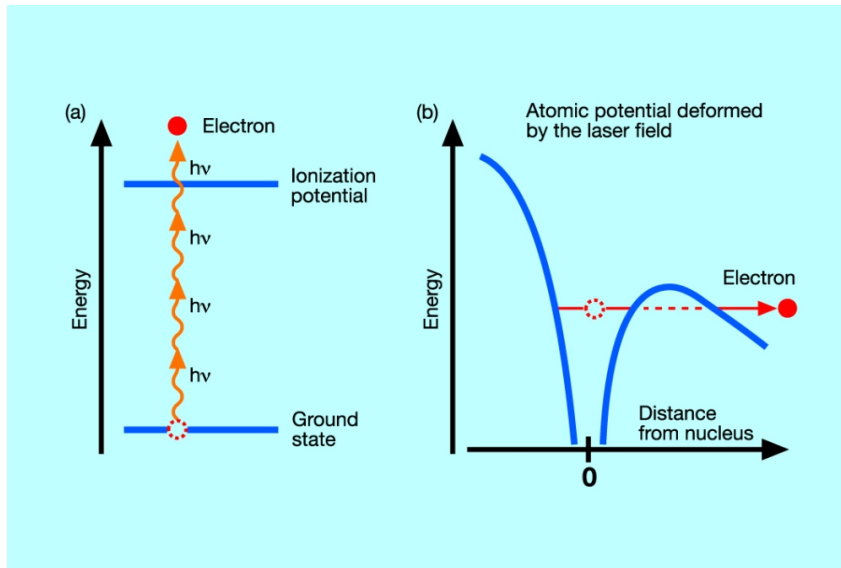
Figure 4.2: a) Electron jumps from ground state to free state by absorbing multiple photons. b) Atomic potential is deformed by intense laser field so that electron can tunnel out.

Due to wave-particle duality of light, the ionization process can be interpreted in two ways as shown in Fig. 4.2: Atoms absorb multiple photons and outmost layer electrons are ejected.This process is called *multiphoton ionization* (MPI) [DK98, Pop04]. On the other hand, ionization can also be seen as a quasi-static process in which strong laser field suppresses the potential barrier of ions and increases the probability for bound

electrons to tunnel through [NR66, AT66, AT67, A 67]. A more general quasi-static theory was developed by Keldysh [Kel65] to describe multiphoton ionization in the low-frequency limit, and was pursued by Faisal [Fai73] and Reiss [Rei80]. In his theory, the assumption has been made that an electron only interacts with laser field, not with ions after ionization. An important parameter *Keldysh parameter* γ_k was defined to measure the contributions of two competing processes . For $\gamma_k \ll 1$, tunnel ionization dominates over MPI, while $\gamma_k \gg 1$, ionization transit to MPI regime. It is interesting to note that early evidence of quasi-static tunneling was found in 1974 by Bayfield and Koch [BK74] in the microwave ionization of highly excited Rydberg atoms.

$$\gamma_k = (\frac{I_P}{2U_P})^{1/2} \tag{4.1}$$

where I_P is ionization potential of atom. U_P is electron ponderomotive energy, which is the cycle-averaged quiver energy of a free electron in an electromagnetic field, defined as

$$U_P = \frac{e^2 \mathcal{E}_0^2}{4m\omega^2} \tag{4.2}$$

Or more practically,

$$U_P[eV] = 9.34 \times 10^{-20} \times (\lambda[nm])^2 \times I[W/cm^2] \tag{4.3}$$

where m and e are the mass and charge of the electron. $\mathcal{E}_0$ is the electric field strength. ω is the angular frequency of laser. λ is laser wavelength. I is laser intensity. It is worth to point out that after plugging Eq.4.3 into Equation 4.1, we find γ_k is proportional to $\lambda\sqrt{I}$ which indicates high intensity, long wavelength end corresponds to tunnel ionization and low intensity, short wavelength refers to MPI. It is consistent with physics intuition that long wavelength laser behaves like wave while short wavelength laser is described as photons. To show the dependence of γ_k on intensity and wavelength, γ_k is plotted as function of intensity for various wavelength cases in Figure 4.3. For Ti:Sa laser (800 nm) in FACET, γ_k is below 1 over most of intensity range of interest which means tunnel ionization overweights MPI.
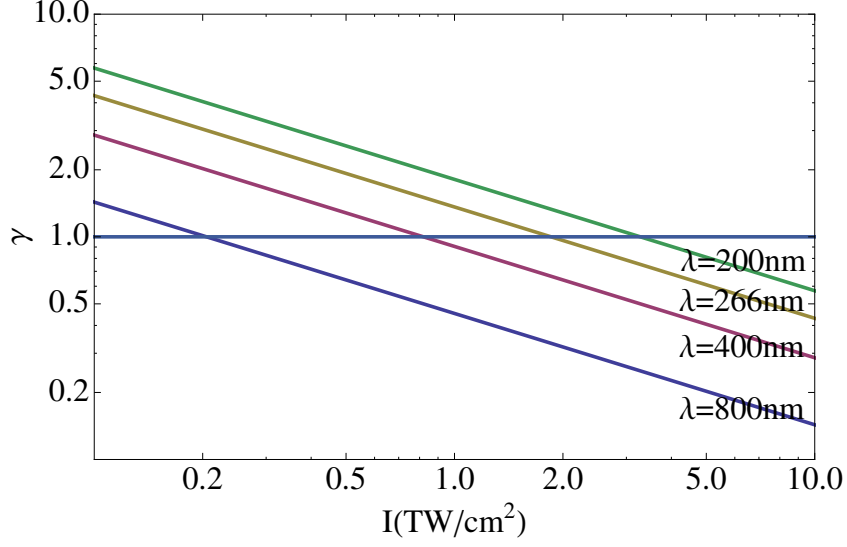
Figure 4.3: Dependence of γ on laser intensity I for λ=200nm, 266nm, 400nm, 800nm.

After introducing MPI and tunnel ionization, we focus on ionization rate in other words how many atoms can be ionized given gas density and certain laser pulse. For a long time, people have been using famous ADK formula to calculate the ionization rate which was named after three pioneers (Ammosov M. V., Delone N. B. and Krainov V. P.) [MK86]. In their theory, rates of laser ionization are averaged over the laser cycle and defined as

$$\Gamma(t) = A_{n^*,l^*} B_{l,|m|} I_P \left(\frac{2(2I_P)^{3/2}}{\mathcal{E}f(t)|cos\phi(t)|}\right)^{2n^*-|m|-1} \times exp\left(-\frac{2(2I_P)^{3/2}}{3\mathcal{E}f(t)|cos\phi(t)|}\right) \qquad (4.4)$$

where the coefficient A_{n^*,l^*} is related to radial part of wave function thus the effective principal quantum number n^* and the effective angular momentum l^*. The coefficient $B_{l,|m|}$ is from the angular part of the wave function and determined by actual angular momentum l and its projection m to laser polarization vector. I_P and $\mathcal{E}$ are ionization potential and laser electric field amplitude as mentioned above. $f(t)$ is temporal envelope function. $\phi(t)$ is the phase term.

$$A_{n^*,l^*} = \frac{2^{2n^*}}{n^*\Gamma(n^* + l^* + 1)\Gamma(n^* - l^*)},$$
$$B_{l,|m|} = \frac{(2l+1)(l+|m|)!}{2^{|m|}|m|!(l-|m|)!} \qquad (4.5)$$

32

where $\Gamma(x)$ is the gamma function. By choosing appropriate $f(t)$ and averaging over half laser cycle, one can obtain tunnel ionization rate formula.

It has been widely used because of its simplicity and well performance in the limit $\gamma_k \ll 1$. For example, it has been well-implemented into particle-in-cell simulation code [DG03]. However, as ultrafast laser technology has developed rapidly. Averaging over laser cycle starts to become invalid for few-cycle laser. In our ionization injection experiment, injection laser is designed as tens of microns long which is close to few-cycle laser. Also, if we select Helium as HIT gas, then the ionization potential is $I_P \approx 24.6eV$, and the corresponding ponderomotive energy $U_P = I/(4\omega^2)$ amounts to $60eV$ at a laser intensity of $I = 10^{15}W/cm^2$ and a central wavelength of $\lambda = 800\mu m$. With Equation 4.1, the Keldysh parameter can be calculated as $\gamma_k \approx 0.45$ in our experiment scenario. The intermediate Keldysh parameter $\gamma_k \sim 1$ indicates that bother tunnel ionization and multiphoton ionization are relevant. In such a case, the photoelectron yield from ionization is underestimated by ADK theory, especially with short wavelength laser pulses [GBL11], the use of which may be advantageous for our experiment. To estimate the yield of electrons released by laser more accurately, we need to find a more accurate model. G. L. Yudin and M. Y. Ivanov derived new ionization rate including dependence of ionization on the instantaneous phase of laser field [YI01].The expression of instantaneous rate is

$$\Gamma(t) \sim exp(-\frac{\mathcal{E}^2 f^2(t)}{\omega^3}\Phi(\gamma_k(t), \theta(t))) \tag{4.6}$$

where $\gamma_k(t) = \gamma_k/f(t)$ indicating now *Keldysh parameter* is time-dependent,

$$
\begin{aligned}
\Phi(\gamma_k, \theta) &= (\gamma_k^2 + \sin^2\theta + \frac{1}{2})\ln c - \frac{3\sqrt{(b-a)}}{2\sqrt{2}}\sin|\theta| - \frac{\sqrt{b+a}}{2\sqrt{2}}\gamma_k, \\
a &= 1 + \gamma_k^2 - \sin^2\theta, \\
b &= \sqrt{a^2 + 4\gamma_k^2\sin^2\theta}, \\
c &= \sqrt{(\sqrt{\frac{b+a}{2}} + \gamma_k)^2 + (\sqrt{\frac{b-a}{2}} + \sin|\theta|)^2}.
\end{aligned}
\tag{4.7}
$$

Figure 4.4 shows a snapshot of the spatial ionization probability distribution when the pulse is at focus. The ionization rate is a maximum at the center of the bi-Gaussian laser pulse profile, since the probability decreases sharply with intensity. Note that the ionization rate peaks every half-laser cycle, when the absolute value of the electric field
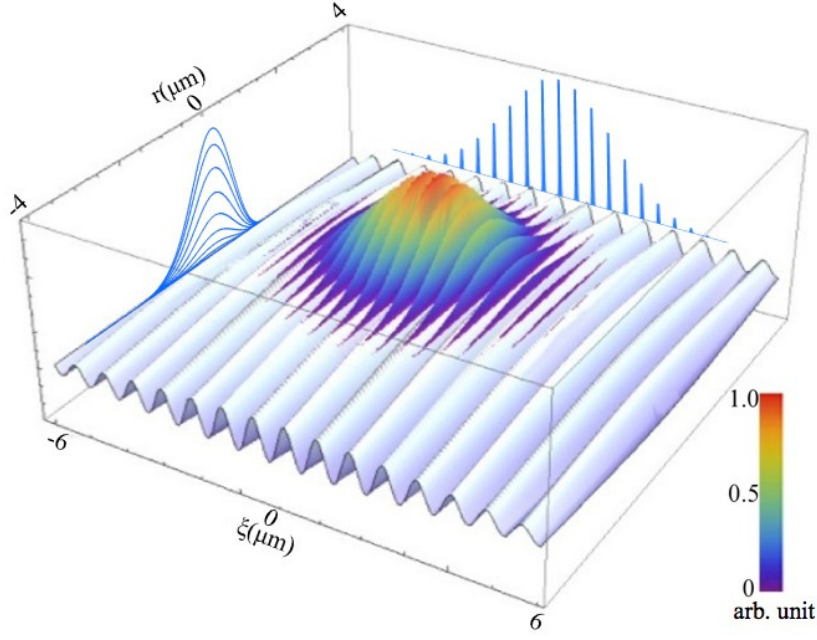
Figure 4.4: Visualization of laser-triggered ionization photoelectron yield. The color-coded elevation is the normalized ionization probability rate distribution inside the laser pulse, while the laser pulse profile is shown at the base. The probability distribution is also projected to show longitudinal and axial characteristics.

in the laser pulse and thus the atomic Coulomb potential barrier distortion reach local maxima.

The ionization probability rate Γ having units of $s^{-1}m^{-3}$ from nonadiabatic theory has, as a function of the laser field, an implicit spatial and temporal dependence [YI01]. The photoelectron yield is given as

$$N_e \approx n_{\mathrm{HIT}} \sum_{(z_w-z_r)/c}^{(z_w+z_r)/c} T/2 \int \Gamma(x,y,\xi,t)\,\mathrm{d}V \tag{4.8}$$

where N_e is the total electron number, n_{HIT} is the electron density of the HIT medium, and T is one complete laser cycle period. At each moment, the probability rate Γ is integrated over the laser pulse volume. In our numerical analysis, the probability is accumulated with a step size of $T/2$. As we are dealing with ionization near threshold, the release process is confined to one Rayleigh length around focus.

For example, in order to produce a charge of $Q \approx 1$ pC per laser shot, the probability

34

integral indicates that the laser intensity should be $I \approx 1.2 \times 10^{15}\,\mathrm{W/cm^{-2}}$.

4.2 Bunch dynamics in ionization injection scheme

Next, the electrons released via laser ionization are numerically injected into a laser and plasma field configuration, in which the laser fields are obtained from the prescription given above, and the plasma fields derived from 2D particle-in-cell simulations using the PIC code VORPAL. Due to relevance for the upcoming Facility for Advanced Accelerator Experimental Tests(FACET) experiment E-210: Trojan Horse at SLAC, the driver electron bunch parameters were chosen in the simulation to reflect FACET parameters: the electron energy $E \approx 23\,\mathrm{GeV}$, the bunch charge $Q \approx 1\,\mathrm{nC}$, and the longitudinal and transverse beam sizes are $\sigma_z = 20\,\mu\mathrm{m}$ and $\sigma_r = 15\,\mu\mathrm{m}$, respectively. Thus, the maximum FACET electron beam density is $n_b = Q/(2\pi)^{3/2}e\sigma_r{}^2\sigma_z \approx 8.8 \times 10^{16}\,\mathrm{cm^{-3}}$.

While the optimum blowout condition $k_p\sigma_z \simeq \sqrt{2}$ would indicate a desirable LIT plasma wavelength of $n_{\mathrm{LIT}} = 1.4 \times 10^{17}\,\mathrm{cm^{-3}}$ (assuming complete LIT medium ionization), such a high density would exceed the electron beam driver density and violate the blowout condition $n_b \gg n_{\mathrm{LIT}}$. Additionally, the sum of the laser pulse Rayleigh length and the driver bunch length would exceed the plasma wavelength $\lambda_{\mathrm{LIT}} \approx 89\,\mu\mathrm{m}$ in the higher plasma density case. This would imply that either the laser pulse front would interact with the driver bunch, or the electrons released by the back of the laser pulse would not be trapped in the first plasma wave bucket. To mitigate these effects, here a LIT plasma density of $n_{\mathrm{LIT}} \approx 5 \times 10^{16}\,\mathrm{cm^{-3}}$ is chosen, corresponding to $\lambda_{\mathrm{LIT}} \approx 149\,\mu\mathrm{m}$.

Figure 4.5 (left) gives color plots of the longitudinal electric field E_z, the transverse electric and magnetic field E_r and B_ϕ, respectively, as obtained using VORPAL simulations for the bunch-plasma interaction with the parameters discussed above. The driver bunch (not shown) moves to the right in these figures, and the position of the laser pulse (also not included of the VORPAL simulations, which are intended only to furnish self-consistent plasma wakefields driven by the intense electron beam), is indicated with the reddish ellipse. The right hand side of the figure shows lineouts of relevant fields taken at the three different longitudinal positions in the excited blowout. It can be seen that in the area of interest, the transverse wakefields have excellent linearity
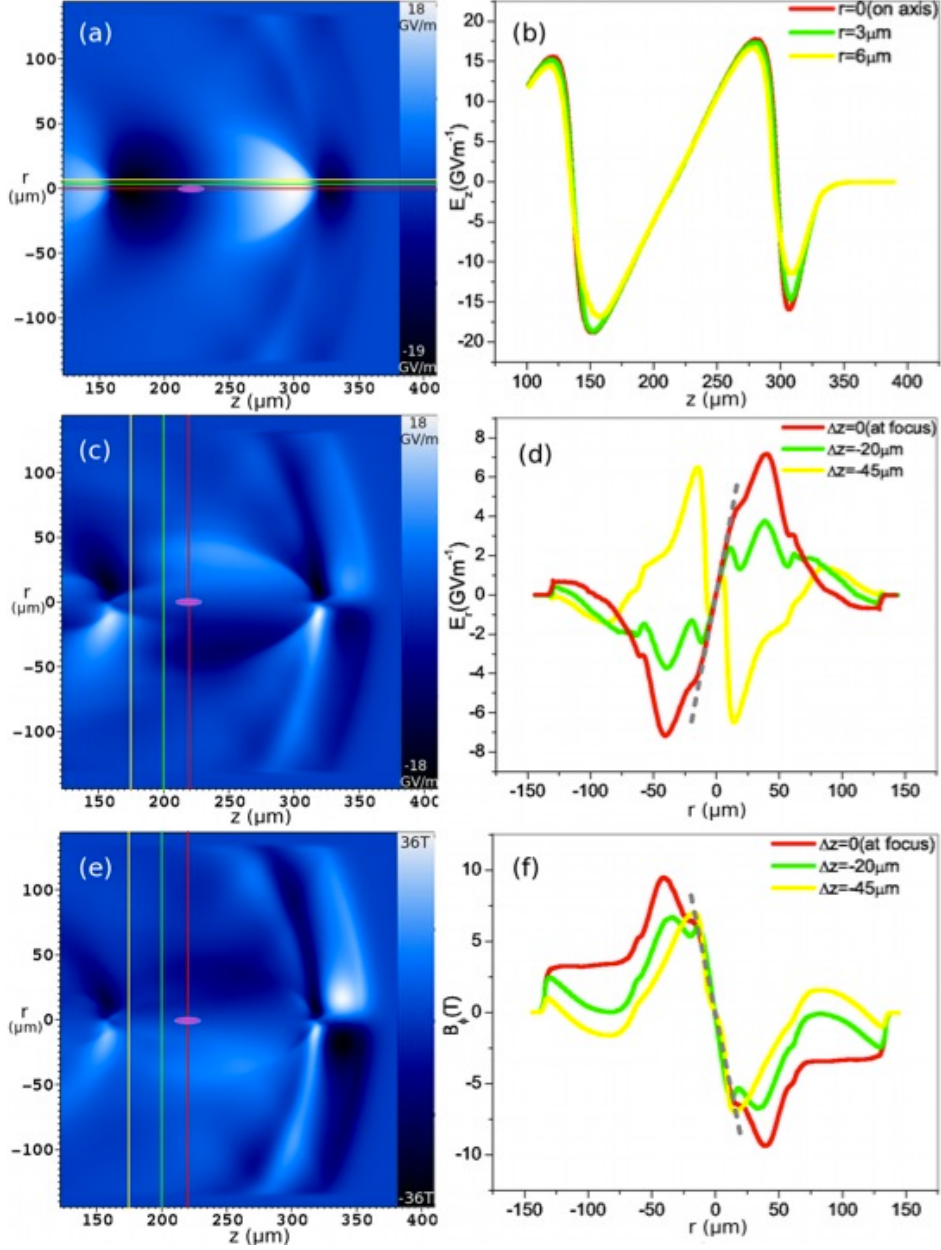
Figure 4.5: VORPAL simulation results of the plasma wakefields acting on the released electrons. The left three figures (a), (c), (e) are color plots of the spatial distribution and intensity of wakefields E_ξ, E_r, B_ϕ, respectively, while the right three figures (b), (d), (f) are lineout plots of the fields at the indicated positions. While the corresponding simulation did not include the laser pulse, the laser pulse position of the laser pulse assumed in the numero-analytical analysis is indicated by the reddish ellipse.

and symmetry in the center of the blowout region: the electric radial component E_r and magnetic azimuthal component B_ϕ are proportional to r, thus providing for minimum

emittance growth due to the wakefield itself. Additionally, the electric longitudinal component E_ξ is linear with ξ, where $\xi = z - v_{pw}t$, which is optimum for management of longitudinal oscillations, implying that the longitudinal emittance due to the wakefields is minimized. The motion of the LIT electrons is governed by the rLorentz force relation $d(\gamma m \mathbf{v})/dt = -e(\mathbf{E} + \mathbf{v} \times \mathbf{B})$ and energy equation $d\gamma/dt = -e\mathbf{v} \cdot \mathbf{E}/mc^2$, where γ is the relativistic Lorentz factor $1/\sqrt{1 - v^2/c^2}$. The time t is normalized to the inverse of the laser frequency ω, and x, y, z are normalized to the inverse of the laser wave number k. These choices in turn imply that the velocity $\boldsymbol{\beta}$ is normalized to c. Immediately after being released from the HIT atoms, HIT electrons are exposed to both the laser fields $\mathbf{E}_l$ and $\mathbf{B}_l$ and plasma wakefields $\mathbf{E}_w$ and $\mathbf{B}_w$, where w and l denote wakefield and laser field. Since the LIT plasma electron density is practically zero inside the blowout, and the ions are quasistatic, there is no plasma response to the laser pulse (which is in diametral contrast to laser wakefield acceleration secenarios). Therefore, the plasma and laser fields can simply be superimposed. Then, when the laser pulse has passed, the electrons are affected only by $\mathbf{E}_w$ and $\mathbf{B}_w$. For simplicity, $\mathbf{E}$ and $\mathbf{B}$ are normalized to dimensionless (vector potential amplitudes) $\mathbf{a} = e\mathbf{E}/m_e\omega c$ and $\mathbf{b} = e\mathbf{B}/m_e\omega$, respectively. In summary, the equations of motion equations are rewritten as $\gamma d\boldsymbol{\beta}/dt = \mathbf{Va} + \boldsymbol{\beta} \times \mathbf{b}$ where

$$
V \equiv \begin{pmatrix} \beta_x^2 - 1 & \beta_x\beta_y & \beta_x\beta_z \\ \beta_x\beta_y & \beta_y^2 - 1 & \beta_y\beta_z \\ \beta_x\beta_z & \beta_y\beta_z & \beta_z^2 - 1 \end{pmatrix}
$$

The laser pulse begins ionization of HIT (He) atoms within roughly a Rayleigh length before it reaches the focal point and the entire ionization process may thus last 100's of femtoseconds, which leads to betatron phase mixing, and thus emittance growth, through the difference in initiation of the betatron focusing oscillation. Figure 4.6 shows trajectories of He electrons launched randomly in the path of the laser pulse with probability proportional to the instantaneous, local ionization rate. The top plot shows the variation of velocity in x (the laser polarization) direction, while the bottom plot shows that in y direction. Each electron track initiates with an oscillation due to ponderomotive motion within the laser pulse, which disappears after passage of the laser pulse. Simultaneously, electrons also undergo relatively slow betatron oscillations because of restoring transverse
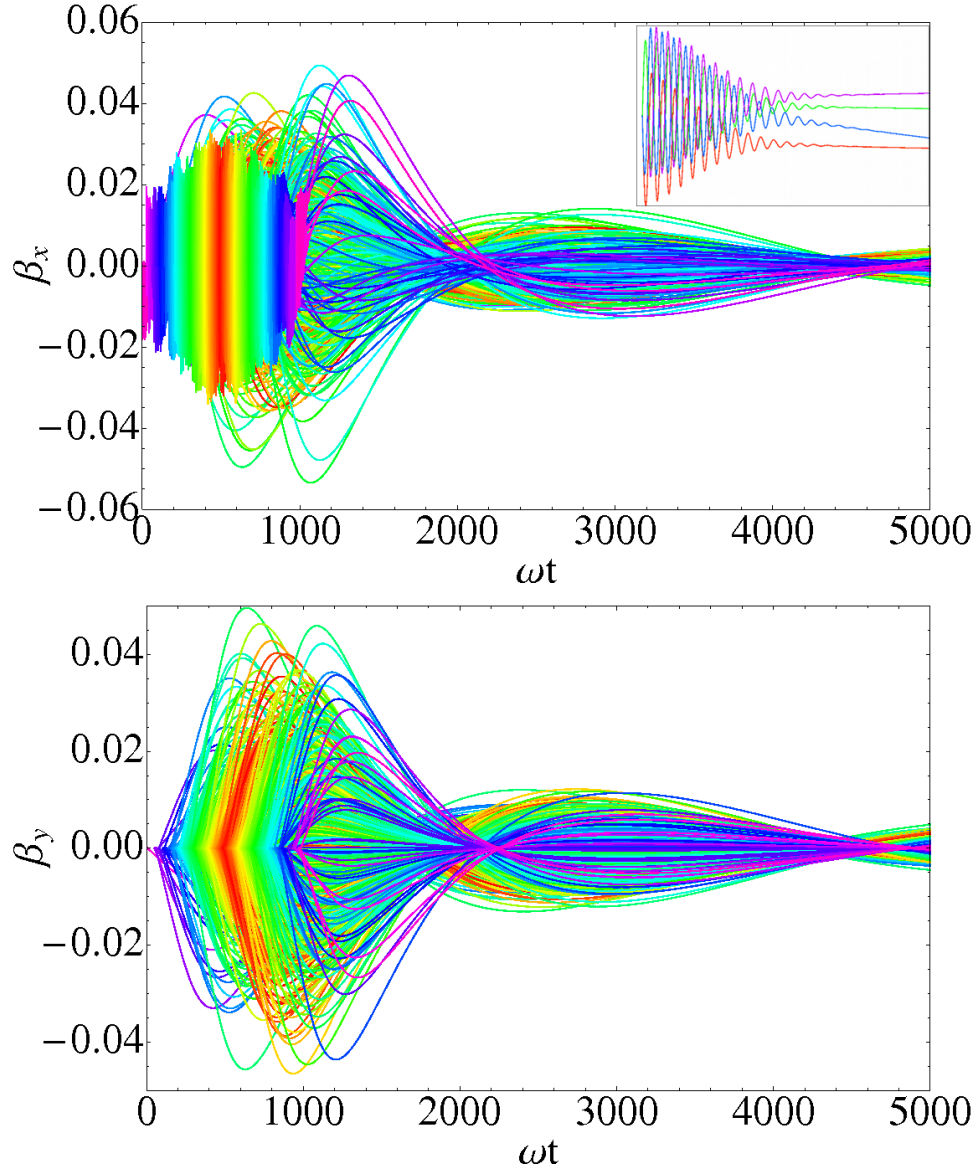
Figure 4.6: Electron motion in x (polarization) and y direction are shown in plots at top and bottom, respectively. The inset is a zoom-in of ponderomotive motion tracks. The tracks are color-coded according to electron density from red (maximum) to magenta (minimum).

wakefield, which is due almost entirely to ion-column focusing in the electron-rarefied region of the blowout. While the oscillatory part of the ponderomotive motion tends to vanish as laser pulse passes, the laser leaves a remnant transverse "kick". This momentum impulse may be estimated well by calculation of the initial canonical transverse momen-

tum, which is proportional to the laser vector potential at the time and position of the HIT electron release. In contrast, in the y direction, where this vector potential vanishes due to the assumed laser polarization, the beam spread in transverse momentum at a given position in z is only caused by betatron phase mixing. All electron betatron oscillations have a unique starting position. This elimination of laser-induced momentum in the y-direction gives the possibility of observing and quantifying phase mixing separately from the direct laser-induced momentum due to the laser seen in x direction.

4.3 Emittance analysis

This ionization injection has been shown in simulations to yield beams with high current (hundreds of amperes) and unprecedentedly low emittance; these are high brightness beams with very strong promise as new-generation XFEL drivers. For an investigation of the underlying physical mechanisms limiting the performance of this scheme it is instructive to consider first the sources of emittance in conventional photo injectors, in which electrons are liberated from photocathodes embedded in high field radio frequency (RF) cavities. In traditional photoinjectors, there are three contributing factors to the electron beam emittance: those from thermal-like effects, time dependent RF field effects, and collective space charge forces [Kim89]. When photoinjector systems are optimized, particularly at low charge, one is left with an emittance dominated by thermal effects. This emittance is proportional to the beam RMS transverse size $\sigma_{x,y}$ injected at the cathode and also the thermal spread in transverse momenta. In a plasma photocathode, an analogous effect to the thermal emittance contribution arises from the transverse momentum obtained during the initial interaction with the ionizing laser pulse. One may profitably view this mechanism as the dressing of the electrons at birth by the canonical electromagnetic momentum associated with the laser. Similarly, there are subsequent time-dependent field (both plasma and laser) and space charge effects to be considered after establishing the minimum laser-induced emittance ϵ_l.

In Trojan horse plasma wakefield acceleration scenarios, the electrons are accelerated in multi-GV/m fields, thus helping to mitigate space charge effects through extremely quick transit of non-relativistic energies. These fields also enable production of few- or

even sub-fs scale duration electron beams with non-negligible (pC-level) charge, thus yield high current beams needed for application. Also, in direct relevance to the present investigation the fields support formation of small electron bunch size $\sigma_{x,y}$, permitting minimization of $\epsilon_{x,y}$. All of these characteristics thus are affected by the ionization laser parameters. It is thus critical to understand the parametric dependences of fundamental processes involved in laser ionization, which occur in the environment of external plasma fields. The multi-disciplinary investigation of these issues involves a detailed understanding of a variety of physical effects arising from an impressive number of disparate fields: plasma physics, (relativistic) beam physics, atomic physics, and optical science.

We are thus searching to determine the dependences of $\epsilon_{\text{lx,ly}}$, which in contrast to the minimum emittance in photocathode devices, typically has both strong thermal and time-dependent characteristics. Indeed, laser ionization contributes to factors in the emittance in two proportional ways: through the electron off-axis positions (x, y) and the net momenta (p_x, p_y) obtained from the oscillating laser pulse field after release of the electron from the atomic species. Ionization theory is used to provide information about the initial conditions of electrons in phase space, using the analytical fields of the laser near its focus. Subsequent electron trajectories are obtained by solving their equations of motion under the applied forces, using analytical laser fields and simulation-derived plasma fields.

The transverse normalized emittance is defined as $\epsilon_x = (\langle x^2 \rangle_N \langle p_x^2 \rangle_N - \langle x p_x \rangle_N^2)^{1/2}/m_e c$ and $\epsilon_y = (\langle y^2 \rangle_N \langle p_y^2 \rangle_N - \langle y p_y \rangle_N^2)^{1/2}/m_e c$, where x, p_x and y, p_y are the transverse Cartesian off-axis positions and momenta, respectively, and $\langle \rangle_N$ denotes the average over all generated photoelectrons at a given position in the nominal propagation direction z. To evaluate the laser-induced momenta, we study the case in which the laser electric field is linearly polarized in x direction. The momenta of electrons from tunneling are assumed to be negligible[KSK92, Cor93], thus the momentum distribution arises purely from electrons-laser interaction and macroscopic plasma fields.

As an initial approximation, one may posit that most of the ionization processes occur when the oscillating laser electric field peaks, since the ionization rates decrease dramatically as the electric field amplitude decreases. Further, ionization in vicinity of the field maxima corresponds to the vicinity where the initial vector potential $\mathbf{A}_{ini} = 0$.

This in turn implies that the canonical momentum in x (and thus the residual momentum left after laser passage) is minimized, as is the associated mean drift energy $\mathcal{E}_{ini} = e^2 \langle \mathbf{A}_{ini}^2 \rangle_T / 2m$, where $\langle \rangle_T$ denotes taking average over one laser cycle. Here, the laser pulse is linearly polarized in the x-direction for the sake of simplicity.

Since the electric field of the laser pulse oscillates only in the x-plane, there is no initial canonical momentum contribution in y direction due to the laser pulse, and a non-vanishing ϵ_y arises only from the spatial (z)-dependence of the ionization, an effect that is not present in RF photo. This effect, which is accounted for in our calculations below, yields $\epsilon_y \ll \epsilon_x$. These initial considerations support the possibility of generating ultralow emittance beams.

In the following, the ionization of HIT atoms and characteristics of the photoelectrons released in the blowout region are analyzed in detail theoretically. The spatial distribution of photoelectrons in the focus is discussed on the basis of non-adiabatic ionization theory. Subsequently, the motion of the electrons in the combined laser field and accelerating and focusing wakefield in the blowout regime is analyzed numerically. The motion of photoelectrons is tracked and the development of aspects of the captured beam, in particular its emittance, are predicted. Due to their superior short pulse capabilities, Ti:Sapphire lasers are ideally suited to ionize HIT atoms for production of the captured beam. In case of helium as HIT medium, which from an experimental view is an appropriate choice since it is present as buffer gas in lithium ovens used for many existing, successful PWFA experiments [BCD07] and is also an attractive HIT candidate in environments where both LIT and HIT media are gaseous at ambient conditions [HPR12], the minimum required intensity of the ionization laser is of the order of 10^{15} W/cm^{-2}. A focus size of $w_0 = 4\,\mu$m is chosen as nominal, which corresponds to a Rayleigh length (and thus roughly the longitudinal extent of the ionization region) of $z_r = \pi w_0^2 / \lambda \approx 63\,\mu$m. The laser pulse duration τ_L may also have an effect on the bunch emittance, by spreading the initial launch phases inside of the wave. Taking into account the availability and parameters of typical short pulse Ti:Sapphire lasers, $\tau_L = 32\,$fs (FWHM) is considered in all of our design examples, with the exception of a parametric study that explores the effects of laser pulse length explicitly.

The time-dependent electromagnetic laser field amplitude is written as

$$E_x = E_0 \frac{w_0}{w(z)} \exp(-\frac{r^2}{w(z)^2}) \exp(-\frac{(t - \frac{z-z_w}{c})^2}{2\tau^2})$$

$$\cos\phi, \tag{4.9a}$$

$$E_z = 2E_0 \frac{w_0}{w(z)} \frac{x}{kw(z)^2} \exp(-\frac{r^2}{w(z)^2}) \exp(-\frac{(t - \frac{z-z_w}{c})^2}{2\tau^2})$$

$$(\sin\phi - \frac{z}{z_r}\cos\phi), \tag{4.9b}$$

$$B_y = E_x/v_{ph,l}, \tag{4.9c}$$

$$B_z = E_z/v_{ph,l}, \tag{4.9d}$$

where z_w denotes the focus position, $w(z) = w_0(1 + (z - z_w)^2/(z_r)^2)^{1/2}$ is the width of pulse at z, $\phi = kz - \omega t + \frac{r^2}{w(z)^2}\frac{z}{z_r} - \zeta(z)$ is the phase, the laser phase velocity $v_{ph,l}$ is near c, and $\zeta(z) = \arctan(z/z_r)$ is the Guoy phase shift. To satisfy Maxwell's equations $\nabla \cdot \mathbf{B} = 0$ and $\nabla \times \mathbf{E} = 0$, the axial field components are included, although for our chosen laser parameters they are approximately two orders of magnitude smaller than the transverse components.

Since electrons tunnel the potential barrier in less than the 50 attosecond [Buc07, LWM14], on timescales small compared to a laser cycle $\tau_{\mathrm{cyc}} \approx 2.7$ fs, each ionizing process can be well-approximated as instantaneous, and a prompt ionization rate distribution based on the laser intensity as it passes near the focus can be assumed. Further, since the electron release should take place relatively close to the center of the blowout to obtain suitable capture dynamics, both the transverse as well as the longitudinal electric fields arising from plasma response are near zero, it can be assumed that the plasma wakefield itself plays a negligible role during ionization.

4.4   Emittance and Brightness Results

To evaluate normalized transverse beam emittance statistically, we rewrite transverse emittances as

$$\begin{aligned}
\epsilon_x &\approx \gamma\beta\sqrt{\langle x^2\rangle\langle x'^2\rangle - \langle xx'\rangle^2} \\
\epsilon_y &\approx \gamma\beta\sqrt{\langle y^2\rangle\langle y'^2\rangle - \langle yy'\rangle^2}
\end{aligned} \tag{4.10}$$
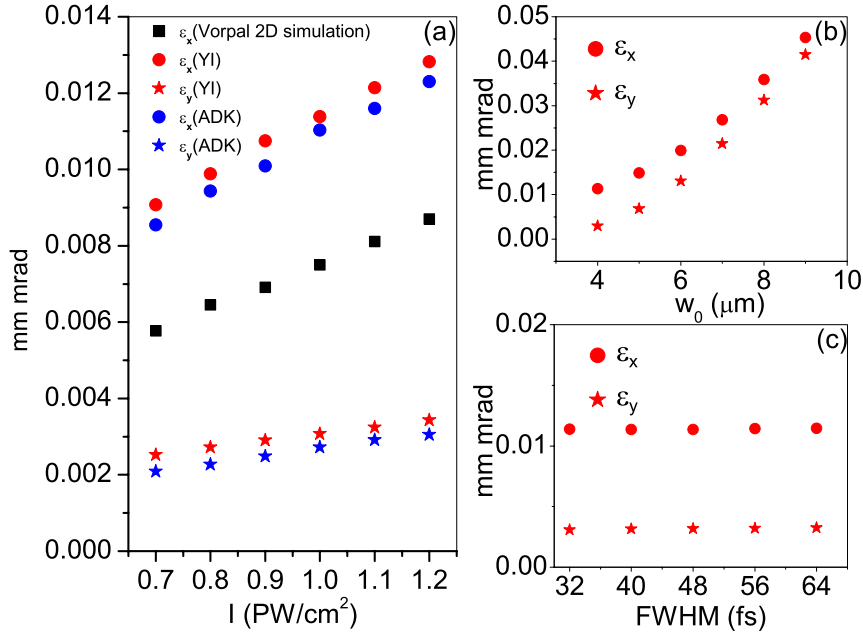
Figure 4.7: Laser pulse parametric study of emittance. The plot (a) displays the increase of emittance with laser intensity both in x direction (dot) and in y direction (star). ADK theory (blue) and YI model (red) are compared with results from VORPAL simulation(black square). Note that ϵ_y is excluded due to 2D simulation. At a fixed intensity of $I = 1\,\mathrm{PW/cm^{-2}}$, the top and bottom plots on the right show effects of beam waist w_0 and pulse duration FWHM on emittance, respectively.

where the ray angles x' and y' are defined as v_x/v_z and v_y/v_z, respectively. We investigate the emittance of the beam, which by convention requires use of the position and momentum information of electrons at the same z position, as opposed to a constant time t. After the injected beam bunch has completed its interaction with the laser pulse, the beam emittance ϵ_x tends to be stable, as one expects given that the dominant force is a linear ion-focusing transverse wakefield. Thus the only increase in emittance would arise from weak chromatic effects due to the finite energy spread in the beam.

As can be seen in Figure 4.7(a), the resulting normalized emittance ϵ_x and ϵ_y are of the order $10^{-2} \sim 10^{-3}\,\mathrm{mm\,mrad}$. The emittance in the dimension orthogonal to the laser polarization ϵ_y, is found to be, for the parameters we have chosen, about one order of magnitude lower than ϵ_x, as it only has ϵ_{mix} component. Both quantities increase

43

approximately linearly with laser intensity I in the parameter range of interest. To explain this result, we emphasize that the beam emittance ϵ_x caused by the laser being polarized in x-direction has two contributions: interaction with laser, and betatron phase mixing which are denoted as ϵ_{int}, ϵ_{mix}, respectively. The contribution ϵ_{int} should scale linearly with I because both x and p_x due to ponderomotive motion are proportional to the electric field amplitude E_0. The linearity of ϵ_{mix} is numerically obtained by calculating $\langle x^2 \rangle = \int x^2 \Gamma(x, y, \xi, t)\, \mathrm{d}V \mathrm{d}t / \int \Gamma(x, y, \xi, t)\, \mathrm{d}V \mathrm{d}t$. In the numerical determination of the emittance, both ADK theory and the YI model have been utilized to compare with 2D simulation. We note that ADK theory has been adopted to deal with laser field ionization in VORPAL framework. Also, space charge effects have been included in simulation even though it is negligible in our scenario, as discussed below. A possible reason for the lower emittance seen in simulation could be the linearization of the transverse wakefield in modeling. In addition, the emittance predicted by the YI model is slightly higher than that indicated by ADK theory, for the reason that the multiphoton ionization included in YI model affects the distribution at the extrema of the laser fields more.

Similarily, we have analyzed the influence of laser waist w_0 on beam emittance. The emittance from laser interaction can be estimated as $\epsilon_{\text{int}} \propto w_0$ while ϵ_{mix} is related to w_0^2 due to w_0^2 factor in Rayleigh length definition. Therefore, beam emittances grow quadratically with the laser pulse waist (Figure 4.7(b)). Additionally, as the laser waist increases, the contribution to the emittance due to phase mixing starts to dominate. Consequently, ϵ_x and ϵ_y tend to equalize for large waist size.

On the other hand, the laser pulse duration does not affect beam emittance as significantly as the laser intensity and waist (Figure 4.7(c)). Certainly, pulse duration plays no direct role in ϵ_{int}. Also, the degree of phase mixing is determined by Rayleigh length z_r, given the situation where $z_r \gg c\tau_L$, not by pulse duration. This implies that for experimental designs that the requirement for laser compression to very short pulses is not critical.

When self-field effects due to space charge are included, as will be the subject of future work, the emittance would be expected to exceed the laser-derived emittance alone, particularly at higher bunch charge. It should be pointed out, however, that the existence of very strong ion focusing implies that space-charge effects are secondary, as

the distortions in the transverse momentum distribution due to space-charge forces are negligible in amplitude compared to those due to the betatron oscillations arising from the ion restoring force. One may, in the context of near-equilibrium transverse (axisymmetric) beam propagation in the blowout regime, define the ratio of space-charge-to-emittance effects in the transverse rms envelope equation as

$$R \simeq \frac{I\lambda_p}{\sqrt{8}\pi I_0 \gamma^{3/2}\epsilon_n} \tag{4.11}$$

where $I_0 = ec/r_e \simeq 17\,\mathrm{kA}$. This ratio at the exit of a standard photoinjector ($\gamma \simeq 10$), in which notable space-charge induced emittance oscillations must be controlled by the emittance compensation process [SR97], reaches the range 100-1000. For our case, in contrast, $R \simeq 0.13$, indicating that the space-charge-induced emittance growth is of secondary concern.

A further implication of the strong focusing and ultra-low emittance of the captured beam in the plasma photocathode injector is that the beam density may be extremely large. This space-charge density in turn may cause ion motion, and concomitant emittance growth due to nonlinear ion-derived fields [RCS05]. Indeed, the captured beam density exceeds that of the plasma even at $\gamma = 10$ by over two orders of magnitude. Nevertheless, since the beam is very short compared to λ_p, and the mass of the LIT ions exceeds that of the electrons by 1.4×10^3, the ion motion should be negligible. In our example, even at high energy ($\gamma = 10^4$), the phase advance of the oscillating ions in the beam's potential well over the beam length $k_i L_b \simeq 6 \times 10^{-2}$ is negligible.

The evolution and characteristics of the beam's longitudinal phase space have also been studied. Figure 4.8 shows the evolution of the beam's longitudinal phase space distribution, commencing from the completion of ionization. The observed clockwise rotation of distribution is characteristic of pulse compression as the beam propagates. Beam length $L_b \simeq 2.5\,\mu\mathrm{m}$ after significant compression, with pC-level charge, which gives 100 A-level peak current.

The beam brightness, $B \approx 2I/\epsilon_x\epsilon_y$, can be estimated accounting for only the laser-induced emittance, as is our emphasis in this paper. Given the longitudinal extent of the beam from modeling and bunch charge yield obtained from Eq.4.8, a parametric study of beam brightness is listed in Figure 4.9: Frame(a) mostly reflects the effect of charge yield
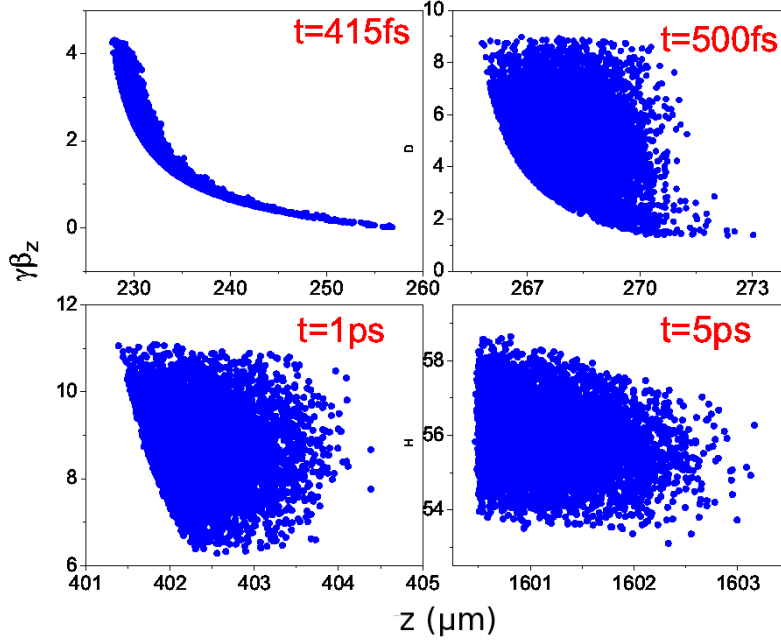
Figure 4.8: Snapshots of beam longitudinal phase space at $t = 415\,\mathrm{fs}, 500\,\mathrm{fs}, 1\,\mathrm{ps}, 5\,\mathrm{ps}$. The first figure corresponds to the moment when the ionization is completed.

since emittances are roughly equal from two models; The growth of emittance outweighs the increase of charge yield in Figure 4.9(b); The variation of pulse duration(Figure 4.9(c)) does not change either the emittance or the charge yield. The brightness values estimated here exceed that of the state-of-the-art Linac Coherent Light Source(LCLS) photo injector beam [ADE08] by a wide margin, indicating that the beam is a promising candidate for driving a compact FEL, with a gain length notably shorter than that obtained with photoinjectors. In this regard, we note that the RMS slice energy spread in our example is approximately $\sigma_U \approx 0.5$ MeV and so for an XFEL with, for example 10 GeV energy, the dimensionless gain parameter should exceed the relative slice energy spread, $\rho > \sigma_U/U \simeq 5 \times 10^{-4}$. Indeed, given current undulator technology, the beam resulting from our analysis should enable an optimized XFEL system to reach this value of ρ.
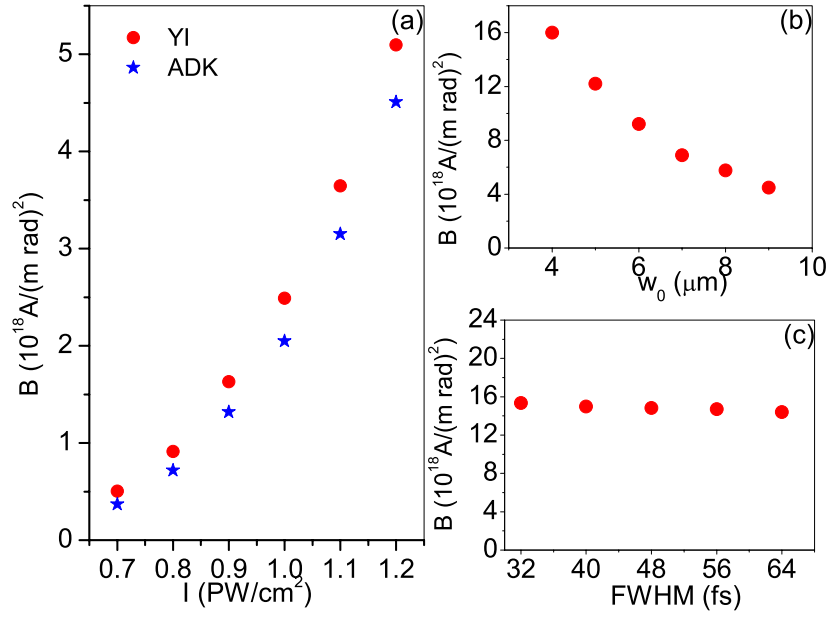
Figure 4.9: The dependence of beam brightness on laser intensity, laser waist, pulse duration are shown in (a), (b), (c) respectively.

CHAPTER 5

Ionization injection PWFA at FACET

5.1 Experiments at FACET

The idea of plasma wakefield acceleration has been tested in SLAC National Laboratory for a long time. Back in 2000s, experiments such as E-157, E-162, E-164 and E-167 at the Final Focus Test Beam (FFTB) facility proved that tens of GeV electron beam can be accelerated and focused through plasma [Cha03, MH09, Jos07]. One of remarkable results is using 42 GeV drive electron beam to generate 85 cm long, 50 GeV/m accelerating wakefields [BCD07]. Electrons at the tail of the drive bunch are observed to have double energy gain.

After FFTB, a new facility, Facilities for Accelerator science and Experimental Test beams (FACET) has been constructed. The main goal is to deliver high-energy, high-peak-current, low-transverse-emittance electron/positron beams to the continuing development of PWFA. With this beam condition, PWFA is expected to yield higher-energy-gain output beam while preserving the low beam emittance. The design parameters of the electron beam from FACET are listed in 5.1. As shown in Figure 5.1, FACET experimental area is located at Sector 20, upstream 2km of LINAC. Sector 20 beam line consists of a chicane, which has four dipole magnets to compress the beam longitudinally followed by an arrangement of quadrupole magnets to focus the beam to an interaction point. A new beam dump is near the end of Sector 20 where exists the LCLS injector.

Besides the upgrading of e-beam, FACET also installed a 10 TW Ti:Sapphire laser system starting from 2013. The main purpose of the laser is to pre-ionize the neutral gas to create wider plasma column, especially for higher-ionizing-threshold gas such as H_2 compared to Lithium gas. Meanwhile, FACET laser plays different roles in many experiments. For our experiment (E-210), a portion will be used as injection laser for

beam energy	20.35 GeV
bunch charge	3 nC
shortest bunch length	30 μm
transverse dimensions at IP	30 μm $\times$ 30 μm
β-function	0.15 m $\times$ 2.0 m

Table 5.1: FACET electron beam design parameters
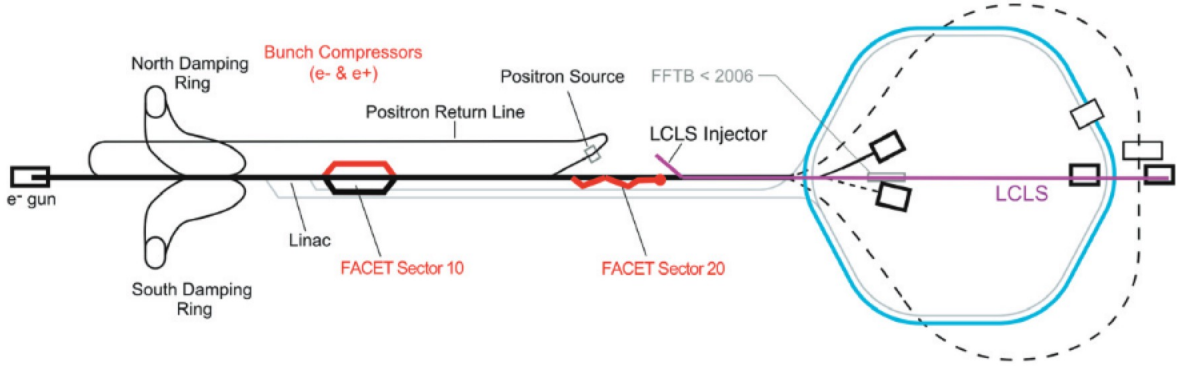
Figure 5.1: Layout of LINAC with FACET updates in red. The experimental area is at Sector 20.

ionizing He and also as a probe to synchronize laser and electron beam. The whole laser system consists of these major components: Verdi pump laser, Vitara Oscillator, Evolution pump laser, Legend Elite regenerative amplifier, FCR-200 Flashlamp-Pumped Nd:YAG laser and two saga 2 Flashlamp-Pumped Nd:YAG lasers. Starting from laser room, laser travels across the gallery and is reflected down to tunnel for multiple uses. The total transport line length is about 28 m. Then the laser goes through a compressor box with compression range from 70 fs to 150 ps. The main laser parameters are shown in the table 5.2.

5.2   Plasma source

Plasma source has been an important issue since FACET project was proposed. Before 2014, Lithium oven was installed and lithium was heated to create neutral gas. Due to

wavelength	800 nm
pulse duration (shortest)	70 fs
pulse energy in tunnel	300 mJ
spot size	1 inch

Table 5.2: FACET laser parameters

its low ionizing threshold, FACET electron beam can ionize the gas easily with main laser pre-ionization through an axicon. The idea of axicon was first proposed in [McL54]. In schematic 5.2, the depth of focus L_f can be calculated from geometry of the lens. $L_f = (R_2 - R_1)((tan\beta)^{-1} - tan\gamma)$ where the exit angle β is $arcsin(n_a sin\gamma) - \gamma$. The radial beam width of the focus is from zeroth order of Bessel function. $R_B = 2.4048/k_0 tan\beta \approx 2.4048/k_0\beta$. However, the secondary ionization of Li^+ ion background increases additional electrons trapping, thus spoiling the witness beam quality. Therefore, we replaced Lithium oven with a sequence of cubes and filled the whole experiment area with higher-ionizing-threshold H_2 gas. With the old axicon setup, the width and length of plasma column was reduced significantly.
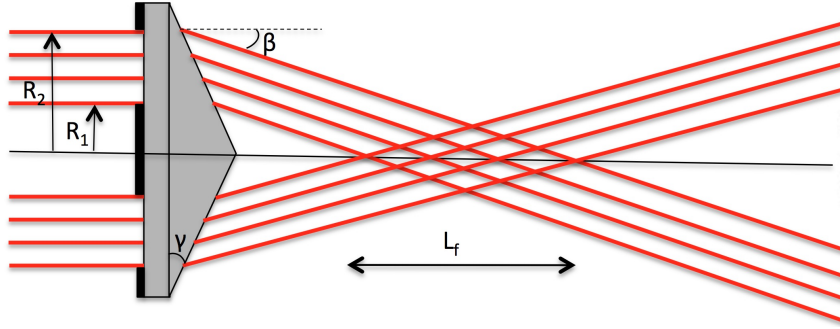
Figure 5.2: Main laser goes through an axicon with a mask at center and is line-focused in H_2 to generate a plasma column.

To make full use of laser energy, holographic axilens was installed to achieve high lateral resolution and long depth of focus simultaneously [DFH91]. As shown in Figure 5.3, the theoretical result from simulation agrees very well with preliminary experimental result. Axilens can generate much wider plasma column where the maximum width is about 250 mm while the axicon is only 90 mm under the same circumstance. Therefore, the axilens can provide sufficiently wide plasma column for plasma wakefield experiment.
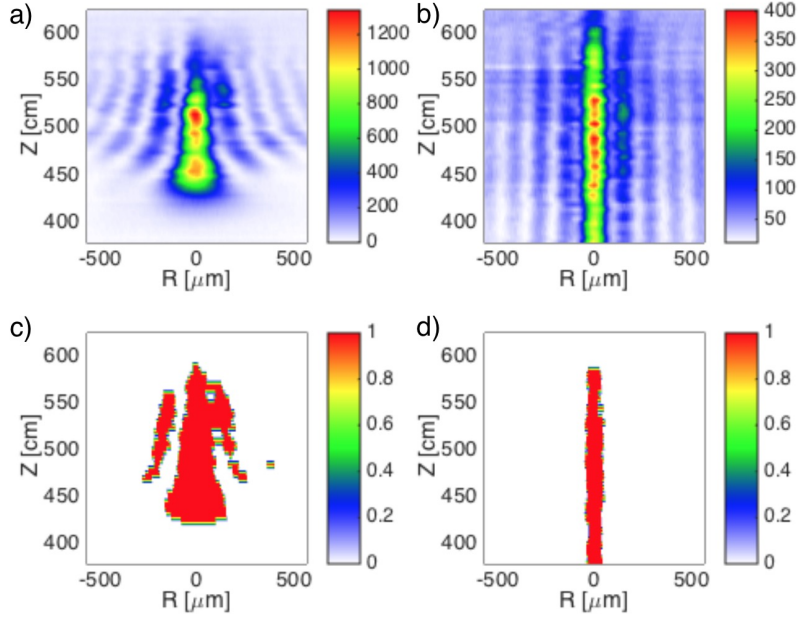
Figure 5.3: Comparison of performance of axilens and axicon both in simulation and testing experiment. Subplot a) and b) are simulation results of axilens and axicon respectively. Subplot c) and d) are experiment profile of axilens and axicon.

5.3 Witness beam diagnostics

In our laser injection ionization scheme, our goal is to produce ultra-low (10^{-8} mrad) emittance beam. As a proof-of-concept, we designed our experiment so that the bunch charge is less than 100 pC. However, as mentioned above, the driver bunch charge is about 3 nC. It is challenging to detect such low charge beam against massive background. Adli *et al* proposed a novel beam profile monitor to construct beam shape based on Cherenkov radiation emitted from a charged particle beam in an air gap [AGC15]. The profile monitor is a set of silicon wafers used to reflect Cherenkov light to CCD camera. From the radiation, we can estimate beam size. The photon yield (pixel counting on camera) tells us beam charge given the good linear relation between these two after we calibrate camera. The calibration of charge is shown in Figure 5.4. When the design orbit energy is set to far away from driver bunch energy 20.35 GeV, the beam is dispersed less which can cause saturation when the charge is high. Thus to spread beam sufficiently, it is better to set the orbit to FACET beam energy.

Combined with this beam profile monitor, we are able to measure charge and energy of
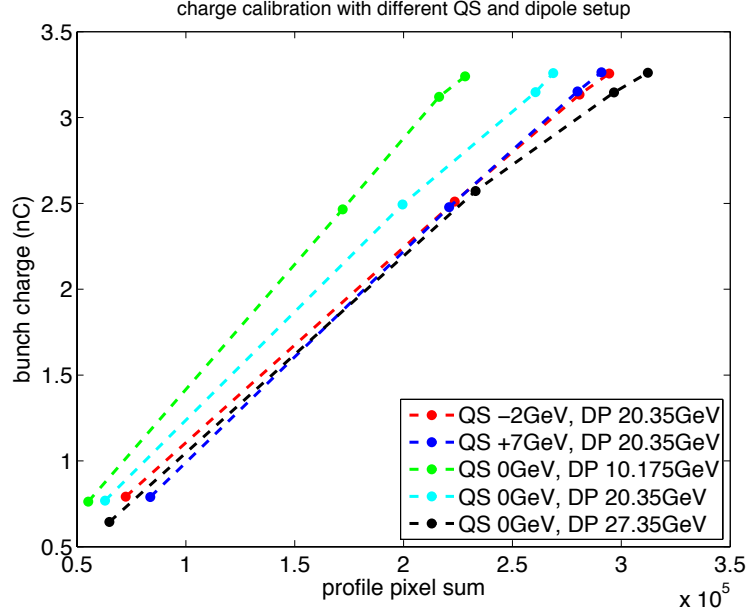
Figure 5.4: Calibration between pixel counting and charge in different dipole design bending orbits and different quadrupole focusing energy.

witness bunch with bending magnet and focusing quadrupoles. The imaging spectrometer is composed of a quadrupole doublet and vertical bend magnet downstream of FACET IP area. The quadrupoles are tuned to image the beam waist which is at the starting point of plasma column to a phosphorescent (LANEX) which is located at 9.6 m downstream of the dipole magnets. In Figure **??**, quadrupole is configured to image at different energy which allows us to calibrate position on camera to the beam energy.

Figure 5.6 shows the whole picture of E210 experiment setup. The major components in plasma experiment area are one injection box (named "picnic basket") which hosts axilens for line-focusing pre-ionizing laser, two compressors (closed one compresses main
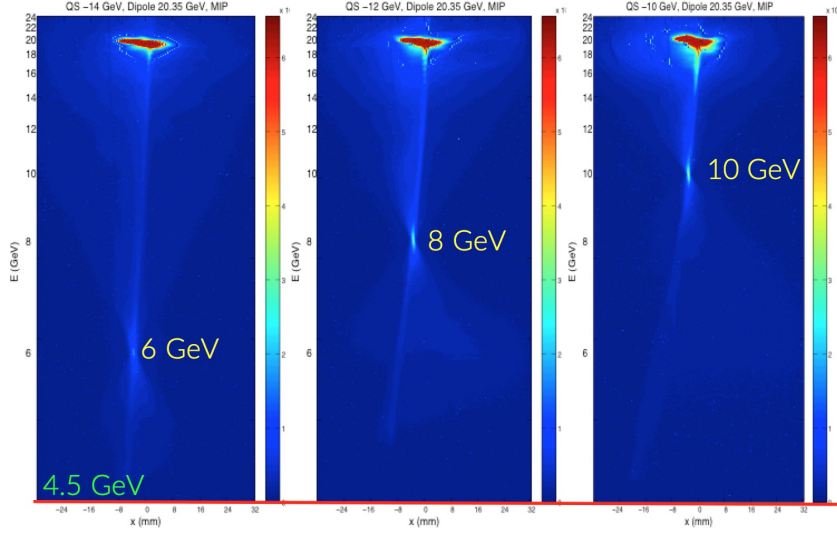
Figure 5.5: Snapshots of beam going through plasma on spectrometer when quadrupole is set to focus at 6 GeV, 8 GeV and 10 GeV respectively. The lowest energy can be observed on camera is 4.5 GeV marked in red solid line.

laser, the open air one compresses probe laser) and five 6-inch cubes at downstream of "picnic basket". After the laser is sent down to the tunnel, a small fraction is split on the path mostly for probing in different experiments and also for injection laser in our experiment. As we mentioned above, the laser goes through main compressor. The grating is motorized so that we can obtain different pulse duration by tuning the grating degree. After the compressor, there is an axilens to line-focus the laser followed by a delay stage to tune position where the plasma starts. Rail_far camera is a far field camera for monitoring the laser alignment. The motorized 45° gold mirror reflects line-focused laser into downstream cubes along the beam line. The setup is adjusted so that plasma generation is optimized (plasma column width is maximized.) in cube 3 where we plan to do the experiment.

For electron beam and laser pulse synchronization and timing jitter measurement, we set up two Electro-Optic Sampling (EOS) systems as we will dive into details of EOS in next section. One EOS is set up in "picnic basket" while 90°-injection happens in Cube 3 for the reason that line-focused laser generates optimal plasma there. However, the fact that two locations are two meters away from each other makes it difficult to synchronize probe and injection beam. To solve this problem, we split injection laser further and set up another EOS in next cube downstream. Two EOS setups are called "upstream EOS"

and "downstream EOS" respectively. That path length difference between injection laser and downstream EOS probe beam is offset to a few picoseconds. Therefore, upstream EOS is for recording timing jitter in realtime while downstream EOS is to help synchronize injection laser and electron bunch.

The Ti:Sa laser pulse delivered down to tunnel is about 300 mJ in total, 90% portion acting as "main laser" is compressed to 50 fs and line-focused to ionize H_2 gas. The rest 10% serves as probes for multiple plasma experiments and also injection laser for our experiement. The probe portion is distributed further as follows: 300 μJ is taken for upstream EOS probing; The rest is sent down for our injection in Cube 3 ($\sim$89%), downstream EOS in Cube 4 ($\sim$4%) and other experiments ($\sim$10%).

As shown in Figure 5.6, the first EOS setup resides in "picnic basket" where main laser is line-focused with axilens and injected to pre-ionize H_2. Two EO crystals (1 cm $\times$ 1 cm $\times$ 100 μm GaP and 1 cm $\times$ 1 cm $\times$ 500 μm ZnTe) are mounted on a holder that can slide horizontally. Both of them are (110) cut. Additionally, we mounted a 20 μm thick YAG crystal to mark electron beam position on camera prior to EOS scan. The sliding motor allows us to switch difference crystals and also control the distance from crystal edge to electron beam line. The typical distance is 3-5 mm. Crystals are aligned perpendicular to beam line and probe laser passes through the crystal with an angle of 45° as mentioned above. Half-wave plate is aligned on laser path to adjust probe's polarization and polarizer and analyzer are cross-polarized to minimize extinction ratio.
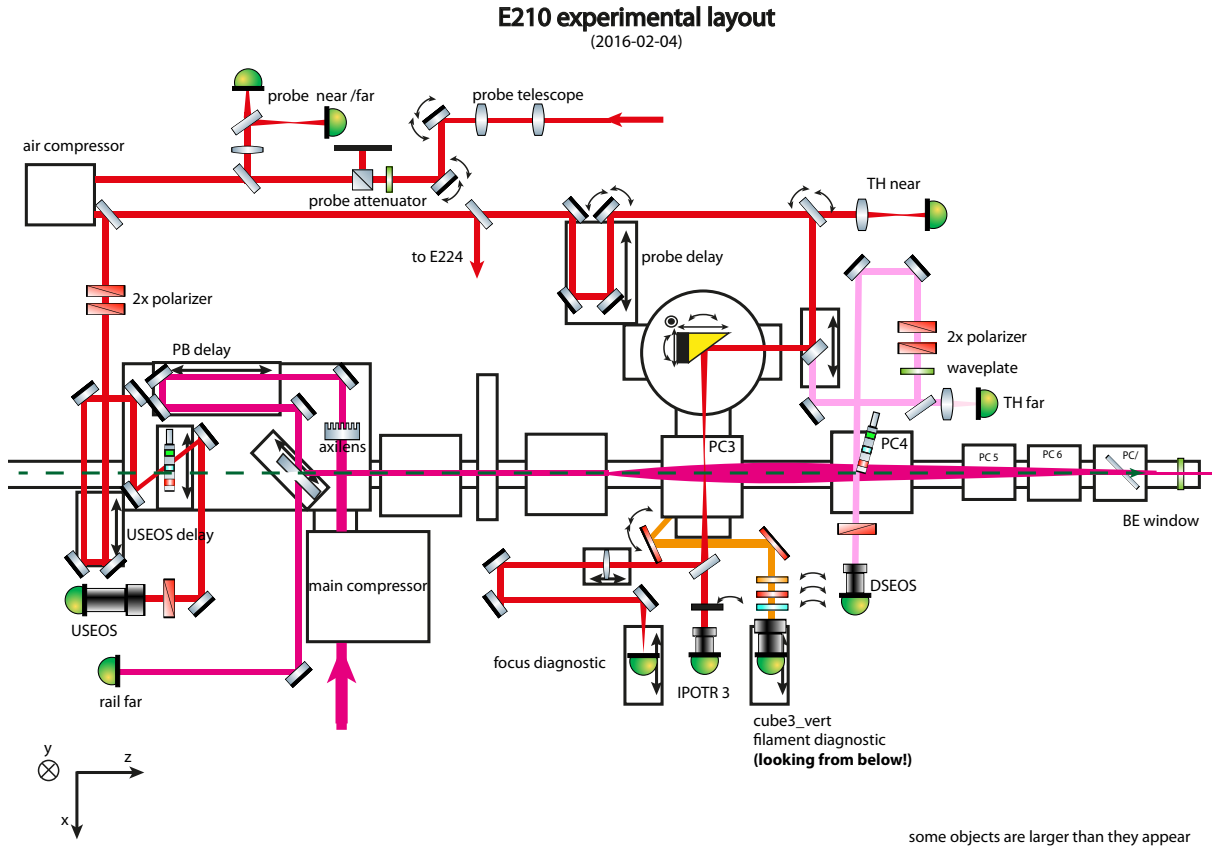
Figure 5.6: Schematic layout of components in FACET experiment area. Only optics that are related to E210 experiments are displayed.

5.4 Dark current

Originally, "dark current" refers to trapping of electrons released on the metal surface in tradition particle accelerator when pursuing higher acceleration gradients. In plasma wakefield accelerator experiments, the gradients are tens of GeV/m. In this highly non-linear regime, strong plasma wakes can create large electric field spikes or "hot spots" leading to further ionization and trapping of plasma species at unfavorable phases. The uncontrolled self-injection of these electrons degrade the blowout regime quality and compromise the wakefields via beam loading. The theory has been studies based on single particle model in [SES06]. The fraction of trapped plasma electrons were estimated and trapping threshold were discussed. In experiment, collaboration of USC, UCLA and SLAC observed the phenomenon and determined the trapping threshold at FFTB [E 05].

A robust, steady acceleration process prefers constant longitudinal accelerating field over the acceleration length. Especially for our laser-ionization injection scheme, dark current also increases background noise and make it difficult to detect low-charge witness bunch. To achieve high quality beam, we have to optimize electron driver bunch and plasma conditions (i.e. gas density, mixing ratio of H_2 and He) to minimize dark current in our experiment and create a clean and robust blowout regime.

Two major hot spots are identified and shown in Figure 5.7. The first hot spot in a) is located at the vertex of the bubble where re-attracted plasma electrons coalesce. The fields in that area can be large enough to tunnel-ionize previously nonionized gas species or the ion background, thus releasing additional electrons. If wakefield is strong enough, these electrons could be trapped and form dark current; The second hot spot can be generated by electric fields of the driver bunch because in blowout regime, bunch density is larger than plasma density $n_b > n_p$. Furthermore, the driver bunch can be subject to plasma lensing and betatron oscillation along the propagation in plasma. These effects can pinch the beam transversally and the increased electric field can ionize He near the front of the plasma wave as in b).
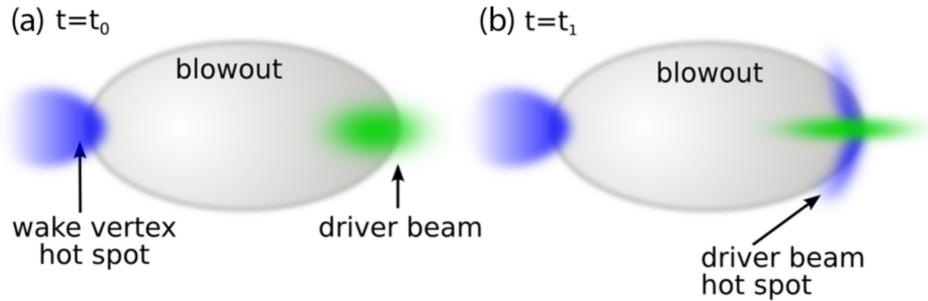
Figure 5.7: Two snapshots of plasma blowout regime at t_0 and t_1 (t_0 ¡ t_1) to display sources of huge electric field spikes or hot spots (blue shade) in PWFA. (a) Wakefields locally maximize at the tail of blowout regime and can trap plasma electrons. (b) The one concurrent with the driver bunch which is subject to plasma lensing and betatron oscillations.

We consider three scenarios here: Self-field ionized plasma, partial laser pre-ionization and complete laser pre-ionization. With VSim 3D particle-in-cell simulations, we modeled the problem based on FACET beam and laser conditions. The electron bunch can

be compressed down to tens of femtoseconds and current up to 30 kA. Laser can be compressed to 70 fs. The plasma gas is the mixture of low ionization threshold (LIT) H_2 and high ionization threshold (HIT) He with tunable mixing ratio.

Given FACET beam, self-field ionization of H_2 only occurs at the proximity of the bunch density peak. As seen in Figure 5.8 (a), a substantial part of the driver cannot contribute to the plasma wake excitation because of partial plasma generation. The ionization front depends on the ionization potential of the plasma media and the driver beam emittance. The shift of the ionization front with respect to the driver bunch is known as "head erosion" [BR94, BCD10]. The reduction of the effective current has further consequences: the effective bunch length $\sigma_{z,eff}$ is shorter than the nominal bunch length σ_z and the effective bunch profile has a sharp rising edge. Neither of them are optimal setup for driving a stable plasma wake and the trapping performance is poor. The released He electrons eventually slip out the accelerating phase and are lost in the plasma background.

The partial laser pre-ionization technique was inspired from [AZV13] to mitigate head erosion by generating a narrow plasma filament in front of the driver bunch by an auxiliary laser pulse. The normal vector potential a_0 and spot size w_0 are chosen as 0.016 and $20\mu m$ to avoid ionizing He. This create an extended plasma region in Figure 5.8 (b). However, partial pre-ionization with such an auxiliary laser pulse does not reinforce the blowout, but weakens it. The reason is that only on-axis H_2 were pre-ionized by laser instead of the whole blowout regime. The electrons expelled from axis are not properly re-attracted. These "shoot-away" electrons prevent a proper strong blowout to be formed, let alone the trapping. Therefore, the pre-ionization needs to be extended to the whole blowout regime. This can be done by increasing the spot size w_0.

With larger spot size laser, we can pre-ionize H_2 completely. The robust blowout is formed in Figure 5.8 (c). The superposition of peak electric field and laser field is about 120 GV/m according to the color bar which is sufficiently large to ionize He. The large trapping potential and accelerating field results in massive amount of He electrons trapped.

In principle, lower plasma density corresponds to less dark current, since the wakefield roughly scales as $\sqrt{n_0}$ [Lot04]. We tuned down the plasma density step by step and fields

(a) $n_H = 3 \times 10^{17}$ cm^{-3}, λ_p= 60 μm   (b) $n_H = 1.5 \times 10^{17}$ cm^{-3}, λ_p= 86 μm   (c) $n_H = 1.5 \times 10^{17}$ cm^{-3}, λ_p= 86 μm
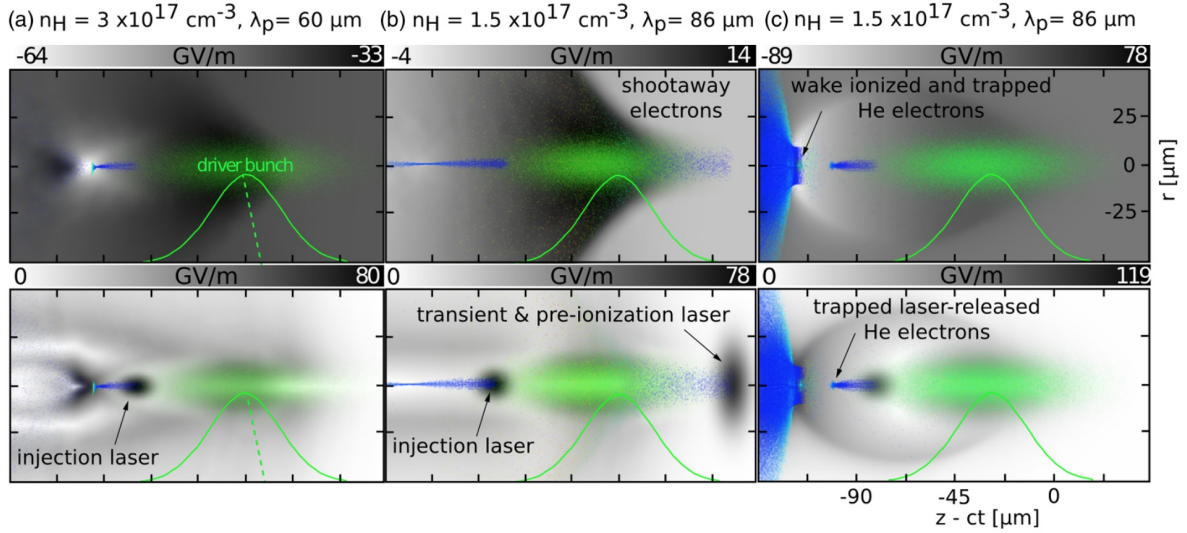
Figure 5.8: Three plasma generation cases: (a) self-field ionization (left), (b) partial pre-ionization (middle), (c) complete pre-ionization (right). The top row of snapshots plots the strength of longitudinal electric field while the bottom row shows the total electric field. The longitudinal current profile of the driver bunch (green) is given with the green line-out. The green dashed line in (a) indicates the effective current profile. The released He electrons are shown in blue shadow.

and potential snapshots of two steps are illustrated in Figure 5.9 (a) and (b). The effective trapping potential $\Phi = (\Psi_{max} - \Psi)/((m_0 c^2/e)(1 - \gamma_{ph}^{-1}))$ for each scenario is calculated and shown at the bottom of each panel. Here, Ψ is the electrostatic wake potential and γ_{ph} is the Lorentz factor associated with the wake phase velocity. The volume where the potential exceeds the trapping threshold ($\Phi < -1$) is indicated with the red solid line. From Figure 5.9 (a) to (b), plasma density is reduced by a factor of 5. However, in both cases, the driver beam hot spot releases He electrons in trapping region. To eliminate the driver beam hot spot, the bunch density is reduced by increasing σ_z from 25 μm to 40 μm as in Figure 5.9 (c). Plasma lensing is still present, but electric field of driver bunch is not strong enough to ionize He. Further lowering the plasma density to $5 \times 10^{15} cm^{-3}$ as in Figure 5.9 (d) which shows a dark-current-free blowout regime. Therefore, simulations demonstrate that decreasing plasma density and reducing driver bunch peak current can mitigate dark current while maintaining high quality blowout regime.

Previous discussion have shown that longer plasma wavelength helps to mitigate the
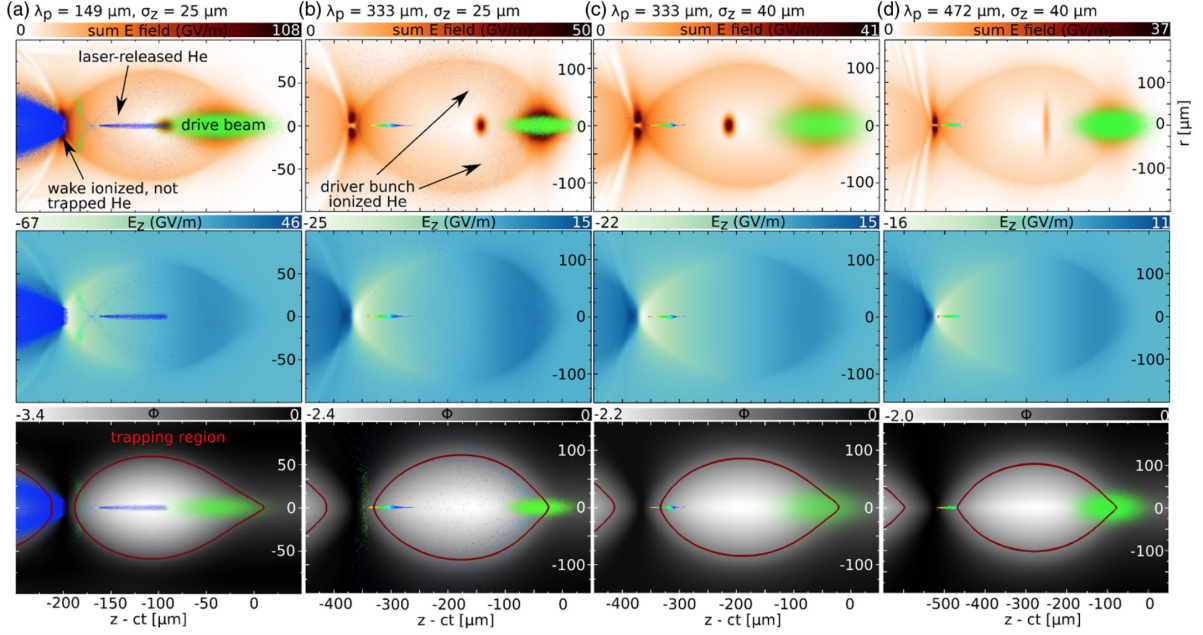
Figure 5.9: Simulation results of dark current reduction in laser injection PWFA. Snapshots in the top row show the electric field while those in the middle row show the longitudinal wakefield and bottom row show the potential Φ. All snapshots are taken at the onset of the laser release. The green shadow is the driver beam. The trapped He electrons are color-code (red is high energy end, blue is low energy end). The red solid ellipse is the estimated trapping region.

source of dark current. However this leads to significant technical challenge because the elevated blowout sizes demand sufficiently wide pre-ionized plasma columns. To make full use of FACET laser energy and expand the plasma column width, as we have discussed in early section, optics such as axicon or axilens is used. Another way to eliminate dark current is to reduce the driver bunch charge. In simulation, we found that when plasma density is $1.1 \times 10^{17} cm^{-3}$ (plasma wavelength $\lambda_p \approx 100 \mu m$), this would be a typical density for our experiment, after we reduced driver bunch charge down to 1.1 nC with a notch collimator, the blowout regime is clean without dark current. In Figure 5.10, laser was injected after driver bunch experienced plasma lensing and betatron oscillation. The witness bunch already has been accelerated to 570 MeV. The witness bunch has been produced and accelerated in a strictly dark current free environment. Here, dark current is ruled out by the complete absence of He-ionizing electric field strengths outside the

injector laser position in the blowout.
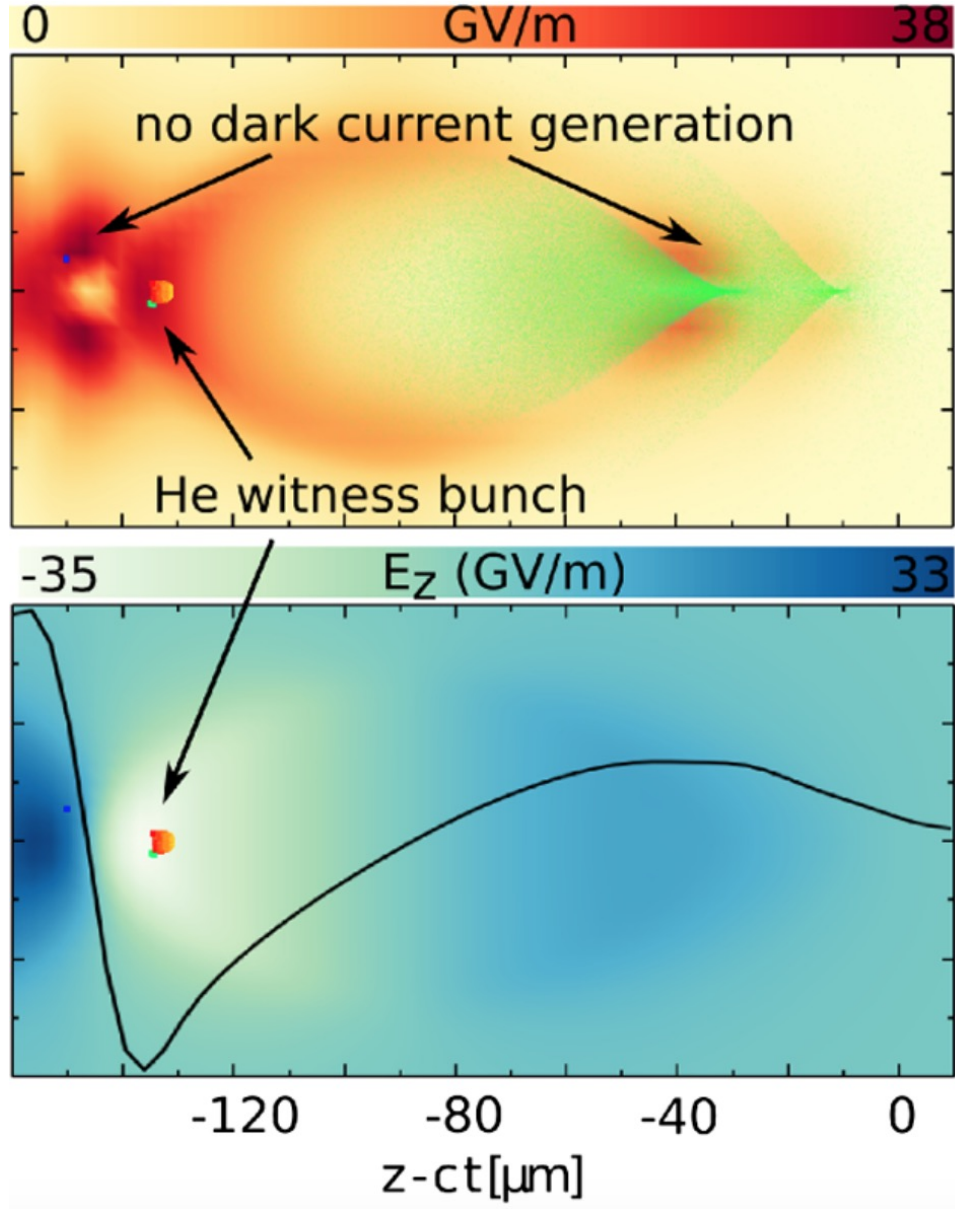
Figure 5.10: The top snapshot is plot of total electric field while the bottom one is only longitudinal component. On-axis lineout of the field is overlaid on the snapshot in black solid line.

As we mentioned earlier, we can reduce the dark current by either lowering the plasma medium pressure/density or reducing the driver bunch charge. In experiment, we let FACET e-beam travel through the plasma medium and observe the increase of charge both on torroids and on spectrometer screen. We reduced driver bunch charge by inserting a notch collimator so that it partially blocked the beam. In that way, we reduced the bunch charge to 2 nC and 1.5 nC and observed significant charge decrease which is trapped

charge or dark current as in Figure 5.11. To study the relation between plasma medium density and trapped charge, we also tuned down the gas pressure and dark current went down till trivial level.
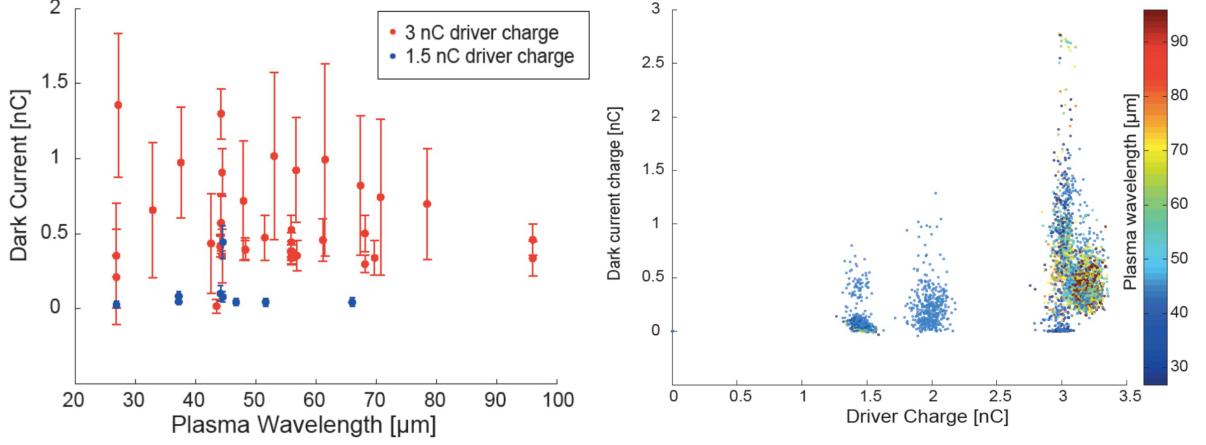
Figure 5.11: The left plot shows the comparison of averaged dark current over different gas densities in 3 nC driver (red) and 1.5 nC driver (blue) cases. The right plot shows shots scattering of 1.5 nC, 2 nC, 3 nC three different cases.

5.5 Timing synchronization and jitter

To accelerate electrons in this laser ionization injection scheme successfully and obtain ultra-low emittance witness beam, we should choose optimal plasma density and gas mixing ratio (H_2:He) based on FACET beam conditions. The trapping condition of ionization injection has been simulated and proved in experiment both in beam-driven scheme [ODK07] and in laser-driven scheme [PMM10]. Another factor is background charge (called "dark current"). According to last section, in excessively dense plasma environment, "dark current" trapped by driven bunch will be significant which impedes the measurements of witness beam. There are also restrictions from practice, for example, plasma column generated by main laser pre-ionization is less than 200 μm wide which limits the transverse size of blowout regime. With all of these considerations, plasma density is chosen on the order of 10^{17} cm^{-3} and the mixing ratio of H_2 and He is 50:50. This plasma density corresponds to 100 μm wavelength which roughly equals to blowout regime longitudinal size. Therefore, if we want to guarantee that ionization laser is

injected inside blowout regime, the laser has to be synchronized with driver bunch at 100 fs level.
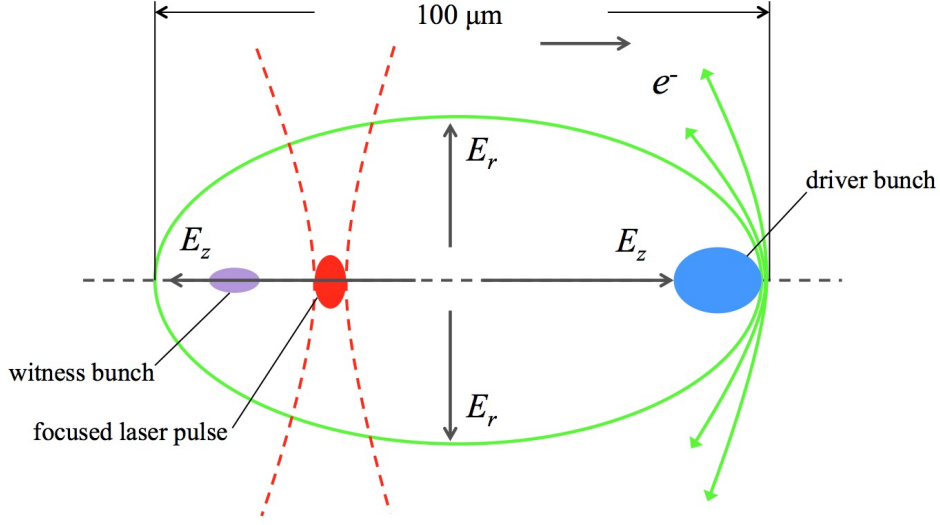
Figure 5.12: Electron driver bunch (blue ellipse) drives wakes while propagating from left to right. Synchronized laser pulse (red ellipse) is injected from side and focused on the axis to ionize He gas and generate witness bunch (purple ellipse). The length of plasma bubble is about 100 μm.

To locate relative time-of-arrival between laser pulse and electron bunch, we observe the enhancement of plasma radiation. When the intense field of an electron bunch or a laser pulse liberates electrons or even drives a wake in neutral gas, there are multiple mechanisms to generate radiations: collision-based absorption and emission, bremsstrahlung radiation, etc. Both mechanisms will be explained in next paragraphs. The radiation intensity increases as field intensity. FACET beam itself can ionize H_2 gas partially. However, if laser pulse overlaps with the electron bunch, the ionization will be enhanced due to the superposition of fields. The radiation enhancement captured by camera indicates the moment t_0.

Collision-induced absorption and emission refers to the inelastic collision process of molecules in a gas. High-energy electrons and photons collide with gas molecules and molecules absorb part of kinetic energy from particle and excite to higher-level energy state. After a while, these plasma electrons fall back to low-level and emit radiation. The most famous emission of H is H-alpha with a wavelength of 656.28 nm while for He, the wavelength of strongest emissions are 447.148 nm and 501.567 nm. During plasma

experiment, we inserted different color filters to select each emission individually.

Bremsstrahlung is a German word that means "braking radiation". It is electromagnetic radiation produced by the deceleration of a charged particle when deflected by another charged particle, typically an electron by an atomic nucleus Figure 5.13. As a high speed electron approaches an atom, it will be repelled by the electrons of the atom. If the electron is slowed down, it will lose kinetic energy and convert that energy to radiation due to conservation of energy. The spectrum of bremsstrahlung is continuous and the shift of peak intensity corresponds to the amount of energy last by electron.
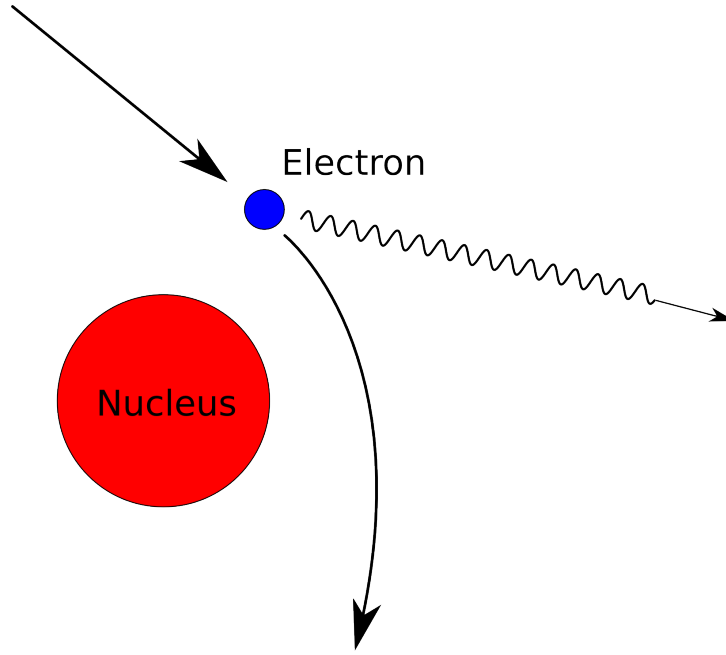
Figure 5.13: Sketch of bremsstrahlung radiation generated by a high-energy electron deflected in the electric field of an atomic nucleus

As shown in Figure 5.14 (a), there is a sharp edge at t_0 and (b), (c) and (d) are example snapshots of plasma radiation from the scan shown in (a). Before t_0, when electron bunch arrives at the cross ahead of laser pulse as illustrated in Figure 5.14 (b), on its right side (closer to laser pulse), ionization is enhanced while left side is not affected obviously. The timing delay is tuned step by step so that laser tends to meet electron beam at the cross. The laser pulse spot is enlightened by local maximum radiation due to the superposition of laser field and electron bunch static field. In fact, after camera calibration, the slope of laser spot trace is estimated as nearly speed of light which agrees with the group velocity of laser pulse in low-density gas. In Figure 5.14 (c), laser pulse

and electron bunch overlap at the cross. Laser pulse assists electron bunch in releasing more electrons on the left of electron bunch path. Once the timing is delayed so that laser bunch passes the cross first as in Figure 5.14 (d), all the gas molecules on the laser path are pre-ionized partially. Electron bunch creates a significantly larger amount of plasma radiations. Laser pre-ionization can last about 1 ns which is approximately the plasma recovery time. Thus in about 1 ns after laser passes, plasma radiation will continue to be enhanced. After $t_2(t_0)$, the electron spot is traced out shown as horizontal dashed gray line in Figure 5.14 (a), because the radiation is enhanced most due to maximum self-field around electron bunch.

For comparison, we repeated the same scan in 8 Torr He gas as shown in Figure 5.15 (a). Since the ionization threshold of He is much higher than H_2, the plasma radiation is not as strong as previous as expected. Only the area around laser focus has constant bright spot. At first when electron bunch arrives at the cross earlier which indicates the e-beam ionizing the gas with little assistance of laser pulse, the self-field of electron bunch can barely ionize gas and generate radiation Figure 5.15 (b). Once the timing delay passes t_0, the ionization due to self-field of electron bunch will be enhanced and we can observe two bright spots on the screen Figure 5.15 (d). One is from laser intense field at focus, the other is from the superposition of laser field and electron bunch self-field.

To locate t_0 more accurately, a fine timing scan was carried out within ± 1 ps window around t_0 with step size of 50 fs. Sigmoid function was applied to fit radiation intensity data points as in Figure 5.16. The turning point in the middle corresponding to the maximum slope is t_0 of our interest. The fitting concludes that t_0 is at 6.432 ps with uncertainty σ of 50 fs.

The discussion above is based on the setup that laser focus is offset from the cross of injection laser and driver bunch by 1 cm. To have the best idea of t_0, we repeated the timing scan in the actual ionization-injection experiment configuration with laser focus overlapping with the cross. The example snapshots are listed in Figure 5.17 panel. First, when H_2 filter is inserted, it means only the radiation with wavelength around 600 nm can go through. Similar to early discussion, the plasma radiation is less intense if e-beam reaches the cross earlier. However, due to Hydrogen's low ionization threshold and focus-cross overlapping, the superposition of laser field and electron bunch field peaks
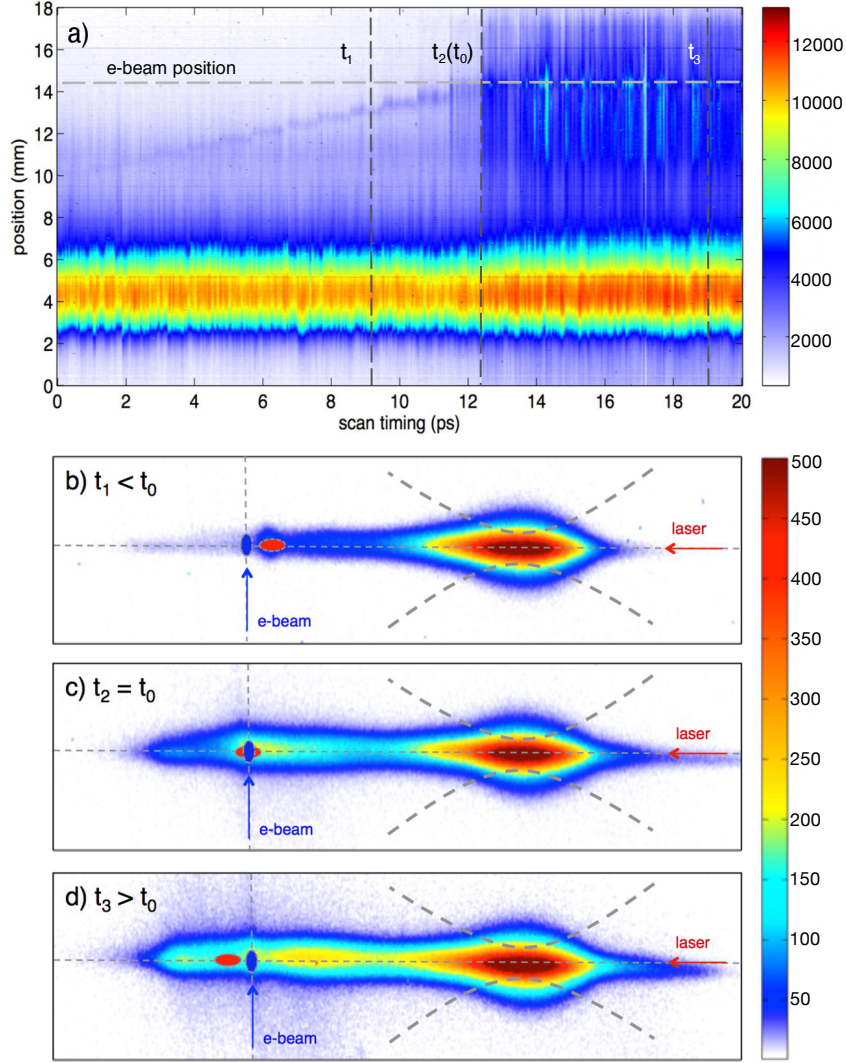
Figure 5.14: (a) displays a timing scan snapshots set with scan range of 20 ps. The step size is 1 ps. 20 shots are taken on each step. Snapshot (b), (c) and (d) are sampled from (a) showing plasma radiation density distribution in pure H_2 gas when $t < t_0$, $t = t_0$ and $t > t_0$ respectively. In each snapshot, the position of laser pulse is marked in red dot when electron bunch (blue dot) is at the same position. Laser focus is indicated by gray dashed curves corresponding to maximum radiation spot.

prominently at t_0, thus ionizing more H_2 molecules and creating more emission. When the filter is switched to He filter, only emission from He atoms (around 400 nm) is allowed to pass. The self-field of driver bunch alone is not intense enough to ionize He and laser field can barely ionize He by itself. However, if laser pre-ionizes He partially, driver bunch can follow up release much more electrons as shown in middle and bottom subplots.
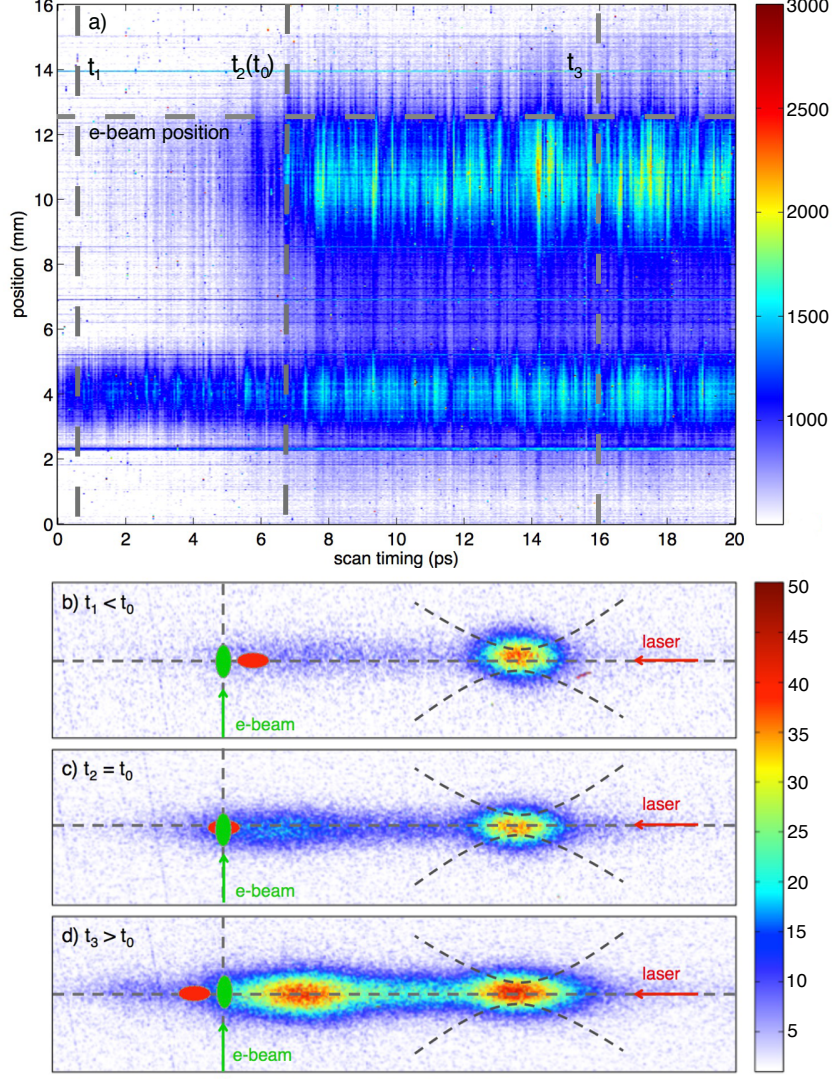
Figure 5.15: The plot is similar to Figure 5.14 except the scan is executed in pure He.

To target t_0 accurately based on scanning dataset, we applied sigmoid fitting to find "turning point" like before for He filter data. t_0 is in [5.415, 5.475] fs range with 95% confidence. For H_2 filter, we select "peak area" and locate the peak with Gaussian fit. The peak is found between 5.227 fs and 5.381 fs with 95% confidence. Given the scanning step is 100 fs, two results are in good agreement.
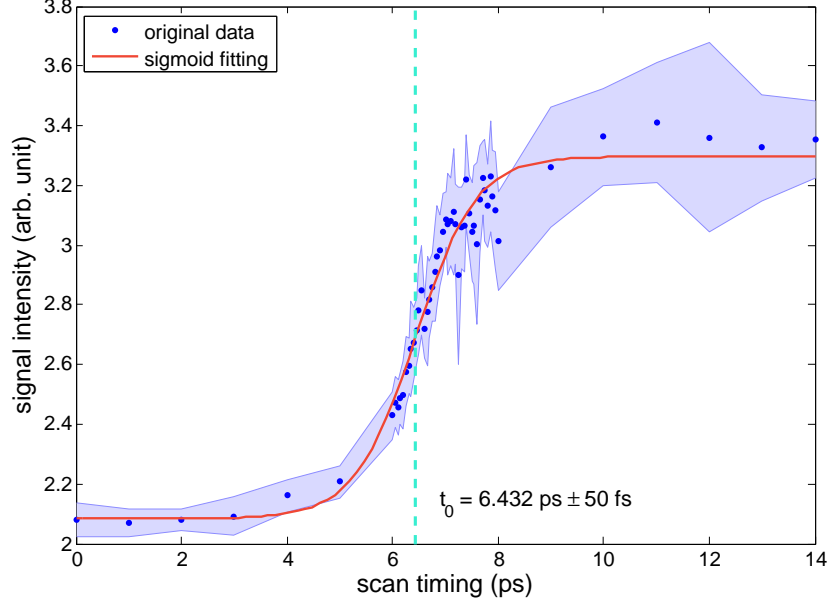
Figure 5.16: Plot of signal intensity flipping region in 14 ps timing scan range (scattering blue points). Coarse scan at two ends is 1 ps per step. Find scan in the middle is 50 fs per step. 20 shots are taken on each step for statistical uncertainty analysis which is reflected in light blue shaded area. Sigmoid fitting is shown in red line.

With laser time-of-arrival relative to electron beam found, we have enough confidence to inject laser pulse at appropriate timing. However, we would like to monitor the timing synchronization and analyze timing jitter in real time when we carry out ionization injection PWFA experiment. Besides, it would be interesting to determine the timing jitter between laser pulse and electron beam during the experiment. In order to achieve that, we use a noninvasive technique, Electro-Optic Sampling (EOS). EOS is an optoelectronic technique which takes advantage of Pockels effect (first described in 1906 by Friedrich Pockels). When electron bunch passes by certain kinds of crystals, the strong electric field exerted on crystal can be regarded as half-cycle THz pulse traveling through the crystal. It will distort refraction index and thus causing birefringence. At that moment, if a linearly polarized laser pulse travels through the crystal. The polarization will be elliptical. We are able to observe "the leak" through polarizer and analyzer. With this method, we can synchronize laser pulse and electron bunch to 100 fs level without a super fast photodetector.

Benefiting from development of ultrafast laser techniques, EOS has been adopted in
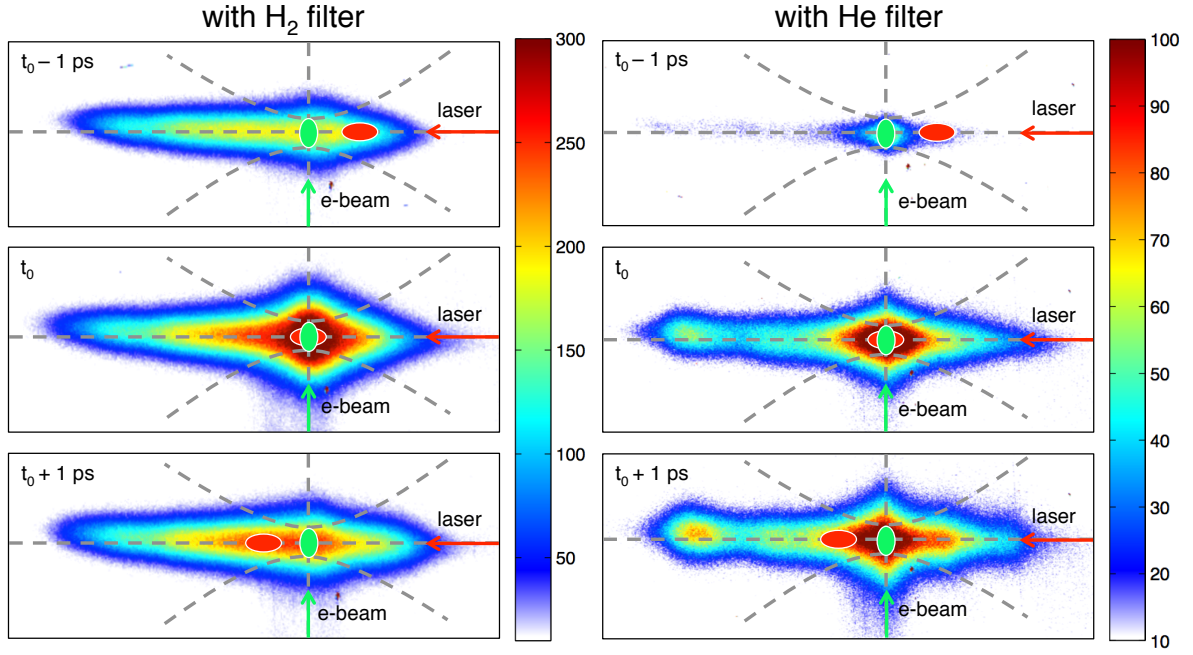
Figure 5.17: The plasma emission snapshots of timing scan with H_2 filter in (left column) and with He filter in (right column). Three shots are sampled in each scan: e-beam arrives at the cross 1 ps earlier than laser; e-beam and laser arrive at the cross simultaneously; e-beam arrives at the cross 1 ps later than laser. Laser focus lined out by gray dashed curve overlaps with the cross of laser and e-beam trajectories (gray dashed straight line). the position of laser is marked as red ellipse with the moment when e-beam (green dot) arrives at the cross as a reference.

many applications such as directly measuring the beam near-field and its longitudinal profile [YMG00, BGJ07], characterizing beam generated radiation like coherent transition radiation [TSF06] and mapping the wakefields trailing the beam [FMC01]. This technique also has application in Free Electron Laser (FEL) field [YMG01, ADR09]. [YMG01] discussed the experiment of characterizing (both amplitude and phase) of freely propagating pulsed electromagnetic radiation and for the quasi-static electric field of relativistic electron bunches. [ADR09] reported the success of EOS in FLASH (free electron laser in Hamburg). It determines the relative arrival time of the extended ultraviolet pulse of FLASH and an amplified Ti:Sa femtosecond-laser pulse at the interaction region better than 90 fs RMS. In UCLA, Scoby *et al* applied EOS time-of-arrival diagnostics in the different context of relativistic ultrafast electron diffraction (UED) where electrons are used
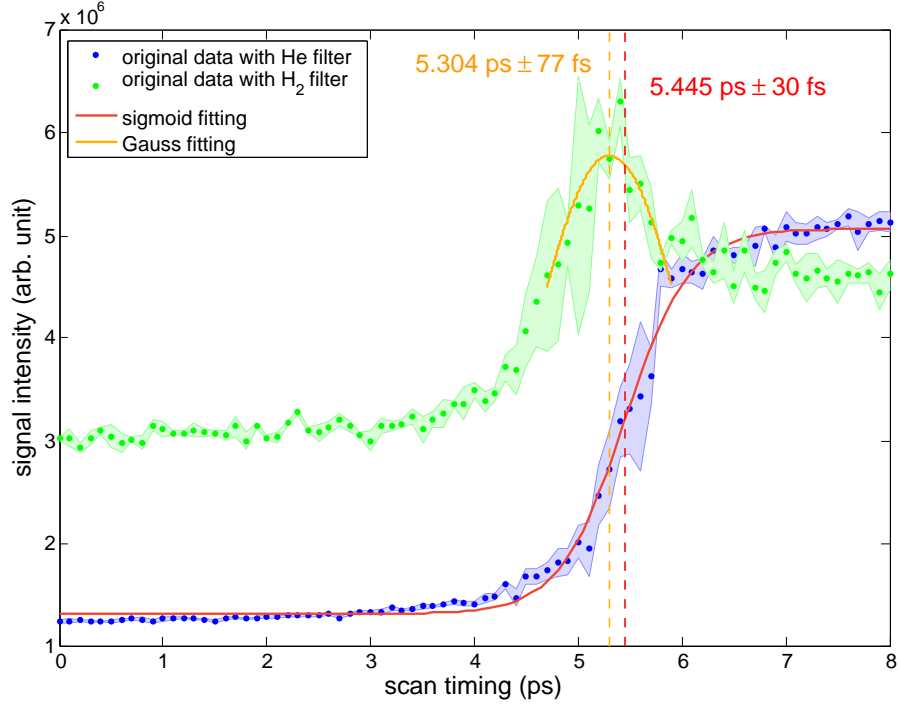
Figure 5.18: Step plot of plasma radiation intensity over timing scan when H_2 filter (blue) and He filter (green) are inserted in turn. Uncertainty is shown in shadow. Sigmoid fitting is applied to data points with He filter in in red solid line. The peak of H_2 filter data is found with Gaussian fit in orange solid line.

directly as probes of atomic structral rearrangements on ultrafast time scales [SMM10].

To have a deeper understanding of EOS mechanism, let us go back to review the response of dielectric materials to electric field. In isotropic media, the relationship between electric displacement field $\mathbf{D}$ and electric field $\mathbf{E}$:

$$\mathbf{D} = \varepsilon_0 \varepsilon \mathbf{E} \tag{5.1}$$

where ε_0 is permittivity of free space and scalar ε is relative dielectric permittivity independent of direction. While in anisotropic media such as a crystal, when $\mathbf{D}$ is not parallel to the electric field, the permittivity is a symmetric tensor $\hat{\varepsilon}$. In this case, Eq.5.1 is expressed as:

$$\begin{pmatrix} D_1 \\ D_2 \\ D_3 \end{pmatrix} = \varepsilon_0 \begin{pmatrix} \varepsilon_1 & 0 & 0 \\ 0 & \varepsilon_2 & 0 \\ 0 & 0 & \varepsilon_3 \end{pmatrix} \cdot \begin{pmatrix} E_1 \\ E_2 \\ E_3 \end{pmatrix} \tag{5.2}$$

The difference among $\varepsilon_i (i = 1, 2, 3)$ results in birefringence. The inverse of $\hat{\varepsilon}^{-1}$ is defined as impermeability tensor.

For crystals like ZnTe and GaP who have cubic crystal lattice, their ε_i are all indentical, which means impermeability tensor can be written as the product of scalar ε^{-1} and unit matrix $\boldsymbol{I}$.

$$\hat{\eta}(\boldsymbol{E}) = \varepsilon^{-1} \boldsymbol{I} + \boldsymbol{r} \cdot \boldsymbol{E} \tag{5.3}$$

where $\boldsymbol{r}$ is EO tensor. Note that to include Pockels effect, linear order term $\boldsymbol{r} \cdot \boldsymbol{E}$ is added and higher order effect such as *Kerr effect* is neglected.

Usually EO crystals like GaP and ZnTe are cut in (110) plane as shown in Fig.. In this plane, *x, y, z-axis* are [-1, 1, 0], [0, 0, 1] and [-1, -1, 0] respectively. To minimize confusion and keep consistency, curve bracket is used to label a plane, while square bracket is for vector. Without losing generality, let us assume there is an angle α between external electric field $\boldsymbol{E}$ and *x-axis* ([-1, 1, 0]) as shown in Fig.5.19(b). If we decompose $\boldsymbol{E}$ into *x, y, z-axis*, we obtain

$$\boldsymbol{E} = E \begin{pmatrix} -\cos\alpha/\sqrt{2} \\ \cos\alpha/\sqrt{2} \\ \sin\alpha \end{pmatrix} \tag{5.4}$$

We already know the permittivity is same in three directions which means $n_{0x} = n_{0y} = n_{0z} = n_0$. Again, due to cubic symmetry of crystal lattice, $r_{41} = r_{52} = r_{63} = r$. According to this paper, the impermeability tensor now can be written as

$$\hat{\boldsymbol{\eta}}(\boldsymbol{E}) = \frac{1}{n_0^2}\begin{pmatrix} 1 & 0 & 0 \\ 0 & 1 & 0 \\ 0 & 0 & 1 \end{pmatrix} + rE\begin{pmatrix} 0 & \sin\alpha & \cos\alpha/\sqrt{2} \\ \sin\alpha & 0 & -\cos\alpha/\sqrt{2} \\ \cos\alpha/\sqrt{2} & -\cos\alpha/\sqrt{2} & 0 \end{pmatrix} \quad (5.5)$$

The eigenvalues of $\hat{\boldsymbol{\eta}}(\boldsymbol{E})$ matrix are

$$\lambda_{1,2} = \frac{1}{n_0^2} - \frac{rE}{2}(\sin\alpha \pm \sqrt{1+3\cos^2\alpha})$$
$$\lambda_3 = \frac{1}{n_0^2} + rE\sin\alpha$$

$$(5.6)$$

The respective eigenvectors are

$$\boldsymbol{u_1} = \frac{1}{2}\sqrt{1 + \frac{\sin\alpha}{\sqrt{1+3\cos^2\alpha}}}\begin{pmatrix} -1 \\ 1 \\ \frac{2\sqrt{2}\cos\alpha}{\sqrt{1+3\cos^2\alpha}+\sin\alpha} \end{pmatrix}$$

$$\boldsymbol{u_2} = \frac{1}{2}\sqrt{1 - \frac{\sin\alpha}{\sqrt{1+3\cos^2\alpha}}}\begin{pmatrix} 1 \\ -1 \\ \frac{2\sqrt{2}\cos\alpha}{\sqrt{1+3\cos^2\alpha}-\sin\alpha} \end{pmatrix} \quad (5.7)$$

$$\boldsymbol{u_3} = \frac{1}{\sqrt{2}}\begin{pmatrix} -1 \\ -1 \\ 0 \end{pmatrix}$$

With $n_i = 1/\sqrt{\lambda_i}$ and assumption of $rE \ll 1/n_0^2$, we obtain refractive indices in three directions:

$$n_1 = n_0 + \frac{n_0^3 rE}{4}(\sin\alpha + \sqrt{1+3\cos^2\alpha})$$
$$n_2 = n_0 + \frac{n_0^3 rE}{4}(\sin\alpha + \sqrt{1-3\cos^2\alpha})$$
$$n_3 = n_0 - \frac{n_0^3 rE}{2}\sin\alpha$$

$$(5.8)$$
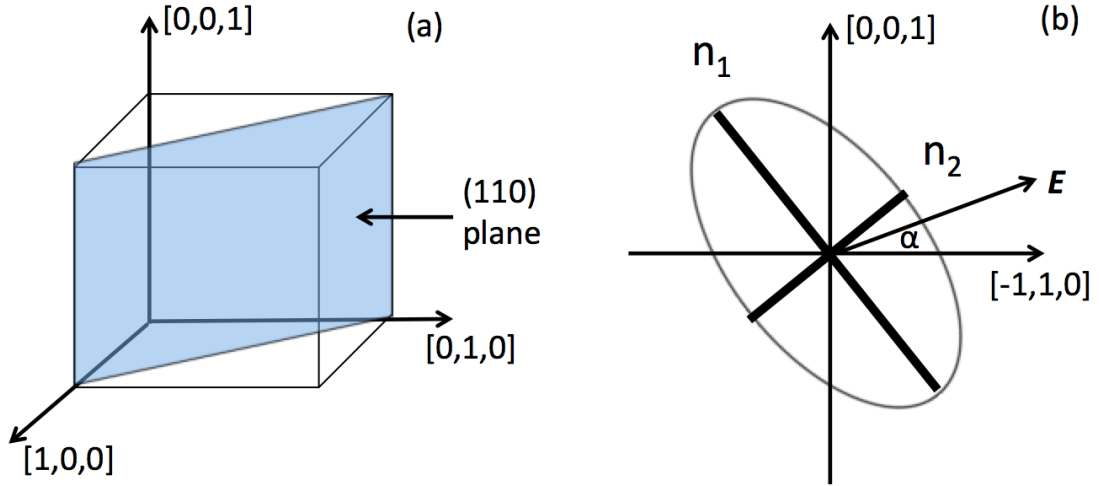
Figure 5.19: a) shows the cut plane (110) of EO crystal. b) Principal-axis transformation in (110) plane. Two axes labeled n_1 and n_2 corresponds to $\boldsymbol{u_1}$ and $\boldsymbol{u_2}$. $\boldsymbol{u_3}$ is normal to (110) plane. Electric field $\boldsymbol{E}$ has an angle α with $x\text{-}axis$ ([-1,1,0]).

After we find refractive indices in three axes, we are able to calculate phase shift Γ caused by birefringence.

$$\Gamma = \frac{2\pi(n_1 - n_2)d}{\lambda_0} = \frac{\pi n_0^3 d}{\lambda_0} rE\sqrt{1 + 3\cos^2\alpha} \tag{5.9}$$

where d is thickness of crystal, λ_0 is wavelength of probe laser.

As an example, now let us calculate the phase shift in our experiment, according to our layout, electric field from electron bunch is vertical which means $\alpha = 90°$. FACET laser is 800 nm Ti:Sa laser. For this wavelength laser, the refractive index of GaP and ZnTe is about 3.16 and 2.82 respectively. The thickness of crystal usually used in experiment is $100\mu m$. FACET ebeam is 20.35 GeV ($\gamma \approx 40000$) and 3.2 nC. Given such large γ, the electric field of ebeam is squeezed to a "pancake" shape with a transverse opening angle of $1/\gamma$. The condition $r_d/\gamma \ll \sigma_z$ is satisfied since in our setup the distance from EO crystal to ebeam r_d is between 1 mm to 10 mm, thus the longitudinal profile of ebeam is well represented by THz signal width which gives us chance to measure bunch length with EOS. Both the transverse RMS σ_r and longitudinal RMS σ_z are about $30\mu m$. Note that $\sigma_z = 30\mu m$ corresponds with frequency 5 THz pulse. The temporal profile of electric

field of ebeam is

$$E(t) = E_0 exp(-\frac{t^2}{2\sigma_z^2}) \tag{5.10}$$

where amplitude E_0 is

$$E_0 = \frac{Q}{(2\pi)^{3/2}\varepsilon_0 r_b \sigma_z} \tag{5.11}$$

where Q is bunch charge. ε_0 is permittivity of free space. r_b is beam radius. Note that the absence of Lorentz factor γ is due to canceling out of lengthening of σ_z when we boost into beam frame and the factor $1/\gamma$ of electric field when we boost back to lab frame. Following Eq.(24) in paper, the dependence of $|r|$ on frequency f is plotted as Fig.5.20. To avoid drastic change of r around 5 THz region, GaP is better than ZnTe for $30\mu m$ long bunch. However, the magnitude of EO coefficient of ZnTe is generally larger than GaP (about eight time larger below 5 THz). Both kinds of crystals were tested in our experiment.
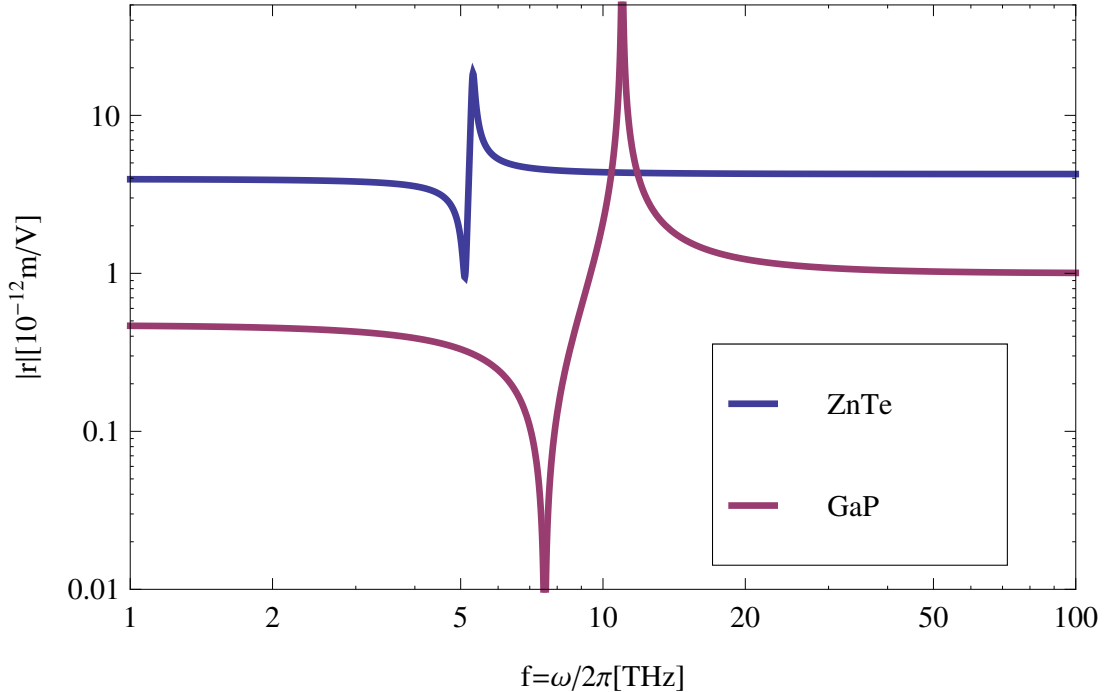
Figure 5.20: Absolute magnitude of EO coefficient $r(\omega)$ of GaP (red) and ZnTe (blue).

73

At the end of this section, I would like to discuss the effect of crystal thickness on EO signal. Due to the difference of THz signal phase velocity and probe laser optical group velocity, in certain range, crystal thickness determines how long THz signal and probe laser propagate in timing. *Geometric response function* is defined to quantitatively measure the the velocity mismatch. In this [paper], $G(\omega)$ is derived assuming laser and electron bunch co-propagate. Here we take the more general form by assuming the angle between laser and electron beam line is θ.

$$G(\omega) = \frac{1}{d} \int_0^d exp(\frac{i\omega z}{v_{ph}(\omega)} - \frac{i\omega z}{v_g \cos\theta})e^{-\alpha z}\mathrm{d}z \tag{5.12}$$

where d is crystal thickness, $v_{ph}(\omega) = c/n(\omega)$ where $n(\omega)$ is the real part of the refractive index, v_g is optical group velocity of laser pulse, $\alpha = \omega\kappa(\omega)/c$ is attenuation coefficient where $\kappa(\omega)$ is the imaginary part of refractive index.
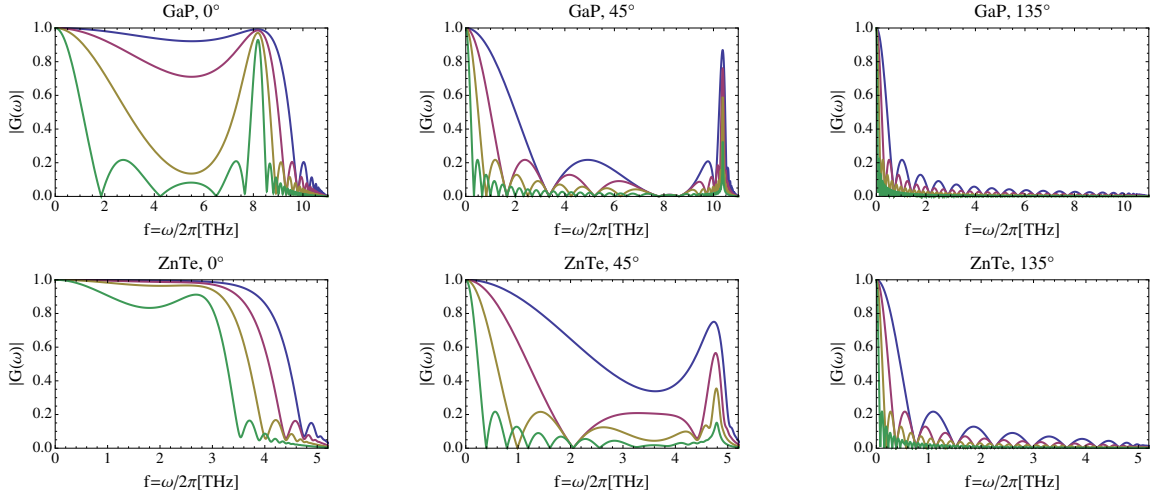
Figure 5.21: Geometric response functions of GaP and ZnTe crystals. 0°, 45°, 135° are angles between laser and electron beam line. Different thicknesses 50 μ m, 100 μm, 200 μm, 500 μm are color coded in blue, red, yellow and green respectively.

As shown in Fig.5.21, to obtain larger response function amplitude, co-propagating scheme is preferred than counter-propagating. We should keep this in mind when we design experiment layout. In given setup, thinner crystal outperforms thicker one. As mentioned earlier, FACET beam equivalents to 5 THz signal. $|G(\omega)|$ is very sensitive in that region which potentially makes signal observation more difficult. Practically, we

converted THz frequency to corresponding bunch length based on the valid assumption that electron bunch passing by crystal can be regarded as a half-cycle THz signal traveling through crystal. 45° orientation is considered in this conversion. Also, FACET beam bunch length range is marked in Figure 5.22.
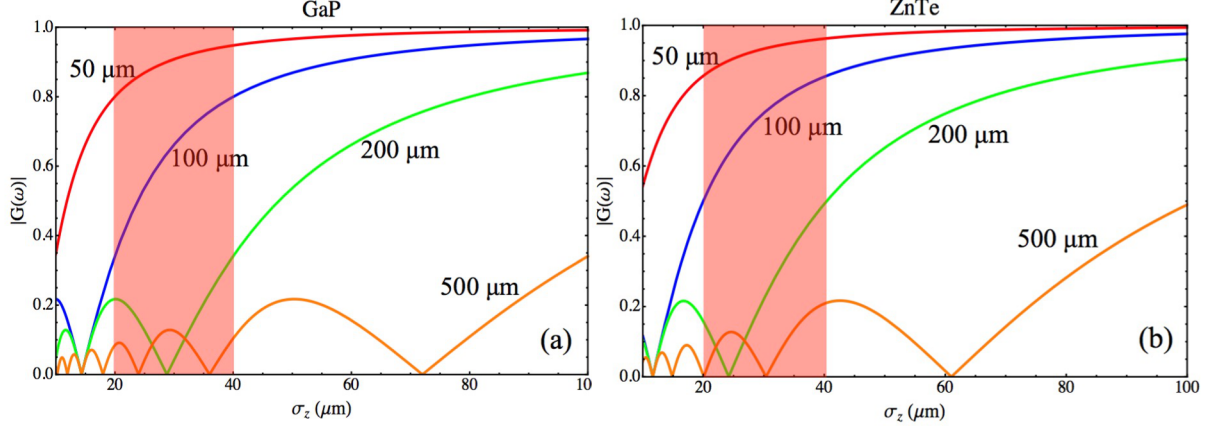
Figure 5.22: Magnitude of geometric response function varies over electron bunch length for different thickness of crystals (50 μm, 100 μm, 200 μm, 500 μm). Figure (a) is GaP. Figure (b) is ZnTe. The pink rectangle marks operating bunch length range in our experiment.

The scan window is width of crystal (1 cm) at 45° orientation which is about 20 ps. We scanned the timing delay in that window at step size of 1 ps. To determine the relative timing jitter between laser pulse and electron beam, we set the delay where the EO signal is the most prominent and sampled about 1500 shots to evaluate timing jitter statistically as in Figure 5.24. The timing jitter is contained in the jitter of horizontal centroid of each EO signal. After Gaussian fit, we obtained the jitter as 190 fs. However, this jitter also includes pointing jitter of both electron bunch and laser bunch. While jitter of electron bunch is trivial, that of laser pulse is obtained as 50 fs from background DAQ with electron beam off. Thus, the relative timing jitter is about $\sqrt{\sigma_{total}^2 - \sigma_{pointing}^2} \approx 160$ fs. LINAC phase ramp is a parameter to tune the compression of electron bunch, thus adjust bunch length as required. Scanning this parameter could affect timing delay of electron bunch. An X-band transverse deflecting cavity (TCAV) is installed at upstream of experiment area to measure longitudinal profile of bunch. The operation of TCAV may also influence bunch delay. Now we have an opportunity of study these effects thanks to

EOS. Figure 5.25 shows the linear calibration between phase ramp and timing delay with a slope of 1 ps/degree roughly. The effect of TCAV operation is trivial under observation with EOS timing resolution.
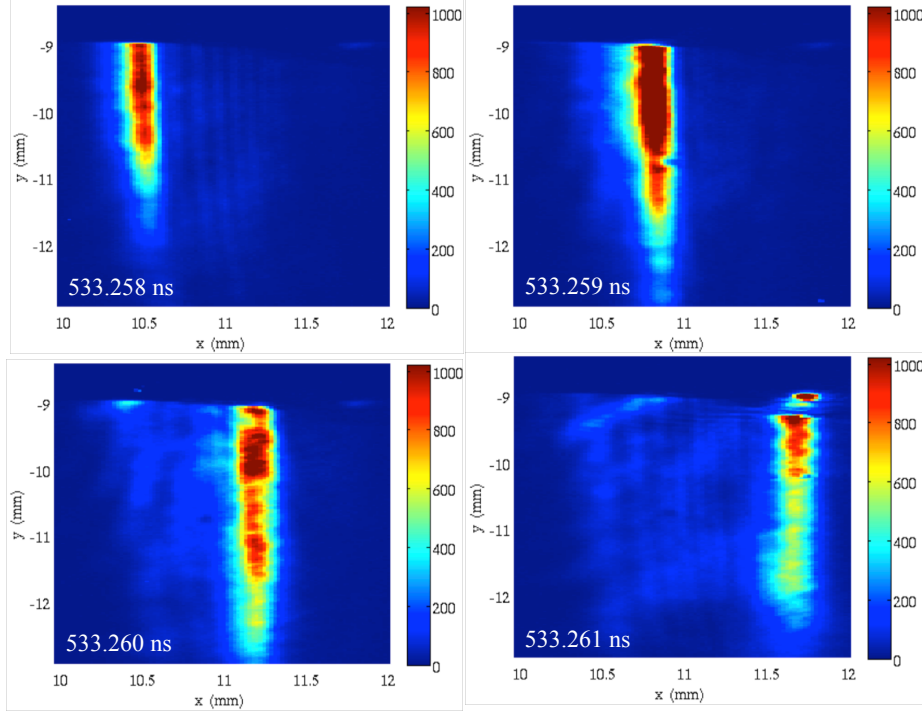
Figure 5.23: Snapshots of EOS scan at step of 1ps. Signal moves from left to right as timing delay increases.

LINAC phase ramp is a parameter to tune the compression of electron bunch, thus adjust bunch length as required. Scanning this parameter could affect timing delay of electron bunch. An X-band transverse deflecting cavity (TCAV) is installed at upstream of experiment area to measure longitudinal profile of bunch. The operation of TCAV may also influence bunch delay. Now we have an opportunity of study these effects thanks to EOS. Figure 5.25 shows the linear calibration between phase ramp and timing delay with a slope of 1 ps/degree roughly. The effect of TCAV operation is trivial under observation with EOS timing resolution.
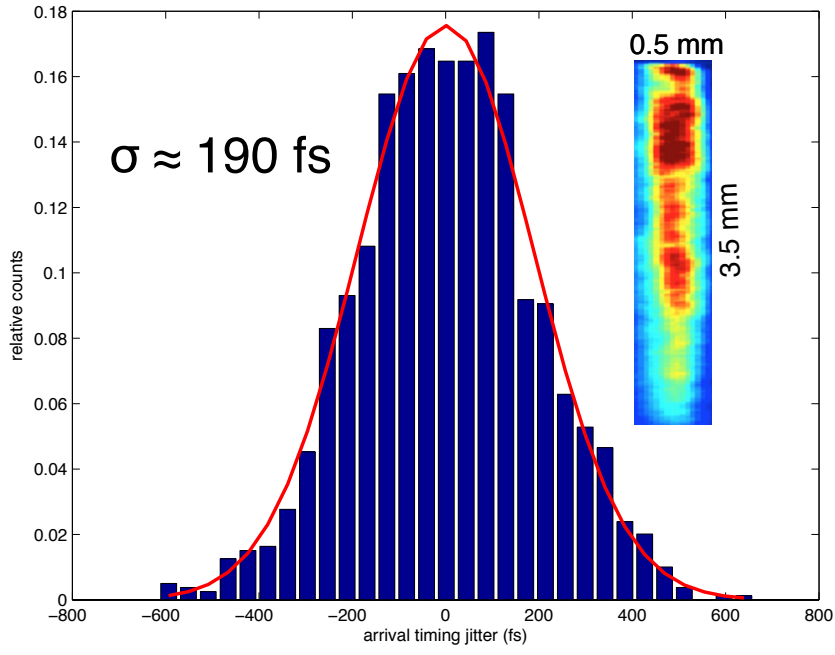
Figure 5.24: Histogram of centered and normalized jitter (blue). Gaussian fit is applied in red solid line. The timing jitter uncertainty is about 190 fs. The inset image is EO signal with dimension labeled.
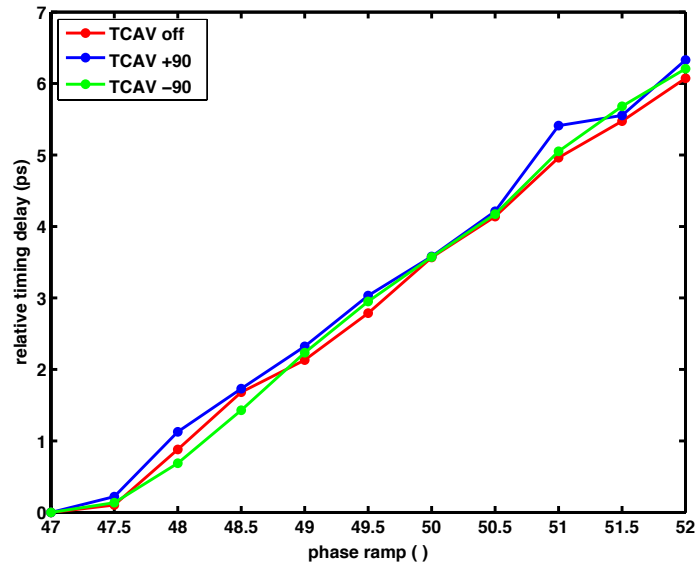
Figure 5.25: Phase ramp scans from 47° to 52° with TCAV on (+90° deflecting and -90° deflecting) and off as color-coded.

5.6 Plasma acceleration experiment

After we reduced "dark current" to a trivial level and found the relative time-of-arrival between laser pulse and electron bunch, we are ready to do 90°-injection. Figure 5.26 shows the trapped charge amount over timing scan around the time-of-arrival for different laser energies. When the laser energy is tuned up to 5 mJ, the trapped charge increases significantly compared to lower laser energy scans. This is due to they are in different regimes: When the laser energy is high enough, laser pulse can ionize sufficient He and H_2 molecules, thus creating a plasma cloud on the path of driver bunch. This plasma cloud can last about 1 ns (plasma recovery time) long. As long as the driver bunch passes in this ns window, part of plasma electrons will be trapped by the wake driven by driver bunch and form the witness bunch. This is called "plasma torch". In this regime, the timing requirement is not that strict since the "torch" can last about ns. We observe the trapped charge without much effort on finding t_0. However, the disadvantage of this regime, as you might expect from self-injection scheme, is that the witness bunch quality is not satisfying. As we lowered down the laser energy, it transits to a different regime where injection laser can only release a small amount of electrons which is barely enough for witness bunch, therefore it has to be injected into correct phase and trapped. Under this circumstance (so called "Trojan horse"), the timing synchronization needs to be narrowed down to 100 fs level which we have achieved as shown in last section. The timing requirement difference between two regimes are actually reflected in the Figure 5.26. The profile of trapped charge for 5 mJ laser appears to be a plateau as electrons will still be trapped when the laser arrives earlier than driver bunch. But "Trojan horse" regime is very sensitive to the timing delay, thus the profiles only peak at the t_0.

For the "plasma torch" regime, the pressure of 50:50-mixed gas was set to 4 torr. Dipole orbit energy was set to estimated witness beam energy 1 GeV. Quadrupoles were imaging 19.85 GeV. Laser energy was 5 mJ. Two example shots are shown in Figure 5.27. The beam energy in both shots is about 1 GeV with spread of 10%. The bunch charge varies shot by shot. On average, it is about several tens of pC after calibration.

In "Trojan horse" scheme, we also observed acceleration of trapped charge as in Figure 5.28. The beam energy and energy spread are about same as in "plasma torch" regime.
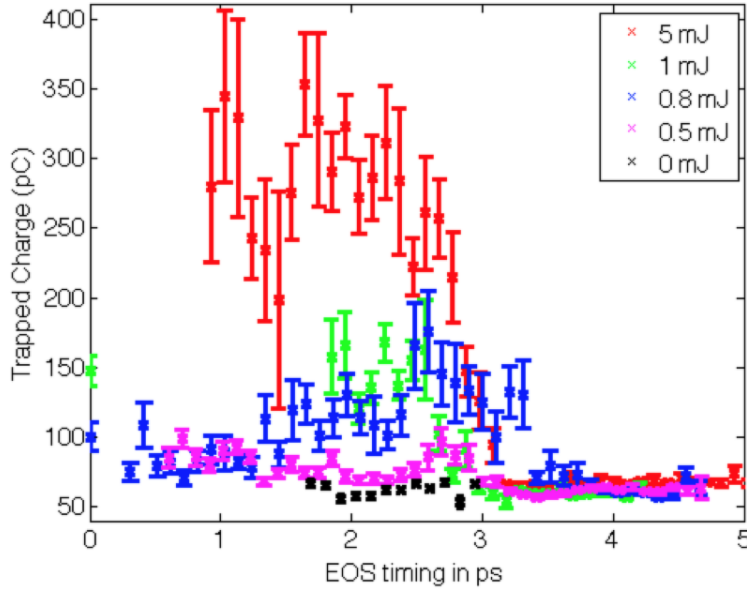
Figure 5.26: Plots of trapped charge as function of relative timing delay for different laser energies (5 mJ, 1 mJ, 0.8 mJ, 0.5 mJ, 0 mJ) as color-coded.

The averaged amount of charge is about the same as well.

The importance of beam emittance has been emphasized in Chapter 2. In experiment, measurement of emittance dependence on time in synchrotrons and storage rings allows to understand and possibly mitigate emittance growth issue. On LINAC, the knowledge of emittance at different locations provides guidance to tune beam optics such as quadrupoles. That is the reason why people have designed different methods to measure it. The first method is called "3-profile measurement" which is based on transverse beam profile. From Chapter 2, we already know the relation between emittance ε and twiss parameters α, β, γ. There are three unknowns given $\gamma\beta = 1 + \alpha^2$. Therefore, to determine the emittance at one certain location along the beam line, one needs at least three waist measurements with three different transfer matrices. Three different transfer matrices can be obtained from either three different profile monitor locations or three different quadrupole magnets settings. In drifting space, the beam waist can be written as $w^2 = \beta\varepsilon - 2L\alpha\varepsilon + L^2\gamma\varepsilon$. With three sets of (w, L), we can solve the equation list and obtain ε. In experiment, more sets of (w, L) are usually taken and the solution is found with fitting (this is called "butterfly" technique). Another way to measure emittance is called "Pepper-Pot" technique. If a bunch is projected to a screen, the information about

79
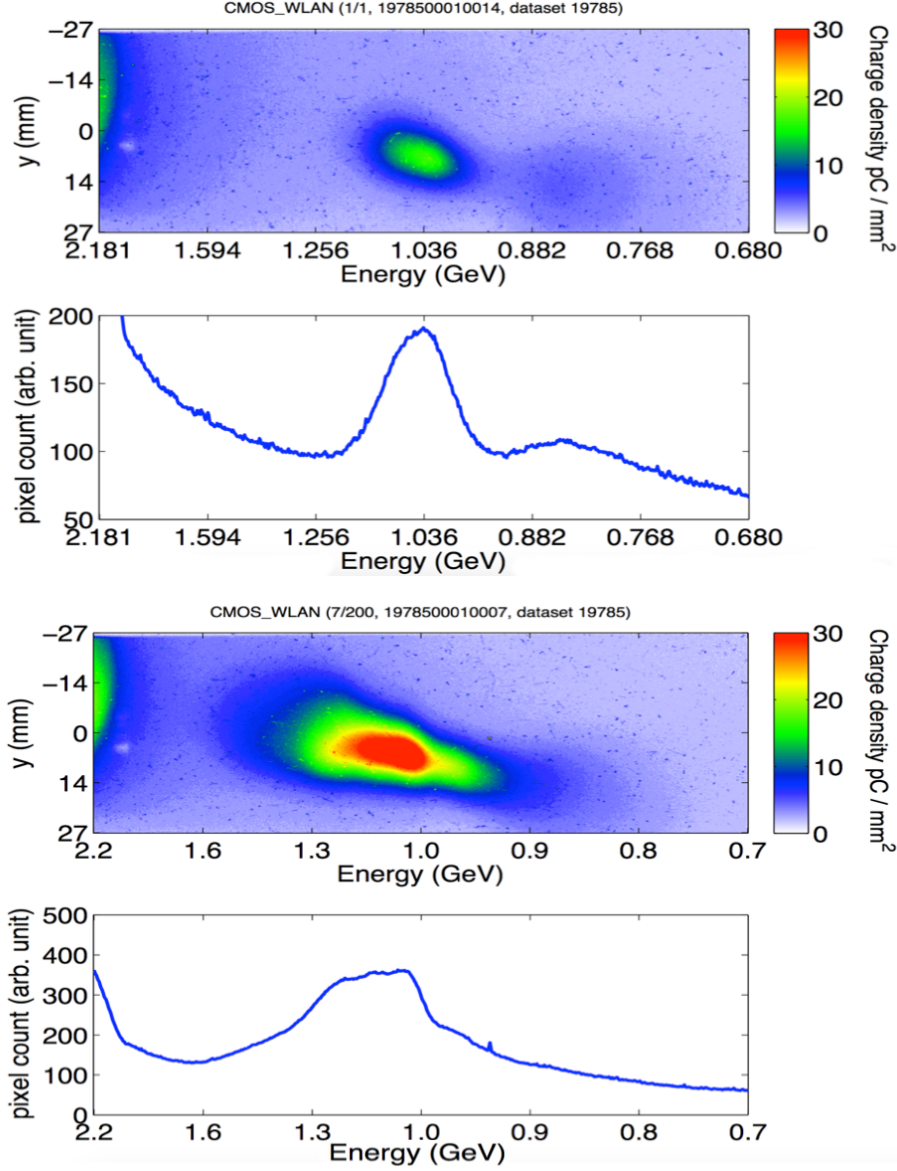
Figure 5.27: Two example shots in "plasma torch" regime. The Region of interest (ROI) is selected so that the massive driver bunch background is out of window. The charge density is color-coded as color bar in plot. Both images are projected to x-axis and plotted out in blue solid line.

angular distribution is lost. However, if the beam is collimated into a bunch of "beamlets" by small apertures and these beamlets can be detected on the following screen with a certain distance. The total intensity of each beamlet as a function of the position of the holes gives a transverse profile of the beam. The profiles of individual beamlets can be used to determine the angular distribution of the beam. The precision of this technique is limited by tradeoff between aperture size and the number of apertures. Smaller aper-
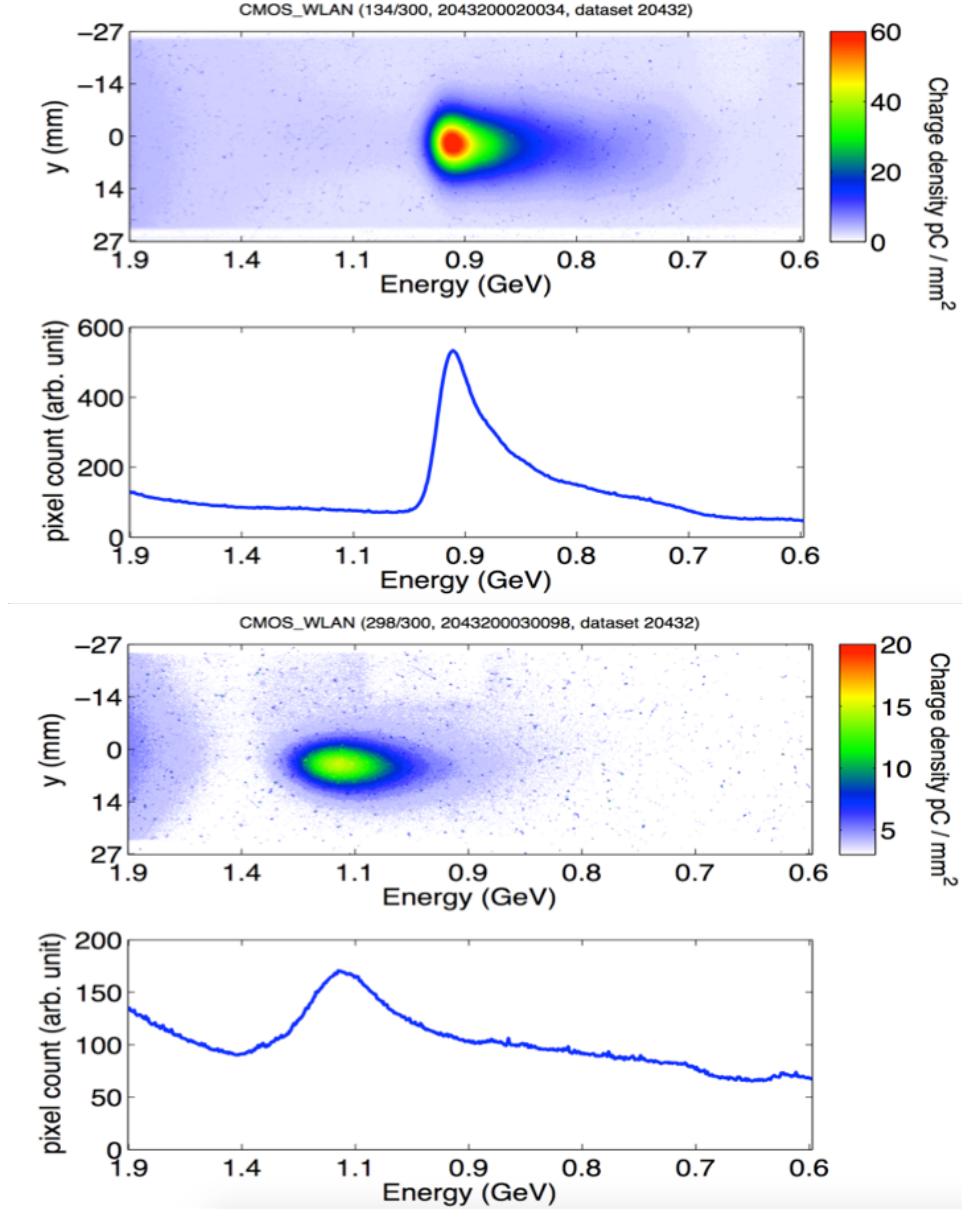
Figure 5.28: Two example shots in "trojan horse" regime similar to Figure 5.27

tures allow more precise determination of beamlets' position, but if the apertures are too small, they only sample a small fraction of the beam and the signal may be too weak to be detected.

However, these two methods mentioned above are not suitable in our experiment given the witness beam transverse dimension is very small and the bunch charge is only tens of pC against massive driver bunch background. Also, the witness beam energy is not very stable in our experiment. To evaluate the emittance as accurate as possible, we came up with a new emittance measurement method based on our knowledge of beam transport

line and spectrometer. The optics on beam line after witness bunch exits plasma are drawn in Figure 5.29. Without consideration of plasma downramp length, we assume the beta function of witness beam is about 1 mm based on operating plasma density. With that, if we optimize beam initial divergence by fitting the simulated beam profile to experiment result on spectrometer screen, we can obtain beam emittance from definition of beam divergence $2\sqrt{\gamma\varepsilon}$. The beam transport matrices include drifting space, focusing in quadrupoles, scattering in (diamond and aluminum) windows and dispersion in the dipole. Example shots are selected for demonstrating the analysis described above both in "plasma torch" and "trojan horse" regimes. With this method, we found for most of "plasma torch" shots, the divergence is about 800 μrad. With the beta function of 1 mm, the emittance is about 10^{-6} mrad while for "trojan horse" regime, the divergence is about 200 μrad which gives 5×10^{-8} mrad emittance.
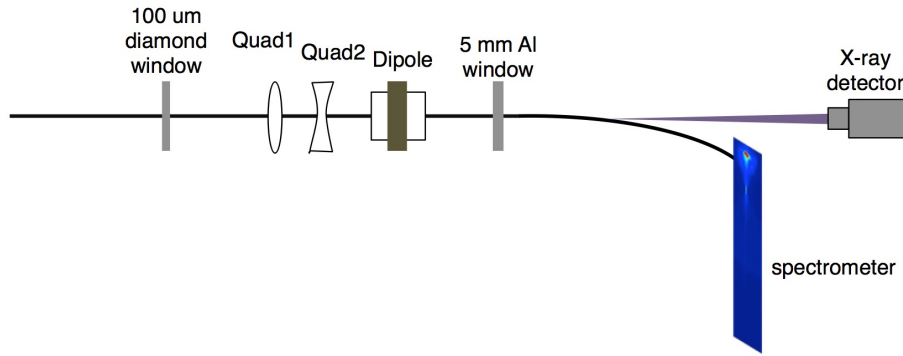
Figure 5.29: Schematic of downstream beam optics for diagnosis
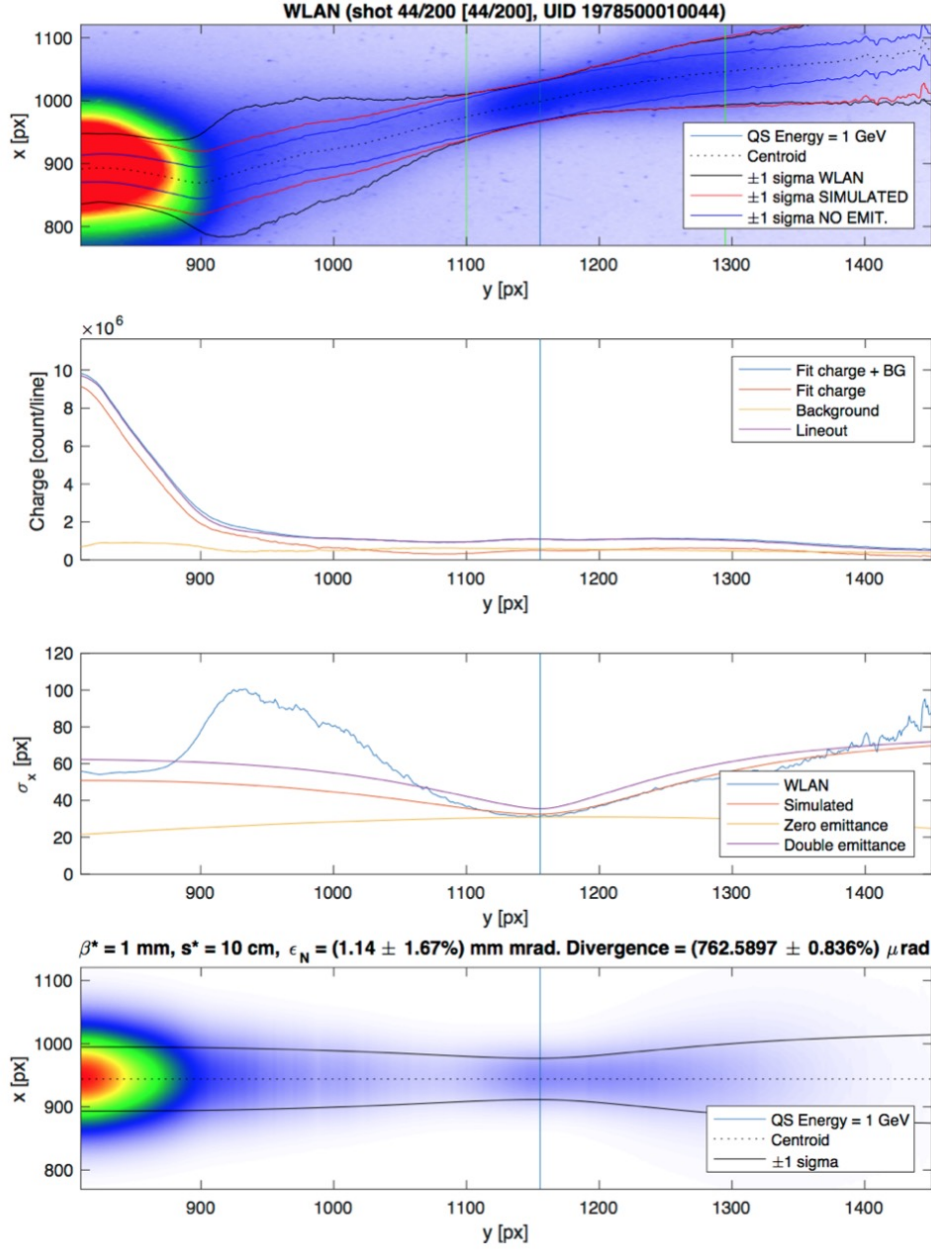
Figure 5.30: The divergence analysis for one sample shot from "plasma torch" regime. The first plot shows $\pm\sigma$ boundary when the beam does not have emittance (blue), from simulation (red) and the actual one based on the beam profile (black). The second plot shows the charge distribution over energy spectrum. The third plot shows the transverse beam size on energy spectrum. The fourth one gives the optimal divergence we found.
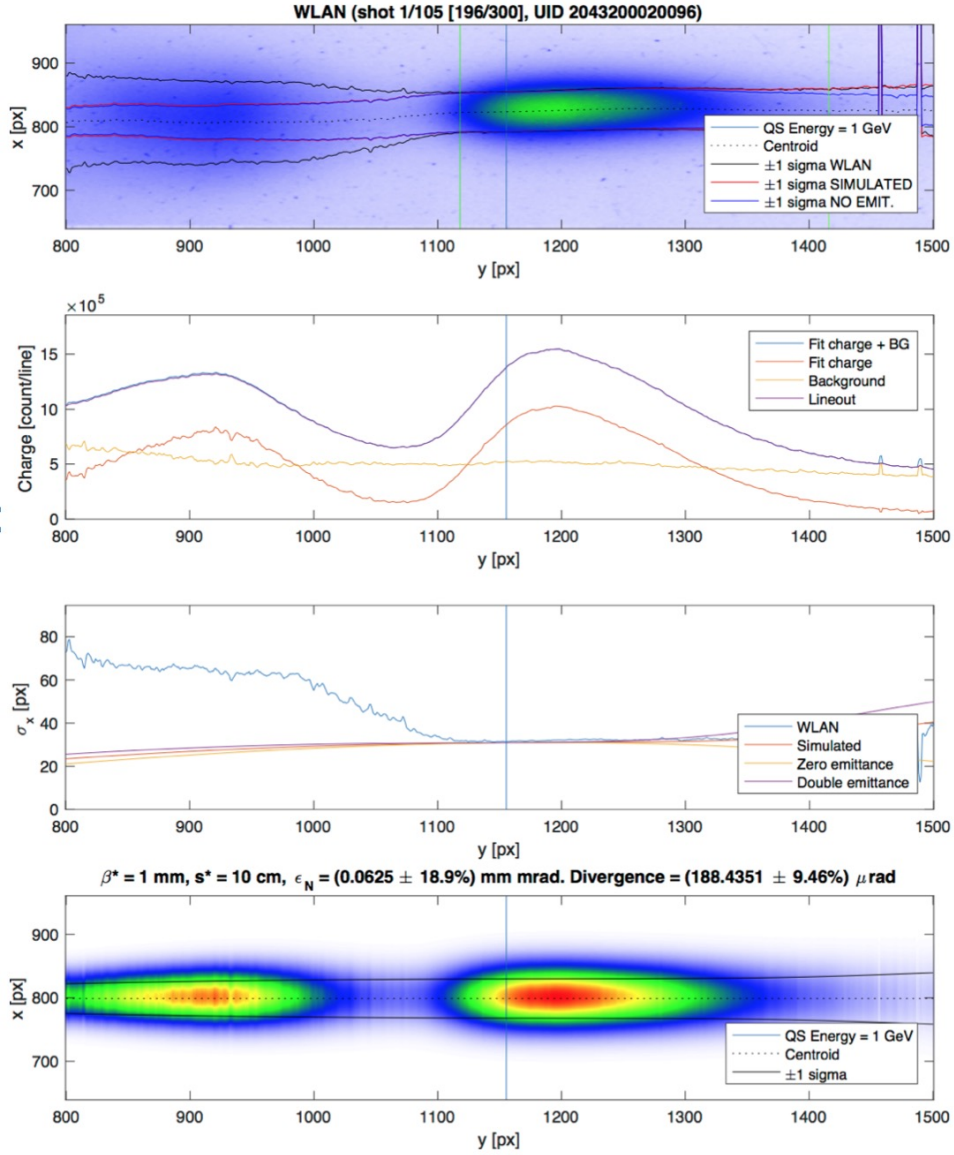
Figure 5.31: This plot is similar to Figure 5.30 except it is in "trojan horse" regime.

CHAPTER 6

Conclusion and future

6.1   Conclusions

In this dissertation, we mostly reported the experiment results we have obtained on FACET. As a proof-of-concept, the He electrons were trapped to be witness beam and accelerated successfully. By tuning laser energy, two regimes ("plasma torch" and "trojan horse") were created and tested. The beam obtained 1 GeV energy gain over several centimeters long plasma in laser ionization injection scheme. The energy spread is less than 10% and the emittance of beam is estimated between 10^{-6} mrad and 10^{-7} mrad.

Two major challenges: beam synchronization and dark current are discussed in detail. Given the plasma blowout regime size (100 μm), we have to synchronize injection laser and driver bunch to 100-fs level for injection. For 90° injection, we should find the relative time-of-arrival between two beams first. We achieved hundred femtosecond accuracy by scanning the timing delay and observing the intensity of plasma radiation generated by intense field of two beams. To observe the synchronization in real time and evaluate the relative timing jitter, we implemented non-invasive EOS system. After statistical analysis, the timing jitter is about 160 fs.

FACET driver bunch is strong enough to drive a wake and trap plasma electrons with main laser pre-ionization if the gas density (pressure) is too high. Thus we should optimize the gas pressure to reduce the dark current to trivial level. We found 4 Torr was an appropriate pressure that driver can drive a nice blowout regime inside without trapping noticeable plasma electrons.

6.2 FACET II

FACET has made tremendous progresses in many fields such as PWFA [CAA15, LAA14], dielectric wakefield [OAB16], THz pulse generation [WFG13], etc over last runs. In the light of phase one success, in 2016, the proposal of second phase, FACET-II, has been approved and supported by DOE. FACET-II will be the new test facility to develop advanced acceleration and coherent radiation techniques with high-energy electron and positron beams. Based on FACET, FACET-II will be upgraded to improve capabilities and breadth of the potential research. The design parameters for FACET-II are set for PWFA experiments. As shown in Figure 6.1, FACET-II will be located between Sector-10 and Sector-20. First 1/3 of linac will be for LCLS-II and last 1/3 stays as LCLS-I. Since only 1/3 of LINAC will be dedicated for FACET-II. The beam energy will be 10 GeV. Both dimensions of electron and positron bunch will be 10 μm $\times$ 10 μm $\times$ 10 μm. Bunch charge can be up to 6 nC. Thus, we can obtain over 10 kA peak current. The repetition rate is up to 30 Hz.
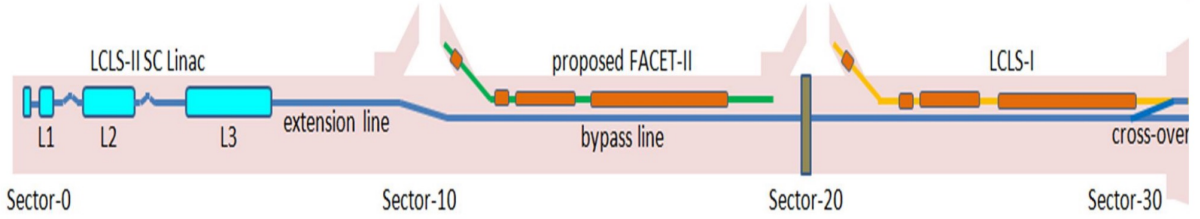
Figure 6.1: Conceptual layout of FACET-II in the middle third of the SLAC linac, downstream of LCLS-II and upstream of LCLS-I

Particularly, for our laser-ionization injection scheme PWFA, we measured that the timing jitter between laser pulse and electron beam is about 160 fs mostly because of the thermal cathode and the large compression factor of the electron bunch. In FACET-II, a new photoinjector and high-power laser will be installed and the timing jitter is expected to be less than 50 fs. With such excellent synchronization, the trapping point inside the blowout regime will be controlled more precisely once we determine the optimal spot for injection.

The high-density electron driver bunch in FACET-II also allows us to explore more

scenarios. At FACET, self-field of driver bunch is barely strong enough to self-ionize alkali metal vapor such as Rubidium or Lithium. This is reason why pre-ionization laser is set up. The intense field of FACET-II driver bunch is about 100 GV/m which is sufficient to ionize alkali metal vapor or even Hydrogen without any assistance of pre-ionization laser.

A high-power Joule-class (> 10 TW) Ti:Sa laser will be installed as well. This laser will still provide pre-ionization of gas medium, but this would decouple the acceleration process from the ability of the driver bunch to self-ionize the plasma medium. We can pre-ionize media which are gaseous at ambient conditions in a simpler container such as a glass vessel which is easy for laser injection and probing. In this case, it would be possible to study the ionization injection scheme when the electron beam density is much weaker than in the self-ionization case. The plasma length (acceleration length) can also be extended so the witness bunch is able to be accelerated higher energy.

A multi-stage acceleration scheme was also proposed at FACET-II that witness bunch energy is ramped up in several major radiofrequency-cavity-based stages. The first one accelerates beam to 200-250 MeV, the second to 4 GeV and the final one to 7 GeV or higher. Ionization injection scheme PWFA can be done after each of these stages. In Figure 6.2, the setup with three stages are drawn. The possible application of witness bunch coming out of the PWFA also shown afterwards. On first stage, the beam is accelerated to 250 MeV which is moderate for driving a wake over a limited distance. A LWFA can follow up and boost its energy to 1 GeV. Then the boosted bunch can be used as our PWFA driver. On second stage, the beam energy is already above 1 GeV which indicates it can be used for PWFA directly. On both stages, witness bunch could be used to power an undulator to produce FEL. On final stage, driver bunch energy hits 10 GeV, potentially the electron energy and flux of the driver beam and the witness beam may already be too high for current undulator. However, Thompson scattering light source can be built afterwards.
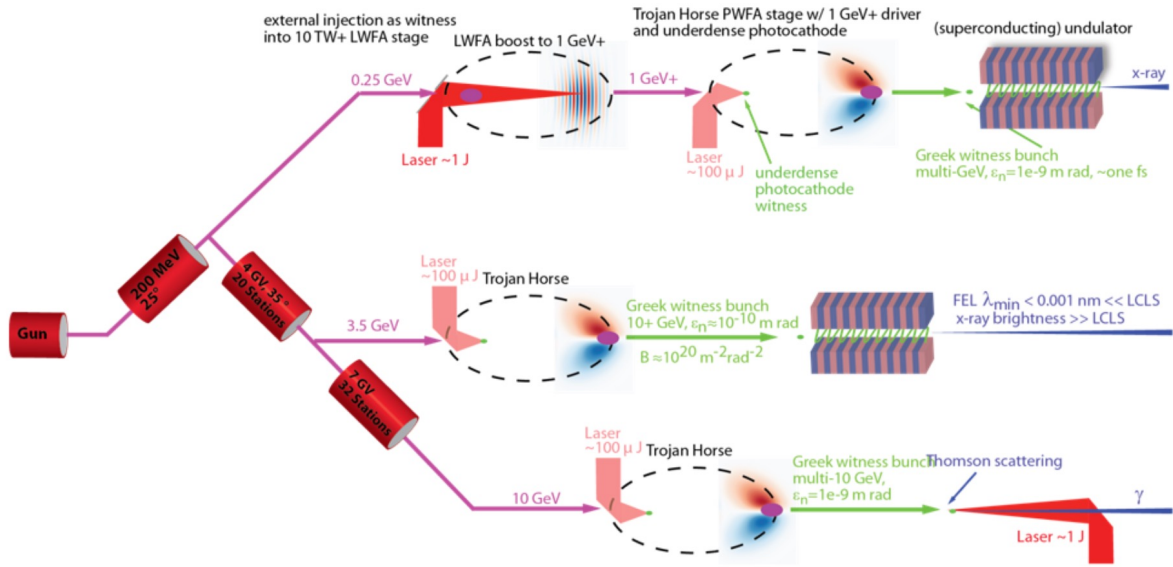
Figure 6.2: A conceptual sketch of multi-stage acceleration scheme at FACET-II. Beam is accelerated to 7 GeV or higher in three stages. On each stage, ionization-injection can be applied to the output for various uses.

Bibliography

[A 67]   V. S. Popov A. M. Perelomov. *Sov. Phys. JETP*, **25**:482, 1967.

[ACD98] R. Assmann, P. Chen, F.J. Decker, R. Iverson, P. Raimondi, T. Raubenheimer, S. Rokni, R. Siemann, D. Walz, D. Whittum, S. Chattopadhyay, W. Leemans, T. Katsouleas, S. Lee, C. Clayton, C. Joshi, K. Marsh, W. Mori, and G. Wang. "Proposal for a one GeV plasma wakefield acceleration experiment at {SLAC}." *Nuclear Instruments and Methods in Physics Research Section A: Accelerators, Spectrometers, Detectors and Associated Equipment*, **410**(3):396 – 406, 1998.

[ADE08] R. Akre, D. Dowell, P. Emma, J. Frisch, S. Gilevich, G. Hays, Ph. Hering, R. Iverson, C. Limborg-Deprey, H. Loos, A. Miahnahri, J. Schmerge, J. Turner, J. Welch, W. White, and J. Wu. "Commissioning the Linac Coherent Light Source injector." *Phys. Rev. ST Accel. Beams*, **11**:030703, Mar 2008.

[ADR09] A. Azima, S. Düsterer, P. Radcliffe, H. Redlin, N. Stojanovic, W. Li, H. Schlarb, J. Feldhaus, D. Cubaynes, M. Meyer, J. Dardis, P. Hayden, P. Hough, V Richardson, E. T. Kennedy, and J. T. Costello. "Time-resolved pump-probe experiments beyond the jitter limitations at FLASH." *Applied Physics Letters*, **94**(14), 2009.

[AGC15] E. Adli, S.J. Gessner, S. Corde, M.J. Hogan, and H.H. Bjerke. "Cherenkov light-based beam profiling for ultrarelativistic electron beams." *Nuclear Instruments and Methods in Physics Research Section A: Accelerators, Spectrometers, Detectors and Associated Equipment*, **783**:35 – 42, 2015.

[AT66]   V. S. Popov A. M. Perelomov and M. V. Terent'ev. *Sov. Phys. JETP*, **23**:924, 1966.

[AT67]   V. S. Popov A. M. Perelomov and M. V. Terent'ev. *Sov. Phys. JETP*, **24**:207, 1967.

[AZV13] W. An, M. Zhou, N. Vafaei-Najafabadi, K. A. Marsh, C. E. Clayton, C. Joshi, W. B. Mori, W. Lu, E. Adli, S. Corde, M. Litos, S. Li, S. Gessner, J. Fred-

erico, M. J. Hogan, D. Walz, J. England, J. P. Delahaye, and P. Muggli. "Strategies for mitigating the ionization-induced beam head erosion problem in an electron-beam-driven plasma wakefield accelerator." *Phys. Rev. ST Accel. Beams*, **16**:101301, Oct 2013.

[BCD07] Ian Blumenfeld, Christopher E. Clayton, Franz-Josef Decker, Mark J. Hogan, Chengkun Huang, Rasmus Ischebeck, Richard Iverson, Chandrashekhar Joshi, Thomas Katsouleas, Neil Kirby, Wei Lu, Kenneth A. Marsh, Warren B. Mori, Patric Muggli, Erdem Oz, Robert H. Siemann, Dieter Walz, and Miaomiao Zhou. "Energy doubling of 42 GeV electrons in a metre-scale plasma wakefield accelerator." *Nature*, **445**(7129):741–744, 02 2007. *[10.1038/nature05538.]*

[BCD10] I. Blumenfeld, C. E. Clayton, F. J. Decker, M. J. Hogan, C. Huang, R. Ischebeck, R. H. Iverson, C. Joshi, T. Katsouleas, N. Kirby, W. Lu, K. A. Marsh, W. B. Mori, P. Muggli, E. Oz, R. H. Siemann, D. R. Walz, and M. Zhou. "Scaling of the longitudinal electric field and transformer ratio in a nonlinear plasma wakefield accelerator." *Phys. Rev. ST Accel. Beams*, **13**:111301, Nov 2010.

[BGJ07] G. Berden, W. A. Gillespie, S. P. Jamison, E.-A. Knabbe, A. M. MacLeod, A. F. G. van der Meer, P. J. Phillips, H. Schlarb, B. Schmidt, P. Schmüser, and B. Steffen. "Benchmarking of Electro-Optic Monitors for Femtosecond Electron Bunches." *Phys. Rev. Lett.*, **99**:164801, Oct 2007.

[BK74] J. E. Bayfield and P. M. Koch. "Multiphoton Ionization of Highly Excited Hydrogen Atoms." *Phys. Rev. Lett.*, **33**:258–261, Jul 1974.

[BL85] C. K. Birdsall and A. B. Langdon. *Plasma Physics via Computer Simulation.* McGraw-Hill, 1985.

[BNP98] S. Bulanov, N. Naumova, F. Pegoraro, and J. Sakai. "Particle injection into the wave acceleration phase due to nonlinear wake wave breaking." *Phys. Rev. E*, **58**:R5257–R5260, Nov 1998.

[Bor70] J. P. Boris. "Relativistic plasma simulation - optimization of a hybrid code." In *Proc. Fourth Conf. Numerical Simulation of Plasmas*, pp. 3–67, 1970.

[BPN84] R. Bonifacio, C. Pellegrini, and L.M. Narducci. "Collective instabilities and high-gain regime in a free electron laser." *Optics Communications*, **50**(6):373 – 378, 1984.

[BPR12] S. Banerjee, N. D. Powers, V. Ramanathan, I. Ghebregziabher, K. J. Brown, C. M. Maharjan, S. Chen, A. Beck, E. Lefebvre, S. Y. Kalmykov, B. A. Shadwick, and D. P. Umstadter. "Generation of tunable, 100–800 MeV quasi-monoenergetic electron beams from a laser-wakefield accelerator in the blowout regimea)." *Physics of Plasmas*, **19**(5), 2012.

[BR39] B. von Borries and E. Rushka. *Z. Tech. Phys.*, **20**(225), 1939.

[BR94] N. Barov and J. B. Rosenzweig. "Propagation of short electron pulses in underdense plasmas." *Phys. Rev. E*, **49**:4407–4416, May 1994.

[Buc07] Philip H. Bucksbaum. "The Future of Attosecond Spectroscopy." *Science*, **317**(5839):766–769, 2007.

[Bun59] O. Buneman. "Dissipation of Currents in Ionized Media." *Phys. Rev.*, **115**:503–517, Aug 1959.

[CAA15] S. Corde, E. Adli, J. M. Allen, W. An, C. I. Clarke, C. E. Clayton, J. P. Delahaye, J. Frederico, S. Gessner, S. Z. Green, M. J. Hogan, C. Joshi, N. Lipkowitz, M. Litos, W. Lu, K. A. Marsh, W. B. Mori, M. Schmeltz, N. Vafaei-Najafabadi, D. Walz, V. Yakimenko, and G. Yocky. "Multi-gigaelectronvolt acceleration of positrons in a self-loaded plasma wakefield." *Nature*, **524**(7566):442–445, 08 2015.

[CBD02] C. E. Clayton, B. E. Blue, E. S. Dodd, C. Joshi, K. A. Marsh, W. B. Mori, S. Wang, P. Catravas, S. Chattopadhyay, E. Esarey, W. P. Leemans, R. Assmann, F. J. Decker, M. J. Hogan, R. Iverson, P. Raimondi, R. H. Siemann, D. Walz, T. Katsouleas, S. Lee, and P. Muggli. "Transverse Envelope Dynamics of a 28.5-GeV Electron Beam in a Long Plasma." *Phys. Rev. Lett.*, **88**:154801, Apr 2002.

[CDH85] Pisin Chen, J. M. Dawson, Robert W. Huff, and T. Katsouleas. "Acceleration of Electrons by the Interaction of a Bunched Electron Beam with a Plasma." *Phys. Rev. Lett.*, **54**:693–696, Feb 1985.

[Cha03] Thomas Katsouleas Chandrashekhar Joshi. "Plasma accelerators at the energy frontier and on tabletops." *Physics Today*, **56**(6):7, Jun 2003.

[Cor93] P. B. Corkum. "Plasma perspective on strong field multiphoton ionization." *Phys. Rev. Lett.*, **71**:1994–1997, Sep 1993.

[CRA10] C. E. Clayton, J. E. Ralph, F. Albert, R. A. Fonseca, S. H. Glenzer, C. Joshi, W. Lu, K. A. Marsh, S. F. Martins, W. B. Mori, A. Pak, F. S. Tsung, B. B. Pollock, J. S. Ross, L. O. Silva, and D. H. Froula. "Self-Guided Laser Wakefield Acceleration beyond 1 GeV Using Ionization-Induced Injection." *Phys. Rev. Lett.*, **105**:105003, Sep 2010.

[CSM06] Min Chen, Zheng-Ming Sheng, Yan-Yun Ma, and Jie Zhang. "Electron injection and trapping in a laser wakefield by field ionization to high-charge states of gases." *Journal of Applied Physics*, **99**(5), 2006.

[Daw59] J. M. Dawson. "Nonlinear Electron Oscillations in a Cold Plasma." *Phys. Rev.*, **113**:383–387, Jan 1959.

[Daw62] John Dawson. "One Dimensional Plasma Model." *Physics of Fluids*, **5**(4):445–459, 1962.

[DBC06] S. Deng, C. D. Barnes, C. E. Clayton, C. O'Connell, F. J. Decker, R. A. Fonseca, C. Huang, M. J. Hogan, R. Iverson, D. K. Johnson, C. Joshi, T. Katsouleas, P. Krejcik, W. Lu, W. B. Mori, P. Muggli, E. Oz, F. Tsung, D. Walz, and M. Zhou. "Hose Instability and Wake Generation by an Intense Electron Beam in a Self-Ionized Gas." *Phys. Rev. Lett.*, **96**:045001, Jan 2006.

[DFH91] N. Davidson, A. A. Friesem, and E. Hasman. "Holographic axilens: high resolution and long focal depth." *Opt. Lett.*, **16**(7):523–525, Apr 1991.

[DG03] John R. Cary Eric Esarey Wim Leemans David L. Bruhwiler, D. A. Dimitrov and Rodolfo E. Giacone. "Particle-in-cell simulations of tunneling ionization effects in plasma-based accelerators." *Phys. Plasmas*, **10**:2022, 2003.

[DK98] N. B. Delone and V. P. Krainov. *Phys. Usp.*, **41**:469, 1998.

[DLR09] X. Davoine, E. Lefebvre, C. Rechatin, J. Faure, and V. Malka. "Cold Optical Injection Producing Monoenergetic, Multi-GeV Electron Bunches." *Phys. Rev. Lett.*, **102**:065001, Feb 2009.

[E 05] T. Katsouleas P. Muggli R. Iverson D.K. Johnson P. Krejcik C. O'Connell R.H. Siemann D. Walz C.E. Clayton C. Huang C. Joshi W. Lu K.A. Marsh W.B. Mori M. Zhou E. Oz, S. Deng. "Plasma Dark Current in Self-Ionized Plasma Wakefield Accelerators." *Particle accelerator. Proceedings, Conference, PAC'05*, **C0505161**:3444, 2005.

[EHL97] E. Esarey, R. F. Hubbard, W. P. Leemans, A. Ting, and P. Sprangle. "Electron Injection into Plasma Wakefields by Colliding Laser Pulses." *Phys. Rev. Lett.*, **79**:2682–2685, Oct 1997.

[Fai73] F. H. M. Faisal. "Multiple absorption of laser photons by atoms." *J. Phys. B*, **6**:L89, 1973.

[FGP04] J. Faure, Y. Glinec, A. Pukhov, S. Kiselev, S. Gordienko, E. Lefebvre, J. P. Rousseau, F. Burgy, and V. Malka. "A laser-plasma accelerator producing monoenergetic electron beams." *Nature*, **431**(7008):541–544, 09 2004. *[10.1038/nature02963.]*

[FMC01] M. J. Fitch, A. C. Melissinos, P. L. Colestock, J.-P. Carneiro, H. T. Edwards, and W. H. Hartung. "Electro-optic Measurement of the Wake Fields of a Relativistic Electron Beam." *Phys. Rev. Lett.*, **87**:034801, Jun 2001.

[FRN06] J. Faure, C. Rechatin, A. Norlin, A. Lifschitz, Y. Glinec, and V. Malka. "Controlled injection and acceleration of electrons in plasma wakefields by colliding laser pulses." *Nature*, **444**(7120):737–739, 12 2006. *[10.1038/nature05393.]*

[GBL11] Vasileios-Marios Gkortsas, Siddharth Bhardwaj, Chien-Jen Lai, Kyung-Han Hong, Edilson L. Falcão Filho, and Franz X. Kärtner. "Interplay of mulitphoton and tunneling ionization in short-wavelength-driven high-order harmonic generation." *Phys. Rev. A*, **84**:013427, Jul 2011.

[GNL11] A. J. Gonsalves, K. Nakamura, C. Lin, D. Panasenko, S. Shiraishi, T. Sokollik, C. Benedetti, C. B. Schroeder, C. G. R. Geddes, J. van Tilborg, J. Osterhoff, E. Esarey, C. Toth, and W. P. Leemans. "Tunable laser plasma accelerator based on longitudinal density tailoring." *Nat Phys*, **7**(11):862–866, 11 2011. [10.1038/nphys2071.]

[GNP08] C. G. R. Geddes, K. Nakamura, G. R. Plateau, Cs. Toth, E. Cormier-Michel, E. Esarey, C. B. Schroeder, J. R. Cary, and W. P. Leemans. "Plasma-Density-Gradient Injection of Low Absolute-Momentum-Spread Electron Bunches." *Phys. Rev. Lett.*, **100**:215004, May 2008.

[GTT04] C. G. R. Geddes, Cs. Toth, J. van Tilborg, E. Esarey, C. B. Schroeder, D. Bruhwiler, C. Nieter, J. Cary, and W. P. Leemans. "High-quality electron beams from a laser wakefield accelerator using plasma-channel guiding." *Nature*, **431**(7008):538–541, 09 2004. [10.1038/nature02900.]

[HAD00] M. J. Hogan, R. Assmann, F.-J. Decker, R. Iverson, P. Raimondi, S. Rokni, R. H. Siemann, D. Walz, D. Whittum, B. Blue, C. E. Clayton, E. Dodd, R. Hemker, C. Joshi, K. A. Marsh, W. B. Mori, S. Wang, T. Katsouleas, S. Lee, P. Muggli, P. Catravas, S. Chattopadhyay, E. Esarey, and W. P. Leemans. "E-157: A 1.4-m-long plasma wake field acceleration experiment using a 30 GeV electron beam from the Stanford Linear Accelerator Center Linac." *Physics of Plasmas*, **7**(5):2241–2248, 2000.

[HBP94] S.C. Hartman, N. Barov, C. Pellegrini, S. Park, J. Rosenzweig, G. Travish, R. Zhang, C. Clayton, P. Davis, M. Everett, C. Joshi, and G. Hairapetian. "Initial measurements of the UCLA rf photoinjector." *Nuclear Instruments and Methods in Physics Research Section A: Accelerators, Spectrometers, Detectors and Associated Equipment*, **340**(1):219 – 230, 1994.

[HE81] R. W. Hockney and J. W. Eastwood. *Computer Simulation Using Particles.* McGraw-Hill, 1981.

[HKO10] B. Hidding, T. Königstein, J. Osterholz, S. Karsch, O. Willi, and G. Pretzler. "Monoenergetic Energy Doubling in a Hybrid Laser-Plasma Wakefield Accelerator." *Phys. Rev. Lett.*, **104**:195002, May 2010.

[HPR12] B. Hidding, G. Pretzler, J. B. Rosenzweig, T. Königstein, D. Schiller, and D. L. Bruhwiler. "Ultracold Electron Bunch Generation via Plasma Photocathode Emission and Acceleration in a Beam-Driven Plasma Blowout." *Phys. Rev. Lett.*, **108**:035001, Jan 2012.

[HRX] B. Hidding, J. B. Rosenzweig, Y. Xi, F. H. O'Shea, F. H., G. Andonian, D. Schiller, S. Barber, O. Williams, G. Pretzler, T. Königstein, F. Kleeschulte, M. J. Hogan, M. Litos, S. Corde, W. W. White, P. Muggli, D. L. Bruhwiler, and K. Lotov. *AIP Conference Proceedings*, (1):570.

[JAB06] D. K. Johnson, D. Auerbach, I. Blumenfeld, C. D. Barnes, C. E. Clayton, F. J. Decker, S. Deng, P. Emma, M. J. Hogan, C. Huang, R. Ischebeck, R. Iverson, C. Joshi, T. C. Katsouleas, N. Kirby, P. Krejcik, W. Lu, K. A. Marsh, W. B. Mori, P. Muggli, C. L. O'Connell, E. Oz, R. H. Siemann, D. Walz, and M. Zhou. "Positron Production by X Rays Emitted by Betatron Motion in a Plasma Wiggler." *Phys. Rev. Lett.*, **97**:175003, Oct 2006.

[Jos07] C. Joshi. "The development of laser- and beam-driven plasma accelerators as an experimental fielda)." *Physics of Plasmas*, **14**(5), 2007.

[Kat86] T. Katsouleas. "Physical mechanisms in the plasma wake-field accelerator." *Phys. Rev. A*, **33**:2056–2064, Mar 1986.

[KBY11] S. Y. Kalmykov, A. Beck, S. A. Yi, V. N. Khudik, M. C. Downer, E. Lefebvre, B. A. Shadwick, and D. P. Umstadter. "Electron self-injection into an evolving plasma bubble: Quasi-monoenergetic laser-plasma acceleration in the blowout regimea)." *Physics of Plasmas*, **18**(5), 2011.

[Kel65] L. V. Keldysh. "Ionization in the Field of a Strong Electromagnetic Wave." *Sov. Phys. JETP*, **20**:1307, 1965.

[Kim89] Kwang-Je Kim. "Rf and space-charge effects in laser-driven rf electron guns." *Nuclear Instruments and Methods in Physics Research Section A: Accelerators, Spectrometers, Detectors and Associated Equipment*, **275**(2):201 – 218, 1989.

[KSK92] Jeffrey L. Krause, Kenneth J. Schafer, and Kenneth C. Kulander. "High-order harmonic generation from atoms and ions in the high intensity regime." *Phys. Rev. Lett.*, **68**:3535–3538, Jun 1992.

[KYB11] S Y Kalmykov, S A Yi, A Beck, A F Lifschitz, X Davoine, E Lefebvre, V Khudik, G Shvets, and M C Downer. "Dark-current-free petawatt laser-driven wakefield accelerator based on electron self-injection into an expanding plasma bubble." *Plasma Physics and Controlled Fusion*, **53**(1):014006, 2011.

[LAA14] M. Litos, E. Adli, W. An, C. I. Clarke, C. E. Clayton, S. Corde, J. P. Delahaye, R. J. England, A. S. Fisher, J. Frederico, S. Gessner, S. Z. Green, M. J. Hogan, C. Joshi, W. Lu, K. A. Marsh, W. B. Mori, P. Muggli, N. Vafaei-Najafabadi, D. Walz, G. White, Z. Wu, V. Yakimenko, and G. Yocky. "High-efficiency acceleration of an electron beam in a plasma wakefield accelerator." *Nature*, **515**(7525):92–95, 11 2014.

[Lap71] P. Lapostolle. *IEEE Trans. Nucl. Sci.*, **18**(1101), 1971.

[LHZ05] W. Lu, C. Huang, M. M. Zhou, W. B. Mori, and T. Katsouleas. "Limits of linear plasma wakefield theory for electron or positron beams." *Physics of Plasmas*, **12**(6), 2005.

[LHZ06] W. Lu, C. Huang, M. Zhou, M. Tzoufras, F. S. Tsung, W. B. Mori, and T. Katsouleas. "A nonlinear theory for multidimensional relativistic plasma wave wakefieldsa)." *Physics of Plasmas*, **13**(5), 2006.

[Lot04] K. V. Lotov. "Blowout regimes of plasma wakefield acceleration." *Phys. Rev. E*, **69**:046405, Apr 2004.

[LWM14] Alexandra S. Landsman, Matthias Weger, Jochen Maurer, Robert Boge, André Ludwig, Sebastian Heuser, Claudio Cirelli, Lukas Gallmann, and Ursula Keller. "Ultrafast resolution of tunneling delay time." *Optica*, **1**(5):343–349, Nov 2014.

[LXW11] J. S. Liu, C. Q. Xia, W. T. Wang, H. Y. Lu, Ch. Wang, A. H. Deng, W. T. Li, H. Zhang, X. Y. Liang, Y. X. Leng, X. M. Lu, C. Wang, J. Z. Wang, K. Nakajima, R. X. Li, and Z. Z. Xu. "All-Optical Cascaded Laser Wakefield Accelerator Using Ionization-Induced Injection." *Phys. Rev. Lett.*, **107**:035001, Jul 2011.

[McL54] John H. McLeod. "The Axicon: A New Type of Optical Element." *J. Opt. Soc. Am.*, **44**(8):592–597, Aug 1954.

[MFL10] S. F. Martins, R. A. Fonseca, W. Lu, W. B. Mori, and L. O. Silva. "Exploring laser-wakefield-accelerator regimes for near-term lasers using particle-in-cell simulation in Lorentz-boosted frames." *Nat Phys*, **6**(4):311–316, 04 2010. [10.1038/nphys1538.]

[MH09] Patric Muggli and Mark J. Hogan. "Review of high-energy plasma wakefield experiments." *Comptes Rendus Physique*, **10**(2):116 – 129, 2009.

[MK86] N.B. Delone M.V. Ammosov and V.P. Krainov. "Tunnel ionization of complex atoms and of atomic ions in an alternating electromagnetic field." *Sov. Phys. JETP*, **64**:1191, 1986.

[MMN04] S. P. D. Mangles, C. D. Murphy, Z. Najmudin, A. G. R. Thomas, J. L. Collier, A. E. Dangor, E. J. Divall, P. S. Foster, J. G. Gallacher, C. J. Hooker, D. A. Jaroszynski, A. J. Langley, W. B. Mori, P. A. Norreys, F. S. Tsung, R. Viskup, B. R. Walton, and K. Krushelnick. "Monoenergetic beams of relativistic electrons from intense laser-plasma interactions." *Nature*, **431**(7008):535–538, 09 2004. [10.1038/nature02939.]

[MMR12] A. R. Maier, A. Meseck, S. Reiche, C. B. Schroeder, T. Seggebrock, and F. Grüner. "Demonstration Scheme for a Laser-Plasma-Driven Free-Electron Laser." *Phys. Rev. X*, **2**:031019, Sep 2012.

[MTS10] C. McGuffey, A. G. R. Thomas, W. Schumaker, T. Matsuoka, V. Chvykov, F. J. Dollar, G. Kalintchenko, V. Yanovsky, A. Maksimchuk, K. Krushelnick, V. Yu. Bychenkov, I. V. Glazyrin, and A. V. Karpeev. "Ionization Induced Trapping in a Laser Wakefield Accelerator." *Phys. Rev. Lett.*, **104**:025004, Jan 2010.

[NC04] Chet Nieter and John R. Cary. "VORPAL: a versatile plasma simulation code." *Journal of Computational Physics*, **196**(2):448 – 473, 2004.

[Nic83] Dwight R. Nicholson. *Introduction to Plasma Theory.* John Wiley & Sons, 1983.

[NR66] A. I. Nikishov and V. I. Ritus. *Sov. Phys. JETP*, **23**:162, 1966.

[OAB16] B. D. O'Shea, G. Andonian, S. K. Barber, K. L. Fitzmorris, S. Hakimi, J. Harrison, P. D. Hoang, M. J. Hogan, B. Naranjo, O. B. Williams, V. Yakimenko, and J. B. Rosenzweig. "Observation of acceleration and deceleration in gigaelectron-volt-per-metre gradient dielectric wakefield accelerators." *Nature Communications*, **7**:12763 EP –, 09 2016.

[ODK07] E. Oz, S. Deng, T. Katsouleas, P. Muggli, C. D. Barnes, I. Blumenfeld, F. J. Decker, P. Emma, M. J. Hogan, R. Ischebeck, R. H. Iverson, N. Kirby, P. Krejcik, C. O'Connell, R. H. Siemann, D. Walz, D. Auerbach, C. E. Clayton, C. Huang, D. K. Johnson, C. Joshi, W. Lu, K. A. Marsh, W. B. Mori, and M. Zhou. "Ionization-Induced Electron Trapping in Ultrarelativistic Plasma Wakes." *Phys. Rev. Lett.*, **98**:084801, Feb 2007.

[OMR10] F. H. O'Shea, G. Marcus, J. B. Rosenzweig, M. Scheer, J. Bahrdt, R. Weingartner, A. Gaupp, and F. Grüner. "Short period, high field cryogenic undulator for extreme performance x-ray free electron lasers." *Phys. Rev. ST Accel. Beams*, **13**:070702, Jul 2010.

[OSD02] C. E. Clayton E. Dodd C. Huang K. A. Marsh W. B. Mori REVIEW PAPERS High energy density plasma science with an ultrarelativistic electron beam a Ö C. Joshi, B. Blue, C. O'Connell R. Siemann S. Wang, M. J. Hogan, T. Kat-

souleas D. Walz, P. Muggli, and S. Lee. "High energy density plasma science with an ultrarelativistic electron beam." *Physics of Plasmas*, **9**(5), 2002.

[PCR11] B. B. Pollock, C. E. Clayton, J. E. Ralph, F. Albert, A. Davidson, L. Divol, C. Filip, S. H. Glenzer, K. Herpoldt, W. Lu, K. A. Marsh, J. Meinecke, W. B. Mori, A. Pak, T. C. Rensink, J. S. Ross, J. Shaw, G. R. Tynan, C. Joshi, and D. H. Froula. "Demonstration of a Narrow Energy Spread, ~ 0.5 GeV Electron Beam from a Two-Stage Laser Wakefield Accelerator." *Phys. Rev. Lett.*, **107**:045001, Jul 2011.

[PMM10] A. Pak, K. A. Marsh, S. F. Martins, W. Lu, W. B. Mori, and C. Joshi. "Injection and Trapping of Tunnel-Ionized Electrons into Laser-Produced Wakes." *Phys. Rev. Lett.*, **104**:025003, Jan 2010.

[Pop04] V. S. Popov. *Phys. Usp.*, **47**:855, 2004.

[RAA08] J.B. Rosenzweig, D. Alesini, G. Andonian, M. Boscolo, M. Dunning, L. Faillace, M. Ferrario, A. Fukusawa, L. Giannessi, E. Hemsing, G. Marcus, A. Marinelli, P. Musumeci, B. O'Shea, L. Palumbo, C. Pellegrini, V. Petrillo, S. Reiche, C. Ronsivalle, B. Spataro, and C. Vaccarezza. "Generation of ultra-short, high brightness electron beams for single-spike {SASE} {FEL} operation." *Nuclear Instruments and Methods in Physics Research Section A: Accelerators, Spectrometers, Detectors and Associated Equipment*, **593**(1–2):39 – 44, 2008. {FEL} Fronties 2007Proceedings of the International Workshop on Frontiers in {FEL} Physics and Related Topics.

[RBK91] J. B. Rosenzweig, B. Breizman, T. Katsouleas, and J. J. Su. "Acceleration and focusing of electrons in two-dimensional nonlinear plasma wake fields." *Phys. Rev. A*, **44**:R6189–R6192, Nov 1991.

[RCC88] J. B. Rosenzweig, D. B. Cline, B. Cole, H. Figueroa, W. Gai, R. Konecny, J. Norem, P. Schoessow, and J. Simpson. "Experimental Observation of Plasma Wake-Field Acceleration." *Phys. Rev. Lett.*, **61**:98–101, Jul 1988.

[RCS05] J. B. Rosenzweig, A. M. Cook, A. Scott, M. C. Thompson, and R. B. Yoder.

"Effects of Ion Motion in Intense Beam-Driven Plasma Wakefield Accelerators." *Phys. Rev. Lett.*, **95**:195002, Oct 2005.

[Rei80] H. R. Reiss. "Effect of an intense electromagnetic field on a weakly bound system." *Phys. Rev. A*, **22**:1786, 1980.

[Ros87] J. B. Rosenzweig. "Nonlinear plasma dynamics in the plasma wake-field accelerator." *Phys. Rev. Lett.*, **58**:555–558, Feb 1987.

[RSC89] J. B. Rosenzweig, P. Schoessow, B. Cole, W. Gai, R. Konecny, J. Norem, and J. Simpson. "Experimental measurement of nonlinear plasma wake fields." *Phys. Rev. A*, **39**:1586–1589, Feb 1989.

[Sac71] F. J. Sacherer. *IEEE Trans. Nucl. Sci.*, **18**(1105), 1971.

[SBR01] H. Suk, N. Barov, J. B. Rosenzweig, and E. Esarey. "Plasma Electron Trapping and Acceleration in a Plasma Wake Field Using a Density Transition." *Phys. Rev. Lett.*, **86**:1011–1014, Feb 2001.

[SBS10] K. Schmid, A. Buck, C. M. S. Sears, J. M. Mikhailova, R. Tautz, D. Herrmann, M. Geissler, F. Krausz, and L. Veisz. "Density-transition based electron injector for laser driven wakefield accelerators." *Phys. Rev. ST Accel. Beams*, **13**:091301, Sep 2010.

[SES06] C. B. Schroeder, E. Esarey, B. A. Shadwick, and W. P. Leemans. "Trapping, dark current, and wave breaking in nonlinear plasma waves." *Physics of Plasmas*, **13**(3), 2006.

[SMM10] C. M. Scoby, P. Musumeci, J. T. Moody, and M. S. Gutierrez. "Electro-optic sampling at 90 degree interaction geometry for time-of-arrival stamping of ultrafast relativistic electron diffraction." *Phys. Rev. ST Accel. Beams*, **13**:022801, Feb 2010.

[SR97] Luca Serafini and James B. Rosenzweig. "Envelope analysis of intense relativistic quasilaminar beams in rf photoinjectors:mA theory of emittance compensation." *Phys. Rev. E*, **55**:7565–7590, Jun 1997.

[SS87] J. M. Dawson P. Chen S. Wilks, T. Katsouleas and J. J. Su. "Beam Loading in Plasma-Waves." *IEEE Transactions on Plasma Science*, **15**(2):210–217, 1987.

[TD79] T. Tajima and J. M. Dawson. "Laser Electron Accelerator." *Phys. Rev. Lett.*, **43**:267–270, Jul 1979.

[TLT08] M. Tzoufras, W. Lu, F. S. Tsung, C. Huang, W. B. Mori, T. Katsouleas, J. Vieira, R. A. Fonseca, and L. O. Silva. "Beam Loading in the Nonlinear Regime of Plasma-Based Acceleration." *Phys. Rev. Lett.*, **101**:145002, Sep 2008.

[TSF06] J. van Tilborg, C. B. Schroeder, C. V. Filip, Cs. Tóth, C. G. R. Geddes, G. Fubiani, R. Huber, R. A. Kaindl, E. Esarey, and W. P. Leemans. "Temporal Characterization of Femtosecond Laser-Plasma-Accelerated Electron Bunches Using Terahertz Radiation." *Phys. Rev. Lett.*, **96**:014801, Jan 2006.

[UKD96] D. Umstadter, J. K. Kim, and E. Dodd. "Laser Injection of Ultrashort Electron Pulses into Wakefield Plasma Waves." *Phys. Rev. Lett.*, **76**:2073–2076, Mar 1996.

[Vay07] J.-L. Vay. "Noninvariance of Space- and Time-Scale Ranges under a Lorentz Transformation and the Implications for the Study of Relativistic Interactions." *Phys. Rev. Lett.*, **98**:130405, Mar 2007.

[Vay08] J.-L. Vay. "Simulation of beams or plasmas crossing at relativistic velocitya)." *Physics of Plasmas*, **15**(5), 2008.

[WCB02] Shuoqin Wang, C. E. Clayton, B. E. Blue, E. S. Dodd, K. A. Marsh, W. B. Mori, C. Joshi, S. Lee, P. Muggli, T. Katsouleas, F. J. Decker, M. J. Hogan, R. H. Iverson, P. Raimondi, D. Walz, R. Siemann, and R. Assmann. "X-Ray Emission from Betatron Motion in a Plasma Wiggler." *Phys. Rev. Lett.*, **88**:135004, Mar 2002.

[WFG13] Ziran Wu, Alan S. Fisher, John Goodfellow, Matthias Fuchs, Dan Daranciang, Mark Hogan, Henrik Loos, and Aaron Lindenberg. "Intense terahertz pulses

from SLAC electron beams using coherent transition radiation." *Review of Scientific Instruments*, **84**(2), 2013.

[YI01] Gennady L. Yudin and Misha Yu. Ivanov. "Nonadiabatic tunnel ionization: Looking inside a laser cycle." *Phys. Rev. A*, **64**:013409, Jun 2001.

[YMG00] X. Yan, A. M. MacLeod, W. A. Gillespie, G. M. H. Knippels, D. Oepts, A. F. G. van der Meer, and W. Seidel. "Subpicosecond Electro-optic Measurement of Relativistic Electron Pulses." *Phys. Rev. Lett.*, **85**:3404–3407, Oct 2000.

[YMG01] X. Yan, A.M. MacLeod, W.A. Gillespie, G.M.H. Knippels, D. Oepts, and A.F.G. van der Meer. "Application of electro-optic sampling in {FEL} diagnostics." *Nuclear Instruments and Methods in Physics Research Section A: Accelerators, Spectrometers, Detectors and Associated Equipment*, **475**(1–3):504 – 508, 2001. FEL2000: Proc. 22nd Int. Free Electron Laser Conference and 7th F {EL} Users Workshop.